NANYANG
TECHNOLOGICAL
UNIVERSITY

INVESTIGATING THE OPEN-CIRCUIT VOLTAGE DEFICIT IN $Cu_2ZnSn(S,Se)_4$ SOLAR CELLS

TAI KONG FAI

SCHOOL OF PHYSICAL AND MATHEMATICAL SCIENCES

2015

INVESTIGATING THE OPEN-CIRCUIT VOLTAGE
DEFICIT IN $Cu_2ZnSn(S,Se)_4$ SOLAR CELLS

TAI KONG FAI

2015

INVESTIGATING THE OPEN-CIRCUIT VOLTAGE DEFICIT IN $Cu_2ZnSn(S,Se)_4$ SOLAR CELLS

TAI KONG FAI

School of Physical and Mathematical Sciences

A thesis submitted to the Nanyang Technological University

in fulfillment of the requirement for the degree of

Doctor of Philosophy

2015

Acknowledgements

I would first like to thank my supervisor, *Prof. Alfred Huan*, and my co-supervisor, *Prof. Subodh Gautam Mhaisalkar*. They have been very supportive throughout my PhD studies, and often encourage and advise me whenever I face difficulties in my research or my personal life. They have pointed out important directions during my PhD research and allow me to work closely with other talented researchers.

I would like to thank a few research staff members from IBM Thomas J. Watson Research Center in New York. *Dr. Oki Gunawan*, he is always very patient and effective in guiding me on electrical characterizations. He also taught me many important skill sets such as MATLAB programming, instrument control and automation, device simulation, data analysis and many others. I enjoyed building a measurement prototype with him out from scratch, and as well as the recreational time we spent together in USA. *Dr. Tayfun Gokmen*, who was my office-mate during my first internship, and guided me on programming microcontroller. He is very smart and a fast thinker. It would not be possible for me to code the microcontroller without any prior experience without him. *Dr. Talia Gershon*, who guide me on TRPL measurements and I appreciate the fruitful discussion on PL results, which helps me gain a better understanding on the fundamental properties of the chalcopyrite and kesterite thin films. I would also like to thank *Dr. David Mitzi*, *Dr. Wang Wei*, *Dr. Lee Yun Seog*, and other staff members in IBM who provide useful advice and helps during my internships.

I would like to thank my group members from *xc*-lab in Physics and Applied Physics, SPMS. Associate *Prof. Sum Tze Chien*, who has been encouraging and helpful in providing constructive advice during my PhD studies. *Dr. Xing Guichuan* and *Dr. Liu Xinfeng*, who are very experienced in optics and guided me on pump-probe spectroscopy and spatially resolved photoluminescence, and also provide valuable advice on analyzing the result. *Dr Chen Shi*, who help me on X-ray photoelectron spectroscopy and XPS depth profile.

My PhD research would not be possible without the high quality CZTSSe samples provided by *Dr. Masaru Kuwahara* from Tokyo Ohka Kogyo Co., Ltd., and *Dr. Fu Dongchuan* from Energy Research Institute in NTU (ERI@N). I am grateful that assistant *Prof. Lydia Helena Wong* and all other CIGS/CZTS group members from ERI@N have always being very supportive and willing to provide help. I would also like to acknowledge *Dr. Yu Zhigen* from Institute of High Performance Computing (IHPC) in A-star, for his step-by-step guidance on DFT calculation for materials simulation. I would like to acknowledge the 4 years Local Ph.D Scholarship sponsored by Clean Energy Programme Office (CEPO) and Energy Innovation Programme Office (EIPO) of National Research Foundation.

I would like to thank my wife, *Ms. Tan Jia Yi*, who always cheer me up and encourage me when I face hiccups, and always believe in me that I could do good research and finish my PhD gracefully. She takes very good care of me, which allows me to concentrate on my PhD studies. Lastly, I would like to thank my parents for providing useful advice when I face difficulties in life, and always being very caring and supportive for my decision.

Table of Contents

Table of Contents

Abstract

Thin film solar cells (TFSC) such as $Cu(In,Ga)Se_2$ (CIGS) and CdTe technology have been successfully commercialized with cost-per-watt on par with the conventional Si photovoltaics. Additional benefits of TFSC include shorter energy payback time, better light absorbance, and high flexibility (if deposited on flexible substrate) for a variety of applications. Among the industrialized TFSC, CIGS is less toxic and possesses the highest power conversion efficiency (PCE), but scarcity of indium and gallium could limit its growth potential. Therefore, research on earth-abundant and non-toxic $Cu_2ZnSn(S,Se)_4$ (CZTSSe) solar cell has generated tremendous interest in the photovoltaic community. However, large open-circuit voltage deficit ($V_{OC,def}$) in CZTSSe solar cell remains unresolved even after a decade of research and development. Although open-circuit voltage (V_{OC}) can be enhanced by increasing its bandgap (E_g) through the tuning of S/Se ratio, $V_{OC,def}$ ($E_g/q - V_{OC}$) generally becomes more severe accompanied by significant loss in short-circuit current density (J_{SC}) and fill factor (FF). These losses limit the power conversion efficiency (PCE) of CZTSSe solar cell. Therefore, in-depth investigations on the fundamental limitations are required to tackle the $V_{OC,def}$ issue. Other issues such as the J_{SC} and FF losses, specifically in the high bandgap CZTSSe solar cells, need to be investigated as well to further improve the device performance.

This thesis focuses on investigating the fundamental limitations of CZTSSe solar cells, in particular the large $V_{OC,def}$, by electrical, optical and physical characterizations. Full bandgap range CZTSSe solar cells from 1.0 to 1.5 eV were studied in this study to provide a comprehensive understanding on the limitations of the CZTSSe technologies. The loss factors were investigated from two perspectives: (i) the *intrinsic* electrical and defect properties of the CZTSSe absorber layer, and (ii) the *extrinsic* loss factors arising from the interfacial secondary phases and interfacial resistances such as high shunt conductance (which lowers V_{OC}) and high series resistance (which lowers J_{SC}).

The intrinsic limitations were investigated by self-developed electrical AC Hall measurement system and optical photoluminescence (PL) technique. From the AC Hall measurement, it was found that CZTSSe thin films (regardless of their bandgaps) typically have low carrier mobility of less than 1 $cm^2/V.s$. This pinpoints one major factor to account for the high V_{OC} deficit. In addition, PL studies indicate that CZTSSe material has a high defect density in the order of 10^{20} cm^{-3}, which results in a deep fluctuating potential (γ) at the conduction and valence band given its low dielectric constant. The upper bound of γ for CZTSSe ranges from 115 meV (Se-rich CZTSSe) to 144 meV (S-rich CZTSSe). The fluctuating conduction and valence band (2γ) of 230 meV and 288 meV partly accounts for the $V_{OC,def}$ of 588 meV and 933 meV in Se-rich and S-rich CZTSSe, respectively. Adding a general thermodynamic loss of ~350 meV to 2γ, the $V_{OC,def}$ in Se-rich CZTSSe can be easily explained, but the $V_{OC,def}$ in S-rich CZTSSe remains largely unaccountable. The deep fluctuating potential will essentially reduce the energy of the photo-generated carriers and results in much lower PL photon energy compared to its bandgap. This is consistent with the low carrier mobility which partly account for the large V_{OC} deficit.

Temperature-dependent PL further suggests that non-radiative recombination centers could be the dominant defects in CZTSSe absorbers, and the defect levels are much deeper compared with the benchmark CIGS absorber. From the Arrhenius relation, the activation energy (E_a) which includes the effect of defect energy level and non-radiative recombination rate can be extracted. The E_a for CIGSSe, Se-rich

CZTSSe and S-rich CZTSSe were found to be 20 meV, 48 meV and 67 meV, respectively. The particularly high E_a in S-rich CZTSSe serves as an additional factor to explain the largely unaccountable $V_{OC,def}$ (from the sum of thermodynamic loss and 2γ mentioned above). These undesired defect properties will exacerbate carrier recombination which already suffers from low carrier mobility. This will essentially lower the V_{OC} of the CZTSSe solar cells.

Extrinsic loss factors were investigated by electrical colour *I-V* (current-voltage sweep), Suns-V_{OC} and various physical characterizations including Glancing-Incidence X-Ray Diffraction (GIXRD), Field-Emission Scanning Electron Microscopy (FE-SEM), Raman mapping, X-ray Photoelectron Spectroscopy (XPS), and XPS depth profile. As shunt conductance was severe in high bandgap S-rich CZTSSe solar cell, it further lowers the V_{OC} by external device leakage path. Physical characterizations suggested the formation of shunting secondary phases at the CZTSSe/CdS interface which provides such leakage path. Besides the V_{OC} deficit issue, J_{SC} loss resulted from the high series resistance (R_S) was also observed in the high bandgap CZTSSe solar cell. Suns-Voc measurement indicates the formation of non-ohmic back contact, which could be due to Schottky contact formation arising from the low carrier density in high bandgap CZTSSe (as probed by AC Hall measurement), and hole blocking secondary phases forming at the CZTSSe/Mo interface which inhibits the carrier injection into Mo electrode. The latter factor was investigated extensively by various physical characterizations, and significant presence of high bandgap secondary phases was indeed found at the back contact interface. High bandgap CZTSSe, which are vulnerable to the formation of secondary phases, could suffer more in V_{OC} deficit, J_{SC} loss, and FF loss.

With better understanding on the intrinsic limiting factor of V_{OC} deficit, defect engineering was attempted in order to improve the crystal quality of CZTSSe. It was demonstrated that the defect properties could be improved, specifically by reducing and passivating the non-radiative defects through extrinsic Sb doping. With the reduction in total defect density by approximately half, the depth of the potential fluctuation was reduced from ~115 meV to ~86 meV. The reduction of γ corresponded well with the increase of V_{OC}. Other approaches such as partial or full elemental substitution could also be pursued to engineer the defect properties, as elaborated in Chapter 7. Specifically, the high concentration of the deep Cu_{Zn} antisite should be inhibited and shallower defects such as Cu-vacancy (V_{Cu}) should be promoted for improved device performance. Defect engineering should lift the kesterite solar cell research into a new phase which could potentially overcome the V_{OC} deficit bottleneck.

List of Figures

List of Tables

Publications List

1. Examination of electronic structure differences between CIGSSe and CZTSSe by photoluminescence study.
Kong Fai Tai, Talia Gershon, Oki Gunawan*, and Cheng Hon Alfred Huan.
Journal of Applied Physics, 117, 235701 (2015).
http://dx.doi.org/10.1063/1.4922493

2. A Parallel Dipole Line System.
Oki Gunawan*, Yudistira Virgus, and Kong Fai Tai.
Applied Physics Letter, 106, 062407 (2015).
http://dx.doi.org/10.1063/1.4907931

3. Antimony Doping in Solution-processed $Cu_2ZnSn(S,Se)_4$ Solar Cells.
Kong Fai Tai, Dongchuan Fu, Sing Yang Chiam, Cheng Hon Alfred Huan, Sudip Kumar Batabyal, Lydia Helena Wong*
(Equal contribution from Kong Fai Tai and Dongchuan Fu).
Chemistry and Sustainability, 8, 3504 (2015).
http://onlinelibrary.wiley.com/wol1/doi/10.1002/cssc.201500433/abstract

4. Fill factor losses in $Cu_2ZnSn(S_xSe_{1-x})_4$ solar cells: Insights from physical and electrical characterization of devices and exfoliated films
Kong Fai Tai, Oki Gunawan*, Masaru Kuwahara, Shi Chen, Subodh Gautam Mhaisalkar, Cheng Hon Alfred Huan, and David B. Mitzi.
Advanced Energy Materials (2015).
http://onlinelibrary.wiley.com/wol1/doi/10.1002/aenm.201501609/abstract

5. Effect of Zn(O,S) buffer layer thickness on charge carrier relaxation dynamics of $CuInSe_2$ solar cell
Juan Sun, Venkatram Nalla, Mai Nguyen, Yi Ren, Sing Yang Chiam, Yue Wang, Kong Fai Tai, Handong Sun, Nikolay Zheludev, Sudip K. Batabyal, Lydia H. Wong.
Solar Energy 115, 396-404 (2015).
http://doi:10.1016/j.solener.2015.03.008

6. ZnS buffer layer for $Cu_2ZnSn(S,Se)_4$ monograin layer solar cell.
Mai Nguyen, Kaia Ernits, Kong Fai Tai, Chin Fan Ng, Stevin Snellius Pramana, Wardhana A. Sasangka, Sudip K. Batabyal, Timo Holopainen, Dieter Meissner, Axel Neisser, Lydia H. Wong.
Solar Energy 111, 344-349 (2015).
http://doi:10.1016/j.solener.2014.11.006

7. $Cu_2ZnSn(S,Se)_4$ kesterite solar cell with 5.1% efficiency using spray pyrolysis of aqueous precursor solution followed by selenization.
Xin Zeng, Kong Fai Tai, Tianliang Zhang, Chun Wan John Ho, Xiaodong Chen, Alfred Huan, Tze Chien Sum, Lydia H. Wong.
Solar Energy Materials and Solar Cells, 124, 55-60 (2014).
http://doi:10.1016/j.solmat.2014.01.029

8. Uncovering loss mechanisms in silver nanoparticle-blended organic solar cells.
Bo Wu, Xianyang Wu, Cao Guan, Kong Fai Tai, Edwin Kok Lee Yeow, Hong Jin Fan, Nripan Mathews, Tze Chien Sum.
Nature Communications 4, 2004 (2013).
http://www.nature.com/ncomms/2013/130613/ncomms3004/full/ncomms3004.html

9. Carrier dynamics in polymer nanofiber:fullerene solar cells
Michael Kurniawan, Teddy Salim, Kong Fai Tai, Shuangyong Sun, Edbert Jarvis Sie, Xiangyang Wu, Edwin Kok Lee Yeow, Cheng Hon Alfred Huan, Yeng Ming Lam, Tze Chien Sum.
Journal of Physical Chemistry C, 116, 18015-18022 (2012).
http://pubs.acs.org/doi/abs/10.1021/jp302968e

Presentations

1. (Invited) Advanced characterization for world record kesterite solar cell and beyond: New tricks & inventions.

Kong Fai Tai, Oki Gunawan
2015 E-MRS Spring Meeting, Lille, France.
Symposium D, third session (11 May 2015, 2 pm): CZTS and its analogues.
http://www.emrs-strasbourg.com/index.php?option=com_abstract&task=view&id=294&year=2015&Itemid=&id_season=13

2. Parallel Dipole Line System: A Novel Magnetic Trap and High Sensitivity Hall system.

Oki Gunawan, Yudistira Virgus, Kong Fai Tai
2015 APS Meeting, San Antonio, USA.
Session B30: Focus session: Nanomagnetic Devices II (02 March 2015, 11:15 am).
http://meetings.aps.org/Meeting/MAR15/Session/B30.2

3. Variation of intrinsic defects on surface and bulk of Cu2ZnSn(S,Se)4 monograin for photovoltaic application.

Kong Fai Tai, Chin Fan Ng.
2013 IPS Meeting, Singapore.
T13 Organic and thin film photovoltaics (06 March 2013, 9.30 am).
http://www.ipsmeeting.org/

CHAPTER 1 Introduction

In 2014, the share of renewable energy has increased to 9.1% of global electricity generation. This would be equivalent to a saving of 1.3 gigatonnes of CO_2 emission. In particular, grid parity has been reached for photovoltaic in 30 countries and become the fastest growing renewable, with worldwide cumulative photovoltaic capacity reaching ~180 GW, sufficient to supply ~1% of global annual electricity consumption of 18.4 TWh currently.[1] Despite the positive changes, it would still require tremendous transformation in the energy system to keep the CO_2 content below 450 parts per million (ppm) in the atmosphere, in order to limit the global temperature rise within two degree Celsius.

1.1 Thin Film Photovoltaics

Mono- and poly-crystalline silicon remains the dominant technology (market share: 90.7%)[2] for photovoltaic. However, as the share of renewable energy in electricity generation increases, intermittency becomes an important issue for grid security. A cloud passing-by or temperature rise could severely affect the performance of Si photovoltaic, which will induce a sudden drop of power generation in the grid and may induce a power breakdown. On the other hand, thin film photovoltaic with a direct bandgap is less sensitive to light condition which is able to generate electricity even in dim or indoor light condition. As a result, they could generate more electric power in real working condition although the current efficiency of thin film photovoltaic (~14%) is lower than that of poly-Si photovoltaic (~17%).[3] Besides, due to its thin absorbing layer (1-5 µm), thin film photovoltaic could also be developed in flexible substrate for other applications such as automotive, surveillance plane, remote expedition, military, consumer electronics, Internet-of-Things (IoT) etc.

Commercialized thin film technology includes Cadmium-Telluride (CdTe), Copper indium gallium selenide (CIGS), and amorphous-Si (a-Si) technology. Due to the high production cost, low efficiency and stagnated improvement in a-Si, large scale production of a-Si has been discontinued. On the other hand, CdTe remains the cheapest solution for photovoltaic, with decent module efficiency of ~14%. However, toxic cadmium and rare tellurium could limit the growth of this technology, as seen in the decrease in production trend recently.[4] This left with the last solution- CIGS technology, which is the highest performing thin film photovoltaic with module efficiency close to 15%, and it is the only thin film technology going through production expansion (mainly in Japan by Solar Frontier). However, indium is expensive and a growing touch screen display industry will compete with indium feedstock.[5] This could potentially threaten CIGS technology in the future. Therefore, non-toxic, earth-abundant and stable (in ambient condition) alternative thin film solar cell is highly sought after, preferably produced with high-throughput and low-cost processing technique.

1.2 $Cu_2ZnSn(S,Se)_4$ Solar Cells and their Key Limitations

For Cu-chalcopyrite I-III-VI materials, aluminium (Al) was used to replace the rare indium and gallium to form Cu_2AlSe_2. However, this compound a has large bandgap of 2.7 eV and thus is unsuitable for solar cell application.[6, 7] Therefore, researchers began to look for elements from other group in the periodic table to replace Indium. One of the potential candidate is Cu_2ZnSnS_4 (CZTS), with the Group-III Indium or

Gallium replaced by the earth-abundant elements Zinc (Group-II) and Tin (Group-IV) to satisfy Octet Rule for crystal formation, as shown in **Figure 1-1**.

CZTS has a kesterite crystal structure, similar to the tetragonal chalcopyrite-CIGS [**Figure 1-3 (a)**]. CZTS has many desired properties for high photovoltaic performance, such as direct bandgap, high absorption coefficient (~10^5 cm^{-1}) and the ability to be synthesized by a variety of scalable processes. By intermixing S and Se in $Cu_2ZnSn(S_xSe_{1-x})_4$ (CZTSSe), the bandgap (E_g) can be tuned from ~1.0 eV for the pure selenide (x = 0) $Cu_2ZnSnSe_4$ (CZTSe) to ~1.5 eV for the pure sulfide (x = 1) CZTS, covering the optimum bandgap range for single junction solar cell according to Shockley-Queisser limit.[8, 9]

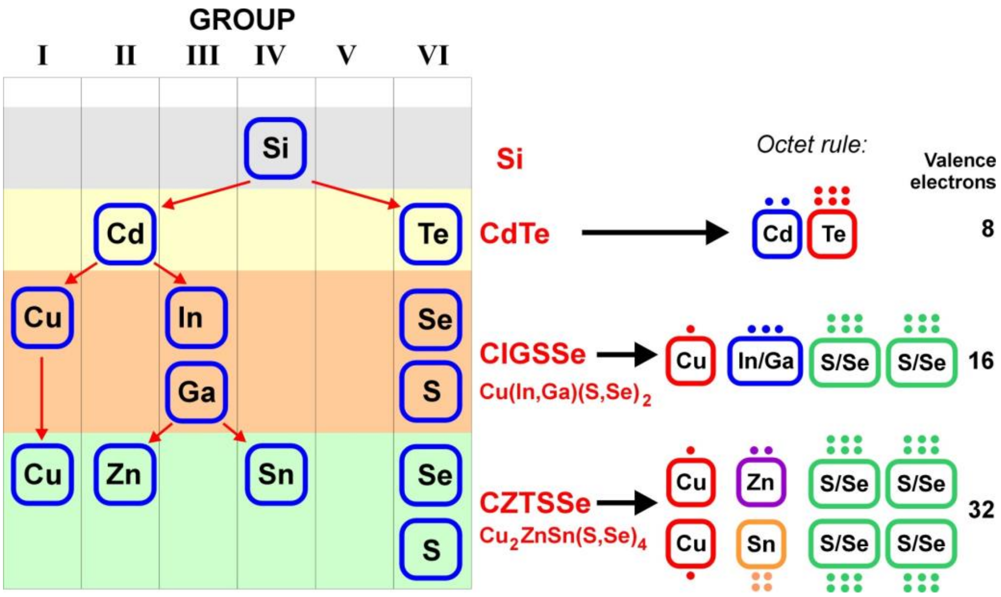

Figure 1-1. Breeding process of photovoltaic technology.

1.2.1 Operating Principles

Due to the similar crystal structure and optoelectronic properties between CIGS and CZTSSe, the same device architecture and processing techniques can be inherited from CIGSSe research on the current generation CZTSSe solar cells. Device were fabricated on a substrate configuration [**Figure 1-2 (a)**], where light transmitted through the top stack transparent conducting oxide (TCO) and buffer layers before reaching the absorber layer (CZTSSe or CIGS). Light was absorbed by the CZTSSe or CIGS layer, and photogenerated electrons will flow towards the n-junction (CdS/ZnO) while holes flow towards the molybdenum (Mo) back contact under favourable band alignment [**Figure 1-2 (b)**] condition. While electron-hole pair is efficiently swept across by the electric field in the depletion region (which extends 0.2 - 0.6 μm into the absorber layer),[10, 11] a long carrier diffusion length ($L_d = \sqrt{D_n \tau}$, where D_n is the minority carrier diffusion coefficient and τ is the minority carrier lifetime) will enable photogenerated carriers in the neutral bulk region of the absorber to traverse across the layer and thus improve charge collection. On the p-n interface, a thin layer of CdS (< 50 nm) between the absorber and n^+-*type* ZnO layer was deposited to provide a "spike" like positive conduction band offset (CBO) such that interfacial recombination is reduced.[12, 13]

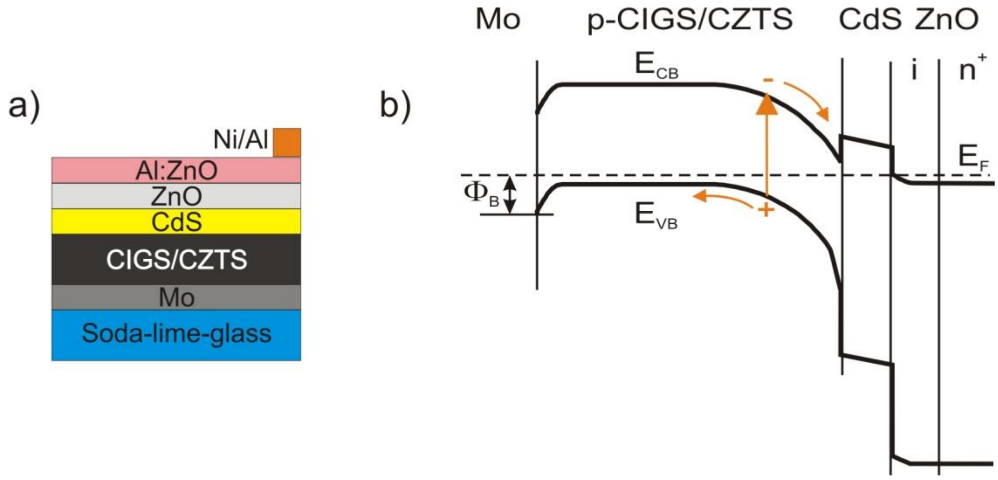

Figure 1-2. (a) Schematics of device structure and **(b)** band alignment for CIGS/CZTS solar cells.

1.2.2 Progress in $Cu_2ZnSn(S,Se)_4$ Solar Cells

The first CZTS solar cell was reported by Katagiri et. al. in 1996 with a power conversion efficiency (PCE) of 0.66% and open-circuit voltage (V_{OC}) of 0.4 V using sequential evaporation for the CZTS film.[14] After a decade, Katagiri et. al. reported a major leap in CZTS solar cell with PCE of 5.7% followed by 6.8%.[15, 16] The latest PCE for pure sulphide CZTS/CdS solar cell is 8.4% with CZTS film deposited by co-evaporation technique.[17] Development of large-area (5×5 cm^2) CZTS sub-module by Solar Frontier has also shown promising progress with efficiency of 9.2% by using a hybrid buffer layer with a combination of CdS and In_2S_3.[18] On the other hand, the analogous pure selenide CZTSe/CdS solar cell fabricated by co-evaporation technique has the latest PCE of 11.6%,[19] while the intermixed sulfoselenide CZTSSe/CdS solar cell fabricated by hydrazine solution-processing holds the record-efficiency of 12.6% for CZTSSe solar cell technology.[20] The progress of CZTSSe solar cells is summarized in **Figure 1-3 (c)**.

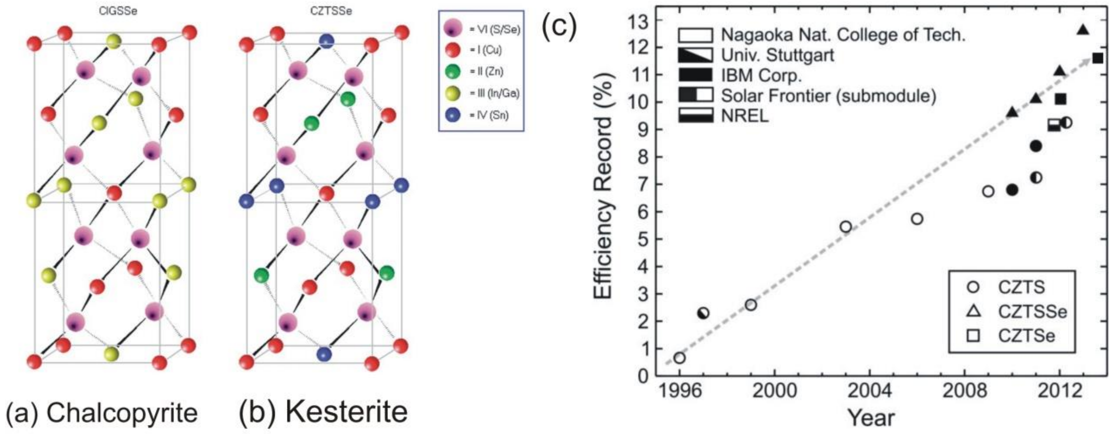

(a) Chalcopyrite (b) Kesterite

Figure 1-3. Crystal structure of **(a)** CIGSSe (chalcopyrite) and **(b)** CZTSSe (kesterite). **(c)** Performance of CZTSSe thin film solar cells showing consistent progress towards higher efficiency. The figures are extracted from Ref. [21, 22]

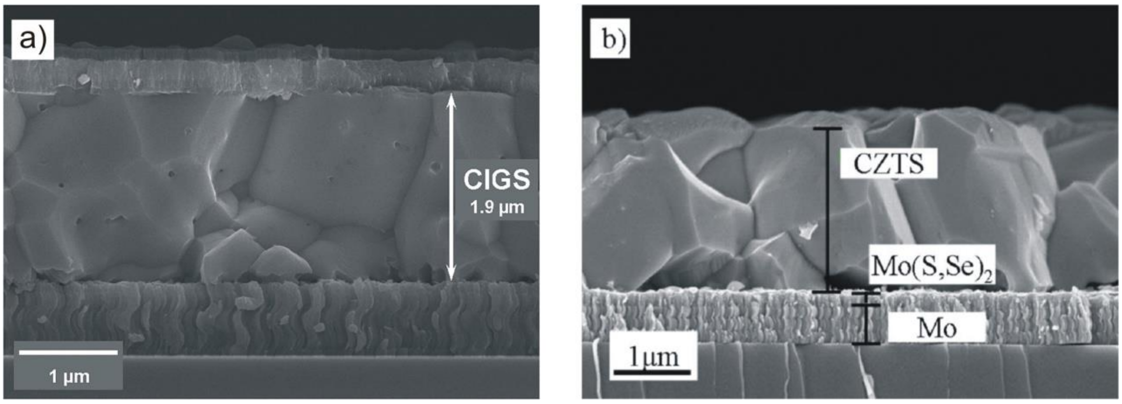

Figure 1-4. Cross section of the **(a)** 15.2% CIGSSe and **(b)** 12.6% CZTSSe solar cells processed by hydrazine solution-processing technique. The figures are extracted from Ref.[20, 23]

Solution processing technique offers ample opportunity for high-throughput large-scale production in thin film photovoltaic. CIGSSe and CZTSSe solar cells fabricated by hydrazine-solution processing gives the best performance among solution-processed devices.[11, 22] **Figure 1-4** shows the cross-section scanning electron microscope (SEM) images of CIGSSe (E_g = 1.16 eV, PCE: 15.2%)[22] and CZTSSe (E_g = 1.13 eV, PCE: 12.6%)[11] solar cells fabricated by hydrazine-solution method. The grain sizes of both CZTSSe and CIGSSe absorber layers span across the thicknesses of ~2 µm. In addition, X-ray diffraction (XRD) for both films shows sharp diffraction peaks for the absorbers,[24] indicating that the CIGSSe and CZTSSe crystals grown by solution-processing method are highly crystallized. Furthermore, transmission energy-dispersive X-ray spectroscopy (EDX) indicates a uniform elemental composition across the film's thickness.[11]

1.2.3 Calculated Phase Stability of $Cu_2ZnSnS(Se)_4$

The stoichiometric ratio of Cu, Zn, Sn, S (or Se) elements in CZTS(Se) crystal is 2:1:1:4. As a result from the increased number of component elements in CZTSSe, competing secondary compounds could form and co-exist with the kesterite CZTSSe phase. The formation of secondary phases could be induced by non-stoichiometric elemental composition or growth conditions (e.g. elemental vapor pressure). Phase stability of CZTS(Se) was shown in a calculated phase diagram by the area of stable region included within specific chemical potential (μ_x) range of the component element (x). Theoretically, secondary phases would not be formed if μ_x for all component elements lie within this stable phase region.

The stable region in chemical potential space can be calculated under several constraints. First, μ_x should be negative ($\mu_x < 0$) to avoid the formation of pure component element. Second, to maintain a stable CZTS(Se) crystal, μ_x must satisfies the following relation:[25, 26]

$$2\mu_{Cu} + \mu_{Zn} + \mu_{Sn} + 4\mu_{S(Se)} = \Delta H_f(\mathrm{Cu_2ZnSnS(Se)_4}) = -4.21\ (-3.21)\ \mathrm{eV}, \quad (1.1)$$

Third, to avoid the formation of secondary phases such as CuS(Se), $Cu_2S(Se)$, ZnS(Se), SnS(Se), $SnS(Se)_2$, and $Cu_2SnS(Se)_3$, the following relations must also be satisfied:[25, 26]

$$\begin{aligned}
\mu_{Cu} + \mu_{S(Se)} &< \Delta H_f(\mathrm{CuS(Se)}) = -0.49\ (-0.30)\ \mathrm{eV},\\
2\mu_{Cu} + \mu_{S(Se)} &< \Delta H_f(\mathrm{Cu_2S(Se)}) = -0.52\ (-0.24)\ \mathrm{eV},\\
\mu_{Zn} + \mu_{S(Se)} &< \Delta H_f(\mathrm{ZnS(Se)}) = -1.75\ (-1.45)\ \mathrm{eV},\\
\mu_{Sn} + \mu_{S(Se)} &< \Delta H_f(\mathrm{SnS(Se)}) = -1.01\ (-0.90)\ \mathrm{eV},\\
\mu_{Sn} + 2\mu_{S(Se)} &< \Delta H_f(\mathrm{SnS(Se)_2}) = -1.33\ (-1.04)\ \mathrm{eV},\\
2\mu_{Cu} + \mu_{Sn} + 3\mu_{S(Se)} &< \Delta H_f(\mathrm{Cu_2SnS(Se)_3}) = -2.36\ (-1.80)\mathrm{eV}, \quad (1.2)
\end{aligned}$$

where $\Delta H_f(Y)$ are the calculated formation enthalpies of the compound Y from density-functional theory (DFT).

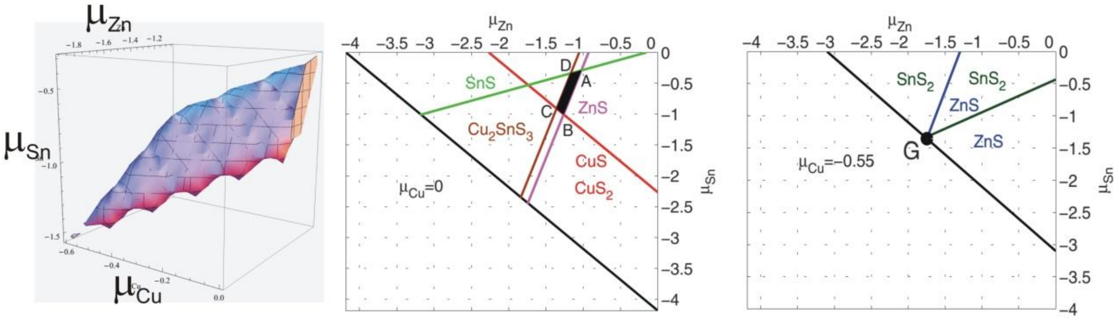

(a) 3D phase diagram (b) μ_{Cu} = 0 (c) μ_{Cu} = -0.55

Figure 1-5. (a) Calculated 3D phase diagram for Cu_2ZnSnS_4, **(b)** 2D projection at μ_{Cu} = 0 (Cu-rich), **(c)** μ_{Cu} = -0.55 (Cu-poor). **(b)** and **(c)** are extracted from Ref.[26]

Under the above constraints, the chemical-potential range of Cu, Zn, and Sn that stabilizes $Cu_2ZnSnS(Se)_4$ is bound by a polyhedron in a three-dimensional (μ_{Cu}, μ_{Zn}, μ_{Sn}) space, with μ_{Se} being the dependent variable. **Figure 1-5 (a)** shows such stable region for CZTS crystal bound by a polyhedron. To express the region more clearly, two planes with μ_{Cu} = 0 and μ_{Cu} = -0.55 eV are plotted in **Figure 1-5 (b)** and **(c)** respectively, in which the stable region shrinks when Cu becomes poorer (more negative μ_{Cu}). Compared to the stable region of $CuInSe_2$, the range of μ_{Zn} and μ_{Sn} in CZTS(Se) are much narrower than that of μ_{In} in $CuInSe_2$,[25, 26] indicating that the synthesis of pure-phase CZTS(Se) crystal needs crucial control on the elemental composition.

1.2.4 Formation of Isolated Defects and Defect Clusters

Intuitively, pure-phase CZTSSe should be formed under stoichiometric chemical composition. However, the best performing CZTS(Se) devices do not have elemental composition near stoichiometric ratio. The chemical composition of the precursor metals is often deliberately altered from the stoichiometric ratio. **Figure 1-6 (a)** illustrates the efficiency distribution with different elemental ratio fabricated by different research groups. It can be seen that the high-performance CZTSSe solar cells were generally achieved under Cu-poor and Zn-rich condition, with Cu/(Zn+Sn) ratio ranging from 0.74 to 0.92, and Zn/Sn ratio ranging from 1.00 to 1.25.[25] This was further verified from the devices fabricated by the same group using DC magnetron sputtering, which gives the highest device efficiency with Cu/(Zn+Sn) ≈ 0.74 and Zn/Sn ≈ 1.23, as shown in **Figure 1-6 (b)**.[27]

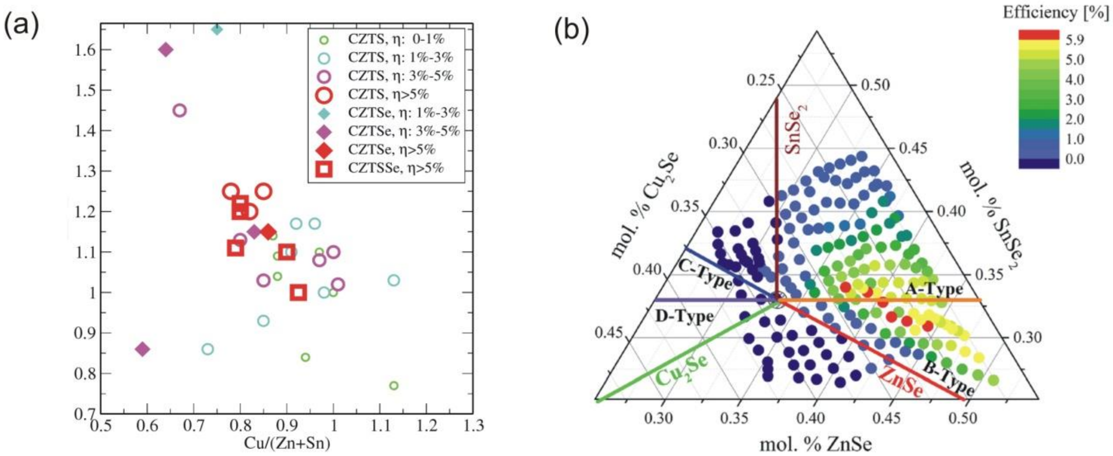

Figure 1-6. (a) Distribution of efficiency for Cu_2ZnSnS_4, $Cu_2ZnSnSe_4$, $Cu_2ZnSn(S,Se)_4$ solar cells with different elemental ratio [Cu/(Zn+Sn) and Zn/Sn]. **(b)** Similar efficiency distribution with elemental ratio fabricated by a single group with DC magnetron sputtering. The figures are extracted from Ref. [25, 27]

Besides formation of secondary phases, the variation from non-stoichiometric ratio highlights the importance of intrinsic defects formation. Due to the low formation energy of acceptor-like intrinsic defects, *i.e.* Cu_{Zn} antisite (Cu replacing Zn) and V_{Cu} (Cu-vacancy), CZTS(Se) has intrinsic p-type conductivity.[25, 26] Apart from these two defects, there are also many other possible lattice defects due to its multinary component elements, including vacancies (V_{Zn}, V_{Sn}, $V_{S(Se)}$), antisites (Cu_{Sn}, Zn_{Sn}, Zn_{Cu}, Sn_{Cu}, Sn_{Zn}) and interstitials (Cu_i, Zn_i). The formation energies of all these defects were calculated, with *Cu_{Zn} forms most easily* (lowest formation energy), followed by V_{Cu}. Other acceptor defects have much higher formation energy and thus their contribution to the p-type conductivity may be negligible, even though they can still act as recombination centers.[25, 26] In addition, the defect energy levels with respect to the band edge were also calculated. **Figure 1-7 (a)** shows the isolated defect energy levels for the pure sulfide CZTS. Similar calculation on pure selenide CZTSe can be found in Ref.[25]

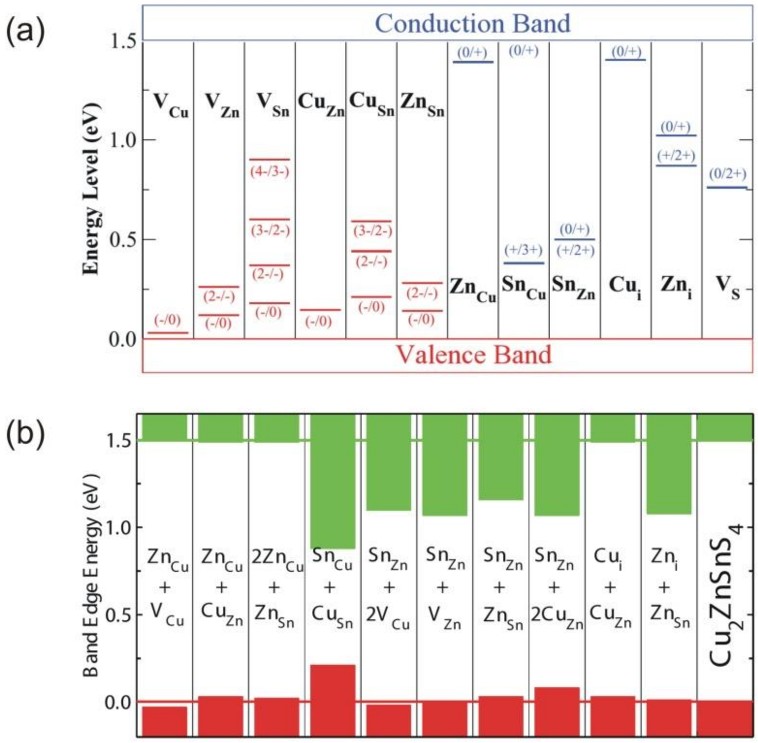

Figure 1-7. (a) Calculated point defect levels and **(b)** defect cluster levels of CZTS with respect to the band edge by DFT simulation. The figures are extracted from Ref.[25]

Similar to $CuInSe_2$, V_{Cu} has the shallowest defect energy of 0.02 - 0.03 eV above the valence band maximum (VBM) for CZTS(Se). However, the *dominant* Cu_{Zn} acceptor-like defect is relatively deeper with 0.15 eV above VBM for CZTS and 0.11 eV above VBM for CZTSe. Noted that the dominant defect is also the shallowest defect (V_{Cu}) in $CuInSe_2$, but this is not the case in CZTS(Se) apparently, where the dominant defect is Cu_{Zn} but the shallowest defect is V_{Cu}.[25, 26] The relatively deeper dominant defects (Cu_{Zn}) in CZTSSe may lead to low conductivity as hole carriers are not easily ionized to the valence band.[11] The difference in defect physics compared to $CuInSe_2$ will adversely impact the optoelectronic properties of CZTSSe solar cell.

Donor-like defects could also be formed in CZTS(Se). Although their formation energies are much higher, they can form donor-acceptor neutral *defect cluster* to reduce the overall formation energies relative to the sum of the isolated ones. However, these defect clusters are self-compensated and do not contribute to the carrier concentration. The reduction of overall formation energies is due to the strong Coulombic attraction between the charged defects. As a result, the energy levels with respect to the band edge of the neutral defect cluster will be reduced too. For example, the energy level with respect to the band edge for $[\mathrm{Zn}_{\mathrm{Cu}}^{+} + \mathrm{V}_{\mathrm{Cu}}^{-}]$ defect cluster reduces [**Figure 1-7 (b)**] compared to the isolated $\mathrm{Zn}_{\mathrm{Cu}}$ and V_{Cu} defects. As the band edge is only shifted slightly with $[\mathrm{Zn}_{\mathrm{Cu}}^{+} + \mathrm{V}_{\mathrm{Cu}}^{-}]$ defect cluster, its impact on the electronic structure and optical properties is weak and thus they can be regarded as benign defects.[25, 26] Similarly, other defect clusters which involves *Zn replacing Cu or Sn, i.e.* $[\mathrm{Zn}_{\mathrm{Cu}}^{+} + \mathrm{Cu}_{\mathrm{Zn}}^{-}]$, $[2\mathrm{Zn}_{\mathrm{Cu}}^{+} + \mathrm{Zn}_{\mathrm{Sn}}^{2-}]$, and $[\mathrm{Cu}_{\mathrm{i}}^{+} + \mathrm{Cu}_{\mathrm{Zn}}^{-}]$ are also found to be *electrically benign*. On the other hand, defect clusters that involve *Sn replacing Cu or Zn* (Sn_{Cu} *or* Sn_{Zn}) *are detrimental* as they shift the band edge of CZTS significantly. Noted that the isolated donor point defects which involves Sn replacing Cu or Zn ($\mathrm{Sn}_{\mathrm{Cu}}$ or $\mathrm{Sn}_{\mathrm{Zn}}$) also possess deep energy levels.[25, 26] *Therefore, this helps to explain the fact that the high performing CZTSSe solar cells are always Zn-rich and Sn-poor.*

1.2.5 Findings from DFT Simulation

From the First-principle calculations based on density functional theory (DFT), several factors could be found to explain why the high-efficiency CZTS(Se) solar cells were achieved under Cu-poor, Zn-rich and Sn-poor condition:

(1) Formation of Cu- & Sn-related detrimental secondary phases [CuS(Se), $\mathrm{Cu_2S(Se)}$, SnS(Se), $\mathrm{Cu_2SnS(Se)_3}$] with bandgap lower than CZTS(Se) could be diminished or

avoided. These secondary phases which are very conductive could provide shunting paths and lower the V_{OC}. Although high bandgap secondary phases such as ZnS could form under Zn-rich condition, ZnS does not absorb much of the solar spectrum and it is very resistive which simply act as dead region in the solar cell. This will not be detrimental (if the presence is minor) in comparison with the shunting effect provided by other secondary phases. However, if ZnS has significant presence in the CZTSSe host, the series resistance (R_S) of the solar cell will be increased.

(2) The formation of shallow acceptor-like defects, *i.e.* V_{Cu}, was promoted instead of the relatively deeper Cu_{Zn} antisite. The formation energy of Cu_{Zn} was calculated to be the lowest and thus it should be the dominant defects. However, these calculations were done based on the narrow ranges of elemental chemical potentials (μ_x) inside the stable CZTS(Se) phase region. In real working devices with elemental composition deviated so much from the stoichiometric ratio, the formation energy of respective defects could be different. Therefore, a Cu-poor and Zn-rich condition will essentially lower the formation energy of V_{Cu} and raises the formation energy of Cu_{Zn}.

(3) Formation of isolated deep donor defects such as $\mathrm{Sn}_{\mathrm{Zn}}^{2+}$, which has a formation energy lower than 1.0 eV in CZTS could be diminished or avoided.[25]

(4) Formation of detrimental defect clusters such as $[\mathrm{Sn}_{\mathrm{Cu}}^{+} + \mathrm{Cu}_{\mathrm{Sn}}^{-}]$, $[\mathrm{Sn}_{\mathrm{Zn}}^{2+} + 2\mathrm{V}_{\mathrm{Cu}}^{-}]$, $[\mathrm{Sn}_{\mathrm{Zn}}^{2+} + \mathrm{V}_{\mathrm{Zn}}^{2-}]$, $[\mathrm{Sn}_{\mathrm{Zn}}^{2+} + \mathrm{Zn}_{\mathrm{Sn}}^{2-}]$, $[\mathrm{Sn}_{\mathrm{Zn}}^{2+} + 2\mathrm{Cu}_{\mathrm{Zn}}^{-}]$, as shown in **Figure 1-7** (b), could be diminished or avoided.

(5) Formation of beneficial $[\mathrm{Zn}_{\mathrm{Cu}}^{+} + \mathrm{V}_{\mathrm{Cu}}^{-}]$ defect cluster, possibly at some domains like grain boundaries and/or *p-n* interface will be promoted. $[\mathrm{Zn}_{\mathrm{Cu}}^{+} + \mathrm{V}_{\mathrm{Cu}}^{-}]$ is beneficial because it shifts the VBM downward without shifting the CBM significantly. This results in a valence band bending that facilitates the separation of photo-generated

electron-hole pairs, and thus reducing electron-hole recombination as found in the chalcopyrite $CuInSe_2$.[28-30]

1.2.6 Key Limitations of CZTSSe Solar Cells

Although the physical grain size and crystal quality of CZTSSe looks similar to that of CIGSSe (**Figure 1-4**), the device performance is comparably poorer than CIGSSe solar cell.[22] Despite both the CIGSSe and record-CZTSSe (PCE: 12.6%) shown in **Figure 1-8** have similar bandgaps of 1.16 eV and 1.13 eV respectively, the open-circuit voltage (V_{OC}) of the record-CZTSSe solar cell (513 mV) was significantly lower than the CIGSSe solar cell (623 mV) fabricated using the same process.[11, 22] To quantify the loss in V_{OC} in consideration of their respective bandgaps, a parameter called *open-circuit voltage deficit* ($V_{OC,def}$) was defined as the bandgap (E_g) divided by electron charge and subtracted by the V_{OC} ($V_{OC,def} = E_g/q - V_{OC}$). The $V_{OC,def}$ in the 15.2% CIGSSe solar cell was 537 mV while the $V_{OC,def}$ in the record 12.6% CZTSSe solar cell was 617 mV, which means a total of 80 mV higher than the former.[11, 22] Following the $V_{OC,def}$ issue, fill factor (FF) poses the second major issue in CZTSSe, with FF of 69.8% compared to FF of 75% in CIGSSe.

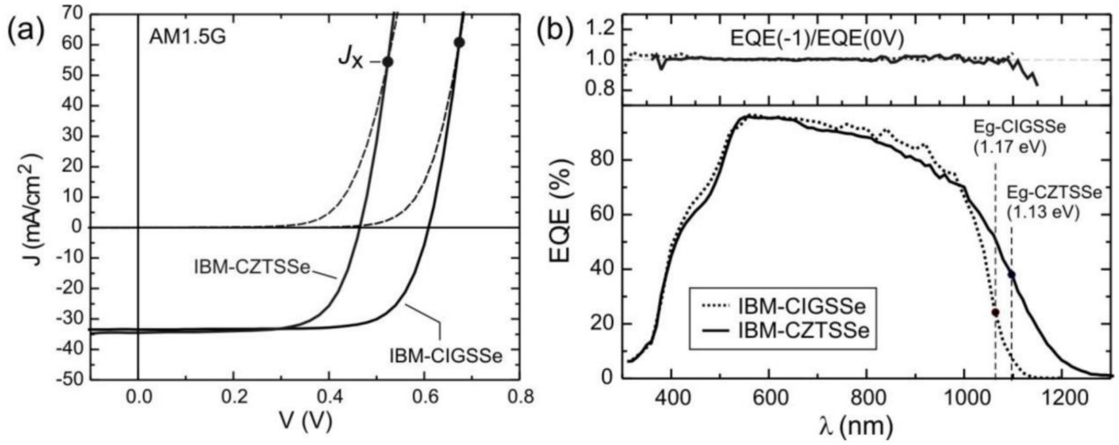

Figure 1-8. (a) J-V device characteristics and **(b)** external quantum efficiency (EQE) of the hydrazine solution-processed CIGSSe (Eff: 15.2%) and CZTSSe (Eff: 12.6%). J_x indicates the cross-over point between the dark J-V and light J-V curves. The upper

panel of (b) shows the ratio of the EQE at voltage bias -1.0 and 0.0 V. The figures are extracted from Ref.[22]

One reason for the high $V_{OC,def}$ in CZTSSe solar cell is reflected in the spectral response external quantum efficiency (EQE). As shown in **Figure 1-8 (b)**, the EQE of the CZTSSe solar cell has a slow decay for photon energy smaller than its E_g (λ > 1100 nm), while the CIGSSe solar cell has a sharper decay for photon energy smaller than E_g. This implies that there is more sub-bandgap absorption in CZTSSe, and indicates the significant role of sub-bandgap defect states or band-tails in the optoelectronic properties.[31] The sub-bandgap absorption will increase the short-circuit current density (J_{SC}), as indicated by: (a) the larger integrated area of EQE below the bandgaps, and (b) the higher J_{SC} in CZTSSe vs. CIGSSe (35.2 vs. 32.6 mA/cm^2). However, the sub-bandgap defects and/or band-tails could have a more severe impact which overwhelms the increment of J_{SC}, *i.e.* reducing the quasi Fermi level splitting (QFLS) given by QFLS = E_{Fn} - E_{Fp}, where E_{Fn} is the electron's quasi Fermi level and E_{Fp} is the hole's quasi Fermi level. A low QFSL will essentially lower the V_{OC}.[32]

Currently, *V_{OC} deficit problem poses the biggest hurdle for CZTSSe solar cell*. To further exacerbate the situation, an increasing $V_{OC,def}$ was generally observed as the bandgap of $Cu_2ZnSn(S_xSe_{1-x})_4$ increases (with higher value of x). For instance, the $V_{OC,def}$ in the record-CZTSe (E_g = 1.00 eV, PCE= 11.6%), record-CZTSSe (E_g = 1.13 eV, PCE= 12.6%) and record-CZTS (E_g = 1.45 eV, PCE= 8.4%) solar cells are 577, 617, and 789 mV respectively.[17, 19, 20] Therefore, an in-depth investigation on the origins of sub-bandgap defect states and band-tails will be important to overcome the V_{OC} deficit issue. In addition, the defect physics could vary with different S/(S+Se) ratio, which require further examinations.

In another aspect of solar cell operation, the collection length (L_c) for photogenerated carriers in n^+-p junction of *thin film* solar cells is approximately the sum of the depletion width (x_d) and the minority carrier diffusion length (L_d) in the absorber layer ($L_c \approx x_d + L_d$).[19, 33] Low performing CZTSSe solar cells generally have a short L_d. This was reflected in the ratio of the reverse-bias-EQE to zero-bias-EQE measurement larger than the unity [EQE(-1V)/EQE(0V) > 1],[34] because reverse bias will lengthen the depletion width and helps to sweep the photogenerated carriers with low diffusion length. This problem is generally termed as *voltage-dependent collection efficiency* (VDCE) issue for thin film solar cells. VDCE issue was also reflected in the low cross-over point (J_x) between the light (LJV) and dark J-V (DJV) curves.[34] However, the current high performance CZTSSe solar cells (with $E_g < 1.20$ eV) have shown significant improvement on this aspect, with high cross-over point (J_x) observed in **Figure 1-8 (a)**, and EQE(-1V)/EQE(0V) close to unity as shown in the upper panel of **Figure 1-8 (b)**.[19, 20]

Therefore, with better charge collection in high-performing CZTSSe solar cells (typically with $E_g < 1.20$ eV), the J_{SC} are high and comparable to CIGSSe, achieving more than 80% of Shockley-Quiesser limit on the J_{SC} (SQ-J_{SC}).[8, 9, 19, 20] However, J_{SC} in high E_g CZTSSe solar cells were generally low, achieving just ~65% of SQ-J_{SC}.[17] The low J_{SC} arise from the high series resistance (R_S) which are generally observed in large E_g CZTSSe solar cells.[17, 35-37] The high R_S in large E_g CZTSSe solar cells will also lower the fill factor (FF) by the empirical relations.[38] As a result, the combination of *J_{SC} and FF losses pose the second key limitation for CZTSSe solar cell, particularly for the large E_g absorber with high S/(S+Se) ratio*.

1.3 Objectives and Scopes

The advantages of $Cu_2ZnSn(S_xSe_{1-x})_4$ as solar cell absorber material includes its non-toxic nature, abundance of component elements, high absorption coefficient (~10^5 cm^{-1}), viable and inexpensive solution processability, and high stability without any encapsulation.[39] These advantages have positioned $Cu_2ZnSn(S_xSe_{1-x})_4$ as a strong candidate for thin film solar cells, especially with the latest reported power conversion efficiency that exceeds 12%.[20] Albeit significant progress has been achieved in CZTSSe solar cell, the record PCE has stagnated at 12.6% for more than a year,[20] indicating that in-depth scientific understanding on the key limitations is critical to overcome the $V_{OC,def}$ problem.

The aim of this thesis is to examine both the *intrinsic* (related to the electrical and defect properties of the CZTSSe layer) and *extrinsic* (related to the device level such as interfaces) loss mechanisms leading to the key limitations as described in **Section 1.2.6** ($V_{OC,def}$ in all CZTSSe and J_{SC} and FF losses in high bandgap CZTSSe). The details of the objectives are outlined as below, and the investigations were benchmarked with the well established CIGSSe cells.

1.3.1 Investigate the $V_{OC,def}$ in CZTSSe Solar Cells

Large $V_{OC,def}$ is the number one problem in CZTSSe technology. Furthermore, $V_{OC,def}$ increases with higher S/(S+Se) ratio or bandgap. *Note: increasing S/(S+Se) ratio and increasing bandgap are equivalent and will be used intermixable from here onwards.* Accompanied by the reduced light absorption as bandgap increases, the increasing $V_{OC,def}$ limits the best efficiency cells to have a bandgap below 1.20 eV.[20, 40-42] Therefore, the behaviour of increasing $V_{OC,def}$ with bandgap in CZTSSe induces a further probe on the loss mechanisms.

Hence, the first objective is to study the loss mechanisms of the generally high $V_{OC,def}$ in CZTSSe solar cells and to investigate the increasing $V_{OC,def}$ behaviour with bandgap by utilizing a series of full bandgap (E_g) range of the high performing $Cu_2ZnSn(S_xSe_{1-x})_4$ solar cells ranging from 1.0 to 1.5 eV. For a comprehensive understanding, the loss factors will be examined from two perspectives:

(A) *Intrinsic loss factors* which arise from CZTSSe bulk absorber layers will be studied by self-developed electrical AC Hall effect measurement and optical photoluminescence (PL) studies. The electrical properties such as the free carrier density and majority carrier mobility will be correlated to the defect properties probed by power- and temperature-dependent PL studies.

(B) *Extrinsic loss factors* which could arise from interfacial losses on the device level such as possible leakage path in the interfaces. This will be investigated mainly by extracting the device parameters from current-voltage (*I-V*) sweep, and physical characterizations will be deployed to inspect the existence of shunting secondary phases.

1.3.2 Investigate the J_{SC} and FF Losses in High Bandgap CZTSSe Solar Cells

As highlighted in **Section 1.2.6**, an increasing J_{SC} loss (compared to the SQ-J_{SC} limit) and FF loss arise from higher series resistance (R_S) were observed as the S/(S+Se) ratio increases. These losses exacerbate the performance and the concerted effects together with the increasing $V_{OC,def}$ result in a low PCE for high bandgap CZTSSe solar cells. Therefore, it is important to investigate the causes of the increasing R_S with S/(S+Se) ratio as this poses an additional efficiency pinning factor (besides the increasing $V_{OC,def}$) when the bandgap of CZTSSe increases.

Hence, the second objective is to investigate the contributing factors to the increasing R_S of the solar cells as the bandgap of CZTSSe increases. In general, there are two components that contribute to the R_S of a solar cell:

(A) The bulk resistance of the CZTSSe layer, where thicker absorber layer give rise to a higher bulk R_S. Resistivity measurement will be done such that the bulk resistance of the CZTSSe layer can be calculated simply from the product of resistivity and the film thickness (ρ.t).

(B) Interfacial resistance developed in the *p-n* junction or back contact. Interfacial resistance will be examined by colour *I-V* sweep (to assess the *p-n* junction resistance) and Suns-V_{OC} measurement (to assess the back contact resistance). To further explore the sources of interfacial resistance, self-developed exfoliation technique and various physical characterizations will be employed to inspect the possible formation of large bandgap secondary phases at the interfaces.

1.3.3 Investigation of Defect Properties and Their Correlation with Enhanced Device Performance

The tail states depicted in the EQE measurement, as shown in **Figure 1-8 (b)**, implies a significant contribution of sub-bandgap defect states to the $V_{OC,def}$ generally observed in CZTSSe solar cells. In addition, previous DFT calculations (**Section 1.2.4**) have shown that Cu_{Zn} lattice defect has the lowest formation energy. Thus, Cu_{Zn} antisite could be the dominant acceptors responsible for the intrinsic *p*-type behaviour of CZTSSe. However, Cu_{Zn} defects have a much deeper energy level above the valence band maximum (VBM) "(relative to, for example, V_{Cu} of just 20 meV above the valence band maximum), which could lower the *p*-type conductivity in CZTSSe. Furthermore, other isolated deep defects may present in CZTSSe which will quench the photogenerated carriers, likely through non-radiative recombination. Based on the investigations of the $V_{OC,def}$ loss mechanisms highlighted in the first objective, an in-depth understanding on the defect properties could be achieved such that defect engineering could potentially be designed to resolve the $V_{OC,def}$ bottleneck.

Hence, the third objective is to engineer the defect properties for enhanced device performance. *Extrinsic doping* will first be attempted in hope to improve the *intrinsic* crystal quality of CZTSSe by reducing or passivating the detrimental sub-bandgap defect states. Similar PL studies, in particular power- and temperature-dependent PL experiments will be done to examine the defect properties of doped CZTSSe to investigate if the doping attempts were efficient. A second approach for defect engineering is to avoid the Cu_{Zn} antisite defects. Acceptor defects like Cu_{Zn} is not ideal for solar cell due to its relatively deep energy level compared to the dominant V_{Cu} in CIGS. In addition, the extremely low formation energy of Cu_{Zn} antisite suggests that a high defect concentration may occur in CZTSSe, generating side-effects like severe potential fluctuation. The second approach can be attempted by partial of full replacement of Zn by other group II elements. This could improve the defect properties without changing the bandgap too much as Zn orbitals do not contribute significantly in the electronic structure of the band edges.[43] Defect engineering could be the possible pathway to resolve the $V_{OC,def}$ bottleneck and this objective serve as an starting point for the next-phase kesterite research.

1.4 Thesis Outline

The thesis consists of seven chapters; a brief introduction to each chapter is as follow:

CHAPTER 1 describes the need to seek for alternative non-toxic earth-abundant thin film solar cell and review the progress and key limitation (V_{OC} deficit issue and J_{SC} loss in high bandgap CZTSSe) for the current-generation kesterite solar cell. In addition, hints from DFT calculation are listed that will provide useful guides to explain the non-stoichiometry observed in high-performance CZTSSe solar cells. For example, the phase stability could help to explain the J_{SC} loss while the defect physics could help to explain the $V_{OC,def}$ as described in the following chapters.

CHAPTER 2 describes experimental techniques used in this study; including new techniques that have been developed which are suitable for a versatile of thin films technology. Exfoliation process for thin films is developed to allow certain characterizations which are not accessible otherwise. Highly sensitive Rotating Parallel Dipole Line (PDL) AC Hall measurement system is also developed to obtain accurate electrical parameters which are important for emerging thin films typically with low mobility or high resistivity.

CHAPTER 3 showcases the device parameters for full bandgap range CZTSSe solar cells. As bandgap increases, $V_{OC,def}$, series resistance, and J_{SC} loss increases. Resistivity, carrier density and mobility are extracted from Hall measurement, which highlights the contribution of low carrier mobility on $V_{OC,def}$, and suggests significant interfacial resistance contributing to the J_{SC} loss.

CHAPTER 4 illustrates the relationship between defects and the induced fluctuating potential by optical PL study. The potential fluctuation is also reflected in the carrier localization frozen at low temperature. Deeper activation energy highlights the deep defect energy levels as well as the presence of significant non-radiative recombination centers in CZTSSe absorbers. All these defect physics contribute to the high $V_{OC,def}$ observed.

CHAPTER 5 probes the interfacial losses contributing to the increasing V_{OC} deficit and J_{SC} loss with higher bandgap CZTSSe. Suns-J_{SC} and Suns-V_{OC} measurements give direct evidence of non-ohmic back contact developed in high bandgap CZTSSe solar cells, which could be explained by Schottky barrier formation (as suggested by low carrier density) and the formation of high bandgap secondary phases verified by physical characterizations. Both of these contributed to high interfacial resistance and results in J_{SC} loss. Low bandgap secondary phases could also form at the *p-n* interface and contribute to the high V_{OC} deficit in CZTS.

CHAPTER 6 attempts to fabricate CZTSSe solar cell with non-toxic *solution* processing and improve the intrinsic bulk absorber by extrinsic doping. Series resistance was greatly reduced with enhanced grain growth in proportion to Sb doping concentration, but the increment of V_{OC} does not follow the trend. Optical study shows that the defect densities could be reduced by passivating non-radiative recombination centers with Sb doping. As a result, the increased V_{OC} is consistent with the reduced depth of fluctuating potential due to reduced defect density.

The last chapter, CHAPTER 7 summarizes this thesis and proposes future work with preliminary results to further improve the performance of kesterite solar cells.

CHAPTER 2 Experimental Techniques

2.1 New Experimental Techniques

2.1.1 Introduction

Hall Effect is one of the most important characterization techniques for semiconductors to probe the (majority) carrier type, carrier density, and carrier mobility. Conventional *absorber* materials like Si and GaAs are usually *p*-type doped with an moderate acceptor concentration of $n_A = (10^{15}\text{-}10^{16})$ cm^{-3}.[44] The reason for *p*-type doping is simple; because electron typically has lower effective mass and higher carrier mobility, and it is the minority carriers that traverse across the *p-n* junction for eventual charge collection. The acceptor concentration is moderately doped because too low carrier concentration will results in low conductivity, whereas too high carrier concentration will results in severe carrier scattering which lowers the minority carrier lifetime and the carrier diffusion length. Majority carrier mobility (μ_{maj}) is another important electrical property. In the conventional Si absorber with $n_A = (10^{15}\text{-}10^{16})$ cm^{-3}, μ_{maj} is larger than 400 cm^2/V.s,[45] whereas μ_{maj} for GaAs is more than 1000 cm^2/V.s.

Polycrystalline thin film photovoltaic materials (e.g. CdTe, CIGS) typically have a majority carrier concentration of 10^{14}-10^{18} cm^{-3} and a majority carrier mobility of 1-200 cm^2/V.s.[46] Different from the conventional Si or GaAs, intrinsic lattice defects form easily in CdTe and CIGS which results in the intrinsic *p*-type behaviour. Due to the low formation energy of lattice defects, doping concentration and thus the carrier concentration would be affected and this explains the vast range of reported carrier concentration.[47, 48] However, carrier concentration for CdTe and CIGS near the optimum range of $(10^{15}\text{-}10^{16})$ cm^{-3} for photovoltaic application can nowadays be well controlled after going through decades of learning curve. Therefore, it is important to probe and benchmark the electrical properties of emerging thin film materials to gauge the fundamental limitations from the macroscopic picture. Van der Pauw measurement is the most general technique for resistivity and Hall Effect measurements. The details can be found elsewhere[49] and **Figure 2-1** below depicts the measurement procedures.

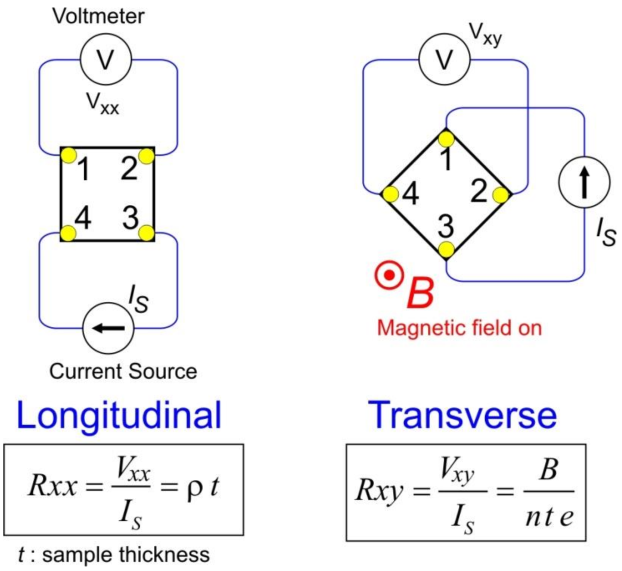

Figure 2-1. (a) Resistivity measurement which measures the longitudinal resistances (4 sides with 2 polarity each, a total of eight electrical switching states), and **(b)** van der Pauw Hall Effect measurement which measures the diagonal resistances (2 diagonals) with the effect of magnetic field (perpendicular to the sample plane).

Hall measurement on CZTSSe and CIGSSe thin films encounters two problems: (1) the quality of CZTSSe or CIGSSe crystals depends very much on the growing substrate (SLG/Mo) due to the sodium (Na) diffusion from the SLG which are serendipitous.[7] Hall measurement on CZTSSe or CIGSSe thin films grown on other insulating substrate (such as directly grown on SLG without Mo) may not truly reflect the electrical properties of the solar-grade CZTSSe or CIGSSe; (2) Hall measurement on thin films which are highly resistive and/or possess low carrier mobility (such as CZTSSe and other emerging thin films like perovskite) are plagued with low signal-to-noise ratio, which results in ambiguous Hall results.

Previous reports [50-57] assume that the quality of CZTSSe thin films grown on soda-lime-glass (SLG) and SLG/Mo substrate to be similar, so the Hall measurement were performed on CZTSSe grown directly on SLG to avoid shunting. However, Na diffusion from soda-lime-glass (SLG) through the Mo interlayer may affect the grain growth, crystal quality, and Na doping amount.[7, 55] Therefore, it is important to measure the electrical properties of the same CZTSSe absorber in the solar cell, which is grown directly on SLG/Mo. To achieve this, we need to isolate the solar-grade CZTSSe from the conducting Mo substrate; mechanical exfoliation was demonstrated to transfer the CZTSSe thin film to a secondary insulating quartz substrate.

For the second problem, difficulty often arises in Hall effect measurement for low mobility ($\mu < 1$ cm^2/V.s) or highly resistive (sheet resistance $R_{sheet} > 100$ MΩ/□) materials which typically exist in emerging thin film material, high bandgap semiconductor, organic material, intrinsic semiconductors or very thin semiconductor films (thickness < 50 nm). Hall Effect measurement in these materials, especially those with low mobility, is often plagued with noise and large drifting background due to the contribution of the large longitudinal resistance. This results in ambiguous results, such as fluctuating carrier type between different measurements.

The *easiness* of Hall Effect measurement can be gauged by the *figure of merit*, which is defined as the ratio of the transversal (R_{xy}) Hall resistance to the longitudinal resistance (R_{xx}) (**Figure 2-1**):

$$\text{Hall Figure of Merit: } R_{xy} / R_{xx} = B \cdot \mu_{\mathrm{maj}} \qquad (2.1)$$

where B is the magnetic field and μ_{maj} is the majority carrier mobility. The Hall figure of merit correlates with the signal to noise (S/N) ratio of the Hall measurement.

Therefore, a decent Hall measurement will require either a high magnetic field and/or high carrier mobility for the material under test.

To improve the S/N ratio for Hall measurement, proper electrical setup such as buffering and guarding can be employed for highly resistive samples. These tri-axial cabling and connections were typically employed in the conventional Hall measurement system with electromagnetic coil (maximum B field of 1-2 T). However, it is still not sufficient for accurate Hall measurement in highly resistive emerging thin film materials with very low mobility. Although higher B field can help to improve the S/N ratio, demanding instrumentation and extravagant cooling are required to obtain such a large B field (> 2 T) which makes routine Hall measurements unrealistic.

Alternative ways have been developed to overcome this issue, such as employing oscillating B field (AC field Hall measurement system), AC current source and lock-in detection (analog) of transversal Hall resistance (R_{xy}) signal.[58, 59] If both oscillating current and oscillating B field were used for lock-in detection, this is often referred as *double AC Hall measurement system* or *double lock-in detection technique*.[58] The lock-in detection techniques are embedded in the conventional electromagnetic coil Hall measurement system. The alternating current used for the first-stage lock-in detection normally operates at higher frequency than the B field oscillation to avoid interference and to reduce *1/f* electrical noise. Furthermore, the first-stage lock-in with oscillating current is not suitable for highly resistive sample due to the large RC (reactance & capacitance) time constant involved. Therefore, a DC current source is still preferred for Hall measurement on insulating materials. However, their applications are not widespread due to complexity of the systems and the robustness of measurement still remains a question.

In this section, mechanical exfoliation technique was first developed to isolate the CZTSSe and CIGSSe thin films from the SLG/Mo substrate. Secondly, the development of high sensitivity Hall measurement system based on a rotating parallel dipole line (PDL) configuration was presented.[60] The PDL can be realized using a pair of cylindrical diametric magnets pair (DMP) in a master-slave configuration. Using modern neodymium iron boron permanent magnet with strong B field as the DMP, this rotating DMP Hall system serves as an ideal, compact and low-cost system to implement high sensitivity AC (B field) Hall Effect measurement, eliminating the need of the bulky electromagnetic coil. Post-processing numerical lock-in detection scheme was also demonstrated to validate the obtained Hall signal and to extract the transversal Hall resistance (R_{xy}) for the calculation of carrier density and carrier mobility. The post-processing techniques are also critical for the success of the AC Hall Effect measurement system. Importantly, the self-developed AC Hall measurement is useful for a versatile for emerging thin films which are demonstrated here.

2.1.2 Thin Films Exfoliation Techniques

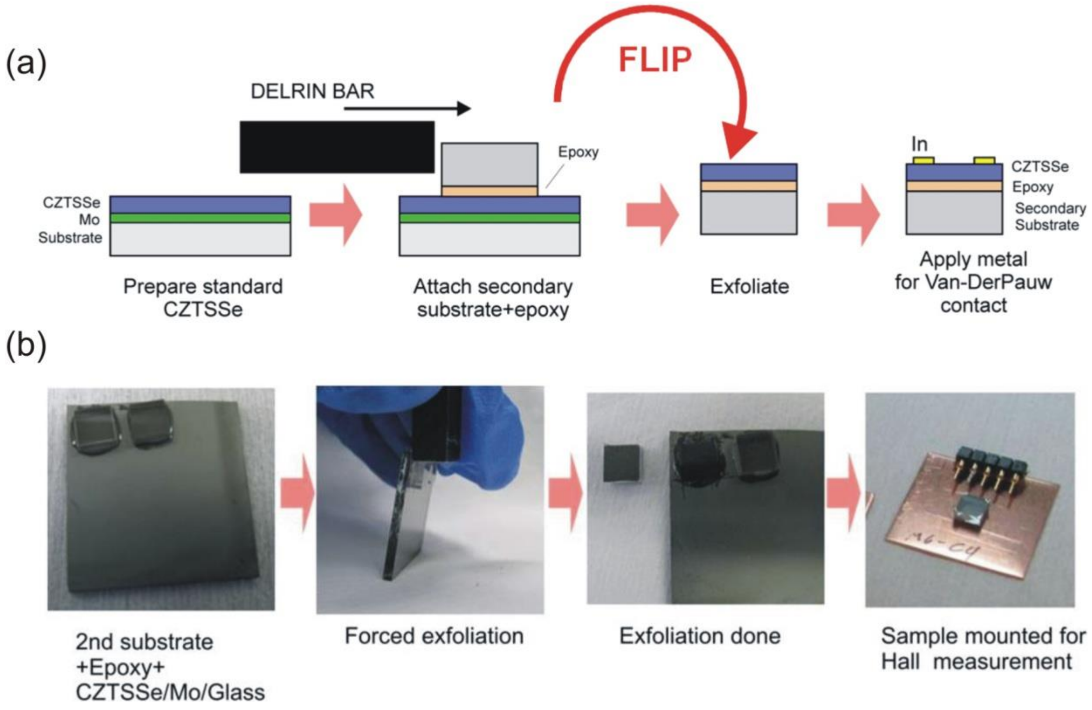

Figure 2-2. Mechanical exfoliation schematics and procedures, followed by wire-bonding for van der Pauw Hall measurement.

To perform reliable Hall measurement on the solar-grade CZTSSe thin film, isolation of the CZTSSe layer from the Mo/SLG substrate is done by mechanical exfoliation. The exfoliation procedures are shown in **Figure 2-2** above: Epoxy (Double/Bubble Epoxy Water-Clear Transparent, Mfg. Hardman Part#: 04004) was applied on a 5×5 mm secondary quartz substrate with thickness of 2 mm, followed by adhering onto the CZTSSe/Mo/SLG sample. A uniform pressure (using glass slide) was applied on the secondary quartz substrate to squeeze out bubbles formed in between epoxy. A weight was placed on top of the quartz substrate and left overnight for epoxy curing. After curing, excessive epoxy surrounding the quartz substrate was removed by cutting off using a shaving blade. Then, a Delrin bar (~ 8×8×120 mm, Mc Master Carr Part#: 8663K11) was positioned alongside with the secondary quartz substrate, and knocked off using a small hammer. The third picture of **Figure 2-2 (b)** shows the exfoliated CZTSSe film adhered on the secondary quartz substrate, while the leftover Mo substrate was clearly seen, indicating a clean exfoliation.

Physical cracks were not observed on the exfoliated films under optical or electron microscope, as shown in **Figure 5-5 (d-f)** and **Figure 5-6 (d-f)** in the following chapters. No clear features (e.g. grain boundaries, grain topography) were seen on the exfoliated films because the bottom surfaces are relatively smooth due to the flat Mo substrate. To prepare van der Pauw type samples for Hall measurement, metal contacts (Au/Al) were evaporated on the four corners of the exfoliated films using a mask. Lastly, wire bonding was done with Au wire (50 µm diameter) to connect the metal contact pads to the electrical pins as shown in the last picture of **Figure 2-2 (b)**.

2.1.3 Rotating Parallel Dipole Line AC Hall Measurement System

In this section we present the details of the rotating parallel dipole line (PDL) Hall measurement system, such as the experimental setup and the operation procedures (data acquisition and data analysis) for AC Hall measurement. The characteristics of the diametric magnet pair (DMP) system were studied by theoretical modelling and experimental measurement of the magnetic field (*B*-field) distribution, which fits very well with one another. *B*-field non uniformity issue on the finite size sample can thus be well described by theoretical modelling, which is found to be minor with ~2 % non-uniformity across a typical 5×5 mm van der Pauw sample. Finally, measurement optimization was discussed in terms of rotation frequency and minimum current source required.

A. Experimental Setup

The basic concept of the rotating PDL Hall measurement system is shown in **Figure 2-3 (a)** where two magnetic dipole lines are lined up in parallel and a sample-under-test is placed at the centre. The "master" PDL line (bottom) is rotated by an external torque and the "slave" line will mirror the motion due to ferromagnetic coupling between the two PDL lines.[60] This concept can be realized using a pair of cylindrical diametric magnets in which the *B*-field is pointing perpendicularly outwards from the surface.

Figure 2-3 (b) shows the experimental setup. In our setup, the diametric magnet which is a neodymium iron boron permanent magnet has an inner cylindrical hole so that they can be mounted on a shaft (of a stepper motor). The rotation of the master magnet (bottom) is controlled by a stepper motor whereas the slave magnet (top) is mounted on ball bearings. The slave magnet will mirror the rotation of the master magnet due to ferromagnetic coupling. Each diametric magnet has an outer radius of a = 12.7 mm, inner radius a_{in} = 3.18 mm, length L = 25.4 mm, and a uniform volume magnetization of M = 1.03×10^6 A/m, which yields a large magnetic field of ~ 1.2 T on the surface. Due to its large magnetic field, a strong coupling between the diametric magnet pair (DMP) is expected and a stepper motor equipped with a gearbox is required to provide a strong torque for magnet rotation. The torque between the two magnets in DMP system can be calculated with:

$$\vec{\tau} = \int d\tau' = \int dm_2' \times d\vec{B}_1 \qquad (2.2a)$$

where dm_2' is a small element of magnetic moment of the second magnet and $\vec{B}_1$ is the magnetic field from the first magnet on the element dm_2'. $\vec{B}_1$ is derived in Section 0, and dm_2' can be expressed as $d\vec{m}_2 = \pi a^2(\cos\theta\hat{x} - \sin\theta\hat{y})dz$. Therefore, the torque between the two diametric magnets of DMP can be estimated as:

$$\boldsymbol{\tau} = \tau_{peak} \cos 2\theta \, \hat{z} \qquad (2.2b)$$

where 2θ is the relative angle between $\vec{m}_1$ and $\vec{m}_1$, and τ_{peak} is the maximum torque between the two magnets. The torque has only z-component and it reaches the maximum values when the magnetization of both magnets are aligned (θ = 0° and 180°). Therefore, the minimum torque required to rotate the DMP system can be estimated by:

$$Minimum\ torque\ required = \tau_{peak} = \frac{\mu_0 \pi a^4 M^4}{4}\left(\frac{1}{d} - \frac{1}{\sqrt{L^2 + d^2}}\right) \qquad (2.3)$$

where μ_0 is the magnetic permeability in vacuum, and d is the distance between the centre of both magnets. The *gap* between the magnets' surface is given as: $g = d - 2a$. For instance, a gap of g = 5 mm between the DMP will require a minimum torque of 0.39 N·m to rotate the magnets.

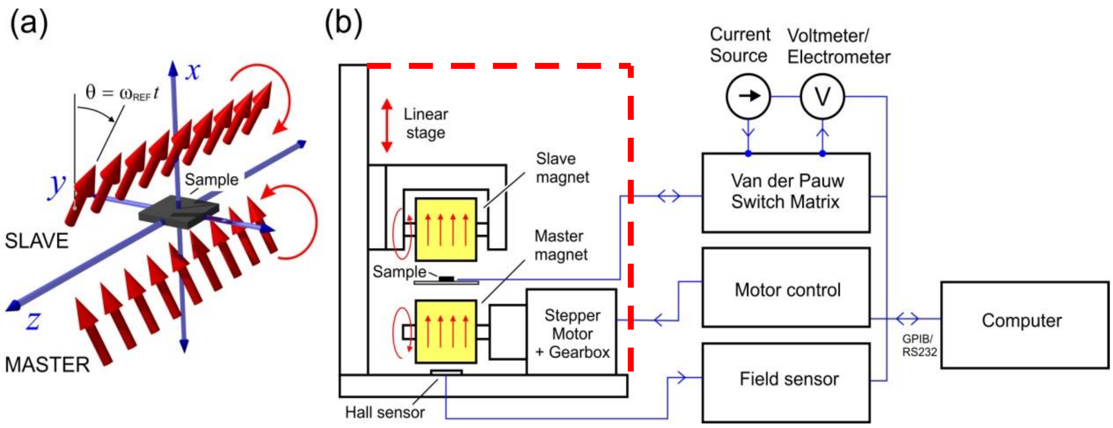

Figure 2-3. (a) Master-Slave rotating PDL configuration, **(b)** Experimental setup of rotating PDL Hall measurement system using DMP permanent magnets. During measurement, the mechanical setups (consists of the DMP and the sample) were enclosed by a Faraday cage (red dash-line) to diminish interference and electrical noise. Post-processing lock-in analysis is implemented numerically.

A gearbox with a gear ratio 27:1 is sufficient to provide the torque required for a smooth DMP rotation. The stepper motor (equipped with the gearbox) is connected to a motor control shield for the control of rotation frequency, rotation direction (clockwise or counter-clockwise) and run/stop in the continuous rotation mode (AC Hall measurement). In resistivity measurement or conventional DC Hall measurement, the motor control shield can couple with the Hall sensor to direct the DMP rotation to the targeted B-field (zero, north or south).

Wire-bonded sample (as described in **Section 2.1.2**), typically a van der Pauw type sample,[61] is mounted on a micro manipulator and positioned at the centre between the DMP. Wire-bonding on the sample is preferred over standard needle probe contacts because the latter could give rise to a double frequency ($2f_{\mathrm{ref}}$) component in the Hall Fourier spectrum due to the ferromagnetic attraction that modulates the contact resistance as the field oscillates. The upper slave magnet is mounted on a linear track that can be moved vertically to maximize B-field for sample with different thicknesses and also to ease sample loading. Besides, the gap (g) between the two magnets can be known by reading the calibre on the linear track. Therefore, the B-field on the sample is immediately known by referring to the calibrated B-field with respect to the gap between the DMP, as shown in **Figure 2-6 (d)** which will be discussed later.

As a validation for the transversal resistance (R_{xy}) obtained from the AC Hall measurement, the Hall resistance should oscillate in-phase with the B-field oscillation at the same frequency. Therefore, the rotation frequency of the magnets, which act as the reference frequency (f_{ref}) for the AC Hall measurement, should be noted. For this purpose, a Hall sensor (magnetic field sensor) was installed beneath the master magnet to record the oscillation of the magnetic field. During measurement, the whole mechanical setup mounted on the Aluminium base plate (which consists of the DMP, stepper motor, Hall sensor, sample-under-test and the linear stage) was enclosed in a Faraday metal cage to diminish electromagnetic wave interference and to reduce electrical noise. The Faraday cage also serves as the ground connection, while the guard and line of the tri-axial cabling are connected to the sample with the external current source and electrometer.

As noted in **Figure 2-1**, a complete resistivity and Hall measurement will require electrical switching through 12 electrical states (8 states for resistivity R_{xx} measurement and 4 states for Hall R_{xy} measurement) for averaging. A van der Pauw switch matrix module can be used to switch the connections between the four terminals of the sample to the current source and electrometer. Alternatively, a simpler but more expensive way is to use parameter analyzer to perform all the required tasks, *i.e.*, source current/voltage, measure voltages, read magnetic field sensor, and perform van der Pauw electrical switching. A parameter analyzer has several benefits, such as it is equipped with tri-axial guarded features for highly insulating samples to prevent current leakage in the cabling and to minimize stray capacitance for improved measurement time response. In addition, a parameter analyzer typically has a very high input resistance (> 10 TΩ) suitable to measure high-resistance ($R_{xx} > 100$ MΩ) samples.[62]

A HP4145B parameter analyzer was used here and controlled by a host computer through GPIB connection. The B-field sensor is read by a voltmeter and the motor control shield is connected to the host computer through RS232 connection. All the electrical components can be controlled by computer, in which codes were developed in MATLAB to automate the resistivity and AC Hall measurement for routine test. To avoid voltage compliance for the parametric analyzer during the measurement of insulating sample, a constant voltage source is used rather than a constant current source. This would require an additional ammeter to monitor the current flowing through the sample.

B. Data Acquisition of AC Hall Measurement

In real operation, the system performs three measurements in the following sequence:

(1) Linearity check between any of the two terminals of the van der Pauw sample,

(2) Resistivity measurement that measures the longitudinal resistances (R_{xx}) for eight electrical switching configurations at zero B-field,

(3) AC Hall measurement which captures two sets of data: B-field and transversal resistance (R_{xy}) as a function of timestamp. This step is repeated twice for two different R_{xy} (two diagonals).

The first 2 steps are quick with only a few data points to be taken, but the last step requires a significant amount of time sweep for post-data processing as explained later (validation and extraction). For semiconductors with high mobility and low resistivity, Hall signal is strong and Step (3) can be replaced with conventional DC Hall measurement by setting the magnets in discrete mode (zero, north or south) without continuous rotation. This will speed up the measurement time as only a few data points need to be taken.

Figure 2-4 (a) and **(b)** shows the raw data of B-field and R_{xy} oscillations in AC Hall measurement [Step (3)] performed on exfoliated CZTSSe thin film. This example highlights the problem encountered in highly resistive and/or low-mobility materials: the transversal resistance (R_{xy}) is rather noisy and embedded in a large drifting resistance background, typically observed in sample with high sheet resistance.

C. Data Post-Processing: Validation and Extraction of R_{xy}

Validation of Hall Signal

As the raw data is noisy in which the in-phase Hall oscillation could not be clearly observed in highly resistive samples, validation of raw data is necessary to avoid ambiguity and to ensure that the Hall oscillation is real. We employed two methods to validate the oscillation of R_{xy}:

(1) Fourier transform for both the B-field and R_{xy} oscillation.

(2) Auto correlation of the raw R_{xy} signal using power spectral density analysis (PSD).

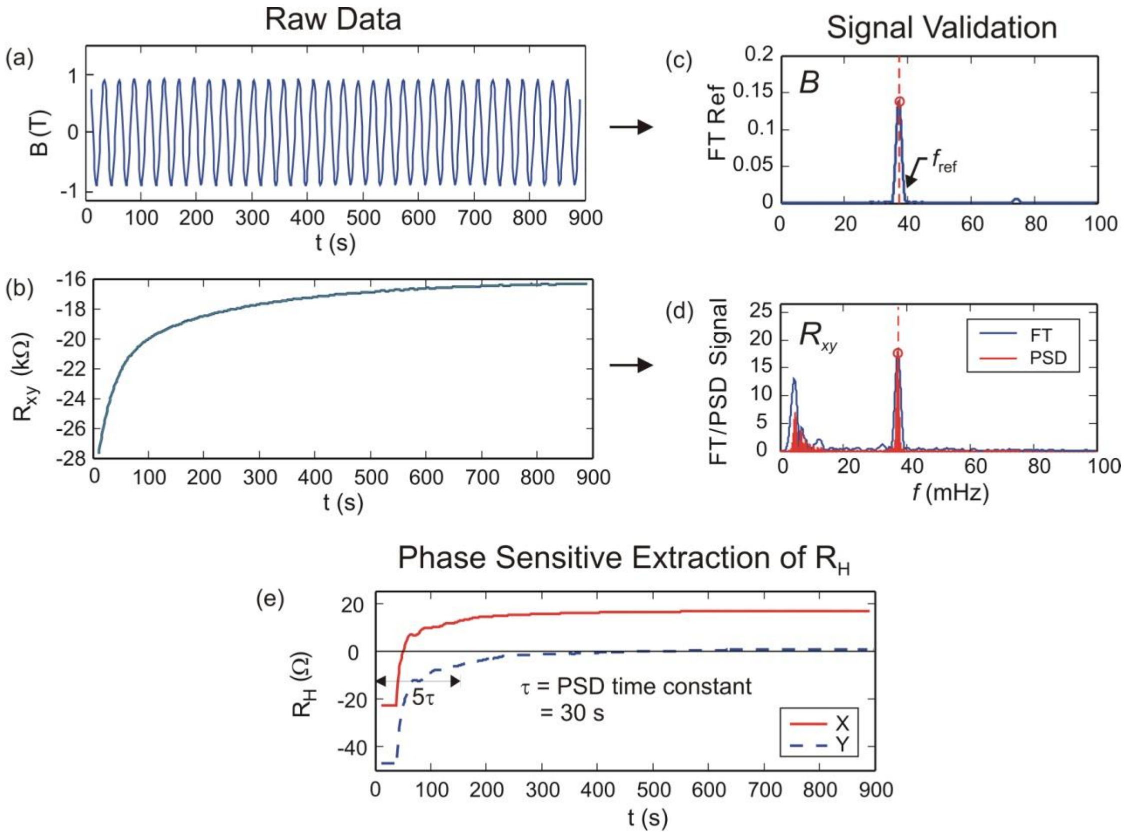

Figure 2-4. Hall signal extraction using rotating PDL Hall system: (a) B field oscillation, (b) Raw data for R_{xy} oscillation, (c) Fourier spectrum of the B field, (d) Fourier spectrum of the R_{xy}, and (e) Lock-in analysis of R_{xy}, the eventual stable value of X-signal gives the Hall resistance R_H.

In both of these methods, a polynomial background subtraction is first performed to remove the huge drifting background, as shown in **Figure 2-4 (b)**. After background subtraction, Fourier transform of the B-field and R_{xy} oscillation were done, as shown in **Figure 2-4 (c)** and **(d)** respectively. The Fourier spectrum of the R_{xy} oscillation gives a clear peak at the same frequency as the B-field (f_{ref}), suggesting the presence of real Hall signal.

The Hall signal can be further confirmed with PSD operation. PSD is essentially the Fourier spectrum of auto-correlated R_{xy} signals which accentuates the periodic signal content. By Wienner-Khinchin theorem, this is identical to the PSD of the signal. PSD method provides a more concrete assessment for validation, thus we observe that the PSD spectrum of the Hall signal is more prominent than the Fourier spectrum, and the rest of the random signals are attenuated, as shown in **Figure 2-4 (d)**. With both of these methods showing a similar frequency between the R_{xy} and the B-field oscillation, the Hall oscillation is validated to be real.

Extraction of Hall Resistance (R_H)

Once the presence of Hall signal is validated from Fourier transform and PSD method, the desired Hall resistance (R_H) can be extracted using *numerical lock-in analysis* technique. The extracted R_H will be used for the calculation of carrier density and carrier mobility by the following relations:

$$p = \frac{B}{q.R_H.t} \tag{2.4}$$

$$\mu = \frac{1}{p.q.\rho} \tag{2.5}$$

where p is the carrier density (for p-type semiconductor), q is the electron charge, t is the thickness of the thin film, μ is the carrier mobility, and ρ is the resistivity obtained from resistivity measurement.

Although the amplitude can be immediately extracted from the Fourier spectrum of R_{xy}, the measured R_{xy} may contain parasitic components such as the Faraday EMF voltage due to the changing magnetic flux (Φ_{flux}) over time. Thus, R_{xy} may not be the pure Hall resistance (R_H), especially in highly resistive sample with large RC time constant. Fortunately, the Faraday EMF contribution ($d\Phi_{flux}/dt$) resulted from the changing magnetic flux is 90° out-of-phase to the Hall oscillation. Therefore, phase sensitive analysis employing orthogonal principle can be done to differentiate the in-phase Hall signal ($X = R_H$) and the out-of-phase parasitic EMF contribution (Y), given by the following integral relations:

$$X(t) = \int_{t-\tau}^{\tau} R_{xy}(t)\sin(\omega_{ref}t)dt \tag{2.6}$$

$$Y(t) = \int_{t-\tau}^{\tau} R_{xy}(t)\cos(\omega_{ref}t)dt \tag{2.7}$$

where τ is the lock-in time constant and ω_{ref} is equal to $2\pi f_{ref}$. **Figure 2-4 (e)** shows the numerical phase-sensitive lock-in analysis of R_{xy} with a lock-in time constant (τ) of 30 s. The final Hall resistance (R_H) is extracted from the stabilized value (when $t > 5\tau$) of the in-phase Hall signal (X). In some cases, longer τ is needed to obtain a stable X value, and thus long acquisition time ($t > 5\tau$) is needed for AC Hall measurement.

Numerical (digital) lock-in analysis is preferred over the standard analog lock-in detection (using standard lock-in amplifier) due to several reasons:

(1) Lock-in time constant for the measurement is typically long. Using an analog lock-in amplifier is not practical.

(2) R_{xy} has large drifting background; performing numerical polynomial background subtraction is easier.

(3) Validation of Hall signal is required before performing lock-in detection.

(4) Numerical lock-in technique employed here is a post-data process/analysis. Therefore, phase-sensitive lock-in output can be easily repeated and plotted with *different* lock-in time constant adjusted after data acquisition. Standard analog lock-in amplifier performs lock-in detection during data acquisition, and thus varying lock-in time constant will require re-measurement which waste time.

D. Magnetic Field Distribution: Calculation Model vs. Experimental

Although the self-developed AC Hall measurement is able to avoid ambiguity and give accurate results, one concern about this AC Hall measurement with the DMP is the field uniformity (due to the cylindrical DMP) on the sample. To address this issue, we model the *B*-field distribution of a DMP system and measure the *B*-field around the DMP. A good match between the modelling and measured *B*-field indicates that the modelling is accurate, and this allows us to predict the *B*-field at *any* point around the DMP using the model.

Calculation Model

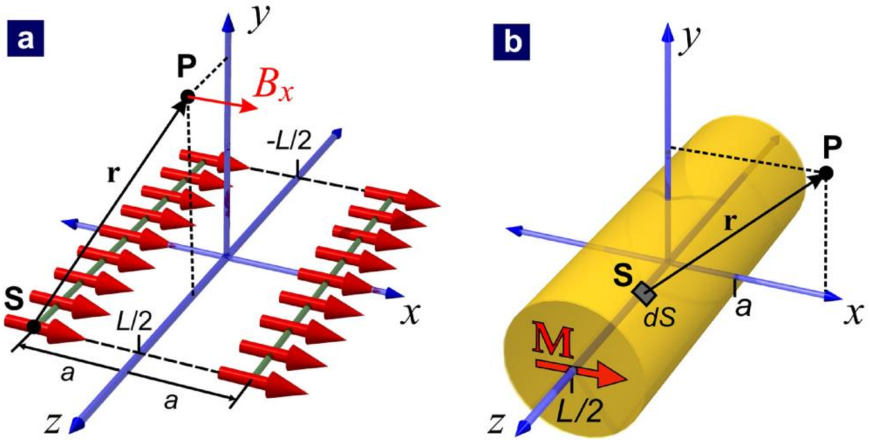

Figure 2-5. Magnetic field calculation models: **(a)** PDL model. **(b)** Diametric magnet model using scalar potential calculation (for one magnet).

Consider a single *solid* diametric magnet with uniform volume magnetization *M*, length *L*, and radius *a*, centred at the origin (x, y, z) = (0, 0, 0) in Cartesian coordinate. The *B*-field at any point around such single solid diametric magnet can be derived as:[60]

$$\mathbf{B}_M(x,y,z)=\frac{\mu_0 Ma}{4\pi}\int_0^{2\pi}\sum_{n=1,2}\frac{(-1)^n}{{u_n}^2+s^2+u_n\sqrt{{u_n}^2+s^2}}\left[x-a\cos\phi,y-a\sin\phi,u_n+\sqrt{{u_n}^2+s^2}\right]\cos\phi\,d\phi \tag{2.8}$$

where μ_0 is the magnetic permeability in vacuum, s^2 = $(x$ - a $\cos\phi)^2$ + $(y$ - a $\sin\phi)^2$, $u_{1,2} = z \pm L/2$. In this setup, the cylindrical magnet has a bore hole of radius *a*/4 for the axis shaft **Figure 2-3 (b)**, thus the superposition principle can be applied to calculate the *B*-field at any point around the hollow cylindrical magnet given by:

$$\mathbf{B}_M(x,y,z)=\mathbf{B}_{M,cyl}(x,y,z)-\mathbf{B}_{M,hole}(x,y,z) \tag{2.9}$$

Furthermore, the DMP system comprises of two cylindrical diametric magnets. Therefore, the total *B*-field at any point is given as:

$$\mathbf{B}_{DMP}(x,y,z)=\mathbf{B}_{M}(x-a,y,z)-\mathbf{B}(x+a,y,z) \tag{2.10}$$

This formula describes the magnetic field at *any point* around the DMP system. The input parameters are the geometry of the magnet (L, a) and the volume magnetization M.

B-field Measurement

To check the validity of the above model, we compare the model with the actual B-field detection around the DMP system, where the magnetization of both magnets are aligned in the $+x$ direction ($\theta = 0$). Note that the B-field has only one component (x-direction) at any angular position θ on the sample due to the mirror symmetry of the DMP system, as shown in **Figure 2-6**.

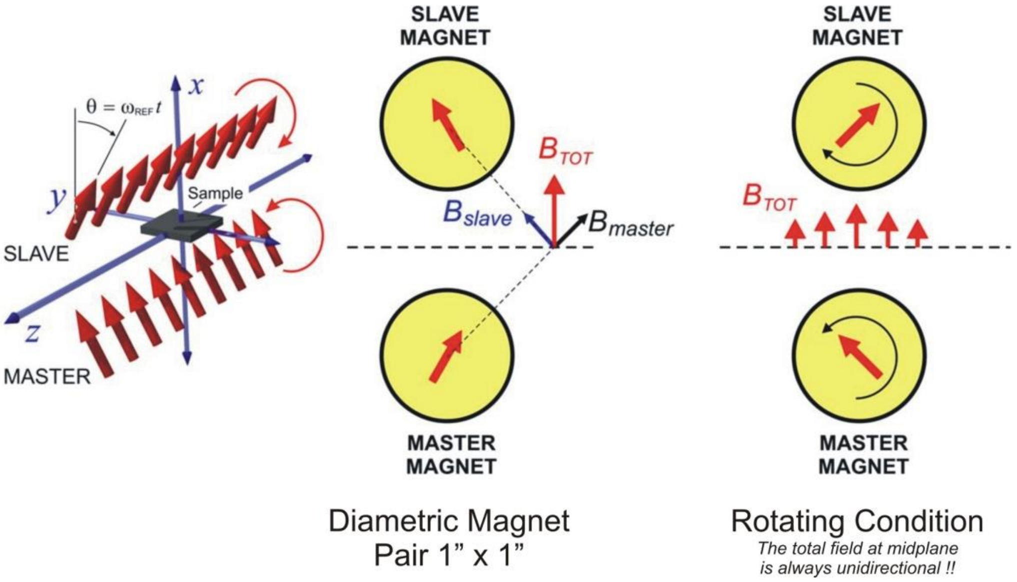

Figure 2-6. Schematics of B-field distribution on the sample plane located at the centre between the DMP. The B-field at the centre is always unidirectional and perpendicular to the sample plane (B_x).

Figure 2-7 (a-c) presents the experimental and theoretical B-field (B_x) profile in x, y, and z directions, which show a very good agreement attesting the validity of the theoretical model in Equation (2.8) - (2.10). Inversely, one could also extract the volume magnetization *M* as a single fitting parameter to the experimental data. It was also observed that the *B*-field is at the local maximum at the origin, which yields a good *B*-field uniformity across the sample positioned at the origin. **Figure 2-7 (d)** plots the theoretical and measured *B*-field at the origin as a function of the gap between the magnets' surface (*g*), which again shows the consistency between the theoretical model and the experimental data. This plot is important to quickly obtain the amplitude of the *B*-field on the sample (with *g* known from the readings of the linear track's caliber) for the calculation of carrier density and carrier mobility [Equation (2.6) - (2.7)].

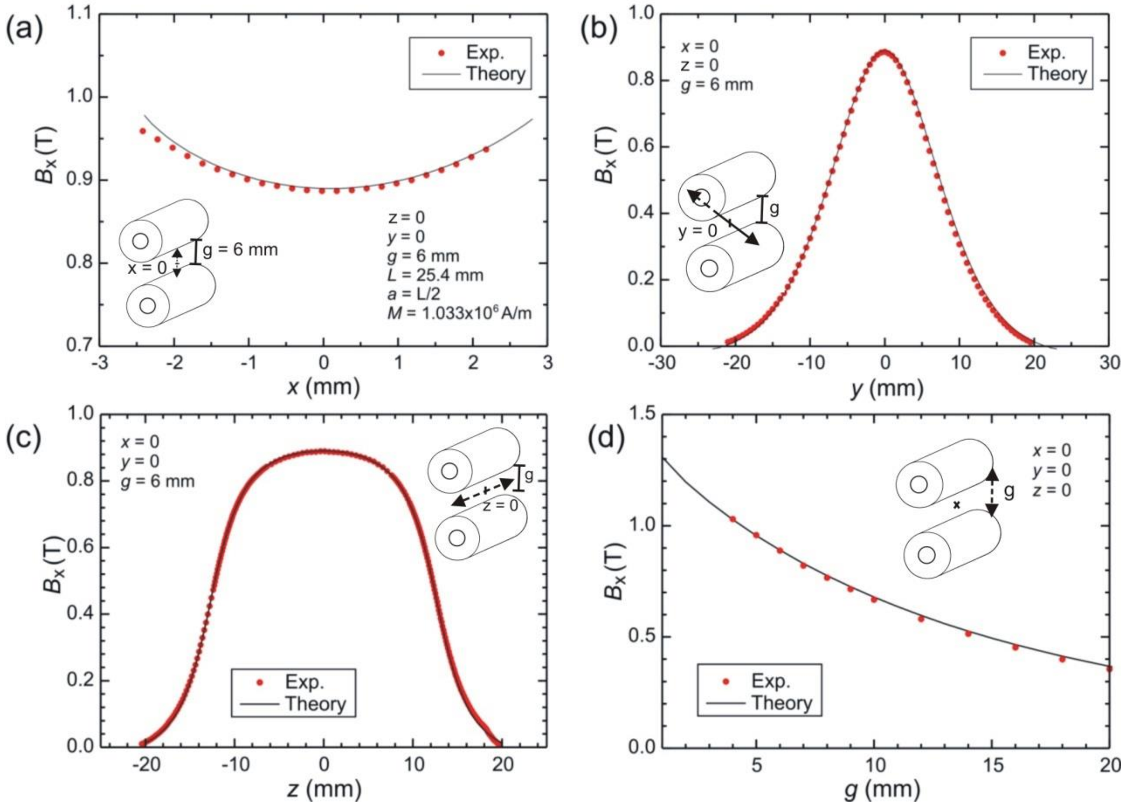

Figure 2-7. (a-c) Theoretical modelling vs. experimental B_x profile across x (fixed at y, z = 0), y (fixed at x, z = 0), and z axis (fixed at x, y = 0) respectively. **(d)** Theoretical modelling vs. experimental B_x profile at the origin [x, y, z = (0, 0, 0)] with varying gap (g) between DMP surfaces.

E. Magnetic Field Uniformity: Finite Sample Size Consideration

In **Figure 2-7 (a-c)**, it can be seen that the *B*-field is quite uniform within a certain region from the origin. If the gap between the magnets' surface is 6 mm, and the ranges for all *x*, *y*, and *z* fall within ± 3 mm from the origin [(*x*, *y*, *z*) = (0 ± 3, 0 ± 3, 0 ± 3 mm)], then a large *B*-field (> 0.8 T) and a good field uniformity can be obtained at the same time. This will result in peak-to-peak *B*-field amplitude of 1.6 T for the AC Hall measurement, which is comparable to the standard bulky electromagnetic coil system in the conventional DC Hall measurement.

To better quantify the field uniformity on a sample-under-test with a finite size, the uniformity of *B*-field can be evaluated for a test square sample with side *s*. We can define the *field uniformity parameter* across a finite-size sample as:

$$\eta = \frac{\sigma_B}{\bar{B}} \tag{2.11}$$

where σ_B is the standard deviation of the *B*-field and $\bar{B}$ is the mean magsnetic field across the sample area *S* given as:

$$\sigma_B^2 = \int (B - \bar{B})^2 \, dS/S \tag{2.12}$$

$$\bar{B} = \int B \frac{dS}{S} \tag{2.13}$$

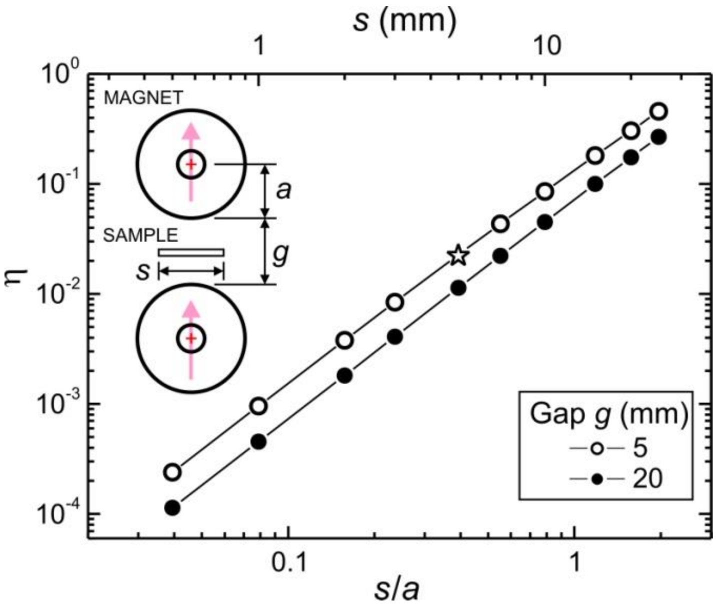

Figure 2-8. Non uniformity parameter (η) of the *B*-field as a function of sample edge length (*s*) for two magnets' gap parameters (5 and 20 mm). A typical sample with *s = 5 mm* yields a *B*-field non-uniformity of *η = 2.1 %,* as indicated by the star symbol.

The uniformity parameter (η) across a sample size of *s* = 5 mm is plotted with two gaps between the magnets' surfaces (g = 5, 20 mm), as shown in **Figure 2-8**. For a typical sample size of *s* = 5 mm and a DMP gap of *g* = 5 mm, the non-uniformity is very small with just *η* = 2.1 %. The field non-uniformity only becomes enormous when the sample size increases or the DMP gap decreases.

F. Measurement Optimization

Aside from material properties and the magnetic field strength [Equation (2.1)], several other parameters could affect the quality of the AC Hall measurement. Consider a rotating magnetic field with $B = B_0 \cos(\omega t)$, the voltage measured across the two diagonal terminals is given as:

$$V_{XY}(t) = \frac{I_S B_0 \cos\omega t}{p\,q\,t} + B_0 \omega A \sin\omega t + \alpha I_S R_{xx} \tag{2.14}$$

where I_S is the current source. The first component (X) of Equation (2.14) is in-phase with the *B*-field oscillation, which is the desired Hall voltage for the extraction of carrier density (p). The last component, $\alpha I_S R_{xx}$, is the background voltage due to some mixture with the longitudinal resistance R_{xx} with a fraction $|\alpha| < 1$ originated from the asymmetry or inhomogeneity of the van der Pauw sample. The middle component is the out-of-phase (with respect to B-field oscillation) parasitic signal (Y) which results from Faraday EMF contribution ($d\Phi_{\text{flux}}/dt$) due to changing magnetic flux in a wiring loop with effect A.

For a successful Hall signal extraction, it is desired to have $X \gtrsim Y$ or $I_S \gtrsim \omega A n d e$, which can be obtained by operating with high current source I_S, minimized effective wiring loop area A, and operates at sufficiently low angular frequency ω (rotation frequency of DMP). However, the operating frequency cannot be too low for the system because the noise density will become larger at lower frequency (due to the general $1/f$ noise). This will result in a longer time constant for the measurement. In general, a good operating frequency can be achieved with DMP rotation frequency in the order of 1 - 2 rpm (rotation per minute) or f = 16.7 - 33.3 mHz. The current source I_S is also limited by the maximum voltage compliance or maximum input voltage of $V \leq 200$ V in typical parameter analyzer.

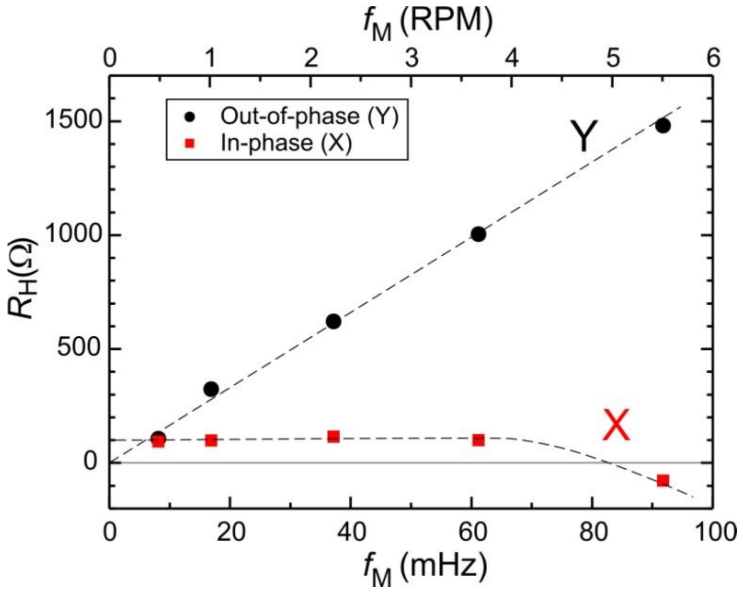

Figure 2-9. In-phase (X) R_{xy} signal and out-of-phase (Y) parasitic component of the lock-in resistance output (R_H) measured on CZTSSe sample by rotating PDL Hall system.

Figure 2-9 shows the experimental data for both the in-phase (X) and out-of-phase (Y) signal for the AC Hall measurement of exfoliated CZTSSe thin film as a function of operating frequency. It was observed that the in-phase X component remains constant below 60 mHz. The out-of-phase Y component is proportional to the operating frequency, consistent with second term in Equation (2.14). At high operating frequency (> 60 mHz), the out-of-phase signal becomes much larger and dominates the R_{xy} signal, resulting in a distorted in-phase X component.

Based on the slope of the out-of-phase Y signal vs. frequency, the effective area A of the wiring loop can be deduced, with A = 74 mm^2. Given the area of our sample to be 25 mm^2, A is reasonable considering there is additional wiring loop area due to the cabling connections to the terminals. Since a typical effective loop area is more or less constant in this experiment, this gives a minimum current source I_S of ~2.5 nA for an operating frequency of f_{ref} = 2 rpm, A = 74 mm^2, $p = 10^{15}$ cm^{-3}, and film's thickness of t = 1 µm.

Occasionally, it was noted that the PSD spectra of the Hall signal is very noisy and the existence of the Hall Fourier component become questionable. Nevertheless, the measurement can still provide useful information by establishing the bounds of the measurement as the peak amplitude of the Fourier transform at the reference frequency will serve as the upper limit of the possible Hall resistance (R_H) - this yields the upper limit on the calculated carrier mobility and the lower limit of the carrier density.

2.2 Other Experimental Techniques

2.2.1 Current Density-Voltage (*J*-*V*) Sweep

White Light and Colour J-V Sweep

Dark and light J-V curves for the solar cells were tested using the solar cell I-V characterization system equipped with 6" x 6" beam solar simulator from Newport. The system is equipped with a close-loop light stabilization system to ensure stable 1 sun (100 mW/cm^2) illumination with a simulated air mass of 1.5 global (AM1.5G) spectrum. A custom-built software was used to perform the I-V sweep using a Keithley 2400 source meter.[63] To perform color J-V measurement, color-filters (long-pass and short-pass filters with cut-off wavelength at 600 nm, denoted by LP600 and SP 600 respectively) were inserted between the light source and the device-under-test for J-V sweep under various illumination conditions.

Parameters Extraction

The solar cell diode parameters (ideality factor n, series resistance R_S and shunt resistance R_{Sh}, reverse saturation current I_0, photocurrent I_{Ph}) were extracted using curve-fitting method described by Zhang et al. based on Lambert-W function.[64] This method provides a simpler and more accurate curve fitting calculation by fixing the fitted J-V curve to pivot at the V_{OC} point.

Briefly, this method fits the experimental I-V curve under one constant illumination level to extract n, R_S and R_{Sh} based on the single-diode model described by:

$$I = I_0\left[\exp\left(\frac{q(V - R_S I)}{nk_B T}\right) - 1\right] + \frac{V - R_S I}{R_{Sh}} - I_{Ph} \qquad (2.15)$$

where q is the electron charge, k_B is the Boltzmann constant, and T is the temperature. However, Equation (3.1) is an *implicit* function which the right side of the equation include the independent (V, T) and the dependent (I) variables at the same time. This two-dimensional fitting increases the complexity and difficulty of the parameter extraction which usually introduces large errors. Therefore, Equation (2.15) is expressed in *explicit* analytic equation with the help of Lambert W-function. Lambert W-function (denoted by W or *lambertw*) is the inverse function of $f(W) = We^{W}$. For example, given $y(x) = xe^x$, the component $y(x)$ can be solved easily if x is given. However, if given y and asked to solve for x, the solution for x will be the inverse of y, which is y^{-1} [or *lambertw*(y)]. The *lambertw*(y) can be solved numerically by Newton's method, and the function is embedded in *Matlab* as "*lambertw*", e.g. The solution for x in the equation: $1 = xe^x$ is $x = lambertw(1) = 0.5671$.

The below derivation simplify Equation (2.15) to an explicit analytic expression. At short-circuit condition (I = - I_{SC} and V =0) and open-circuit condition (I = 0 and V = V_{OC}), Equation (2.15) can be written as:

$$-I_{SC} = I_0\left[\exp\left(\frac{qR_S I_{SC}}{nk_B T}\right) - 1\right] + \frac{R_S I_{SC}}{R_{Sh}} - I_{Ph}, \qquad (2.16a)$$

$$0 = I_0\left[\exp\left(\frac{qV_{OC}}{nk_B T}\right) - 1\right] + \frac{V_{OC}}{R_{Sh}} - I_{Ph}, \qquad (2.16b)$$

Combining Equation (2.16a) and (2.16b), and assuming:[64]

$$\exp\left[\frac{q(R_S I_{SC} - V_{OC})}{nk_B T}\right] \ll 1 \qquad (2.16c)$$

I_0 and I_{Ph} can be derived as:

$$I_0 = \left(I_{SC} + \frac{R_S I_{SC} - V_{OC}}{R_{Sh}}\right)\exp\left(\frac{-qV_{OC}}{nk_B T}\right), \qquad (2.17a)$$

$$I_{Ph} + I_0 = I_{SC} + \frac{R_S I_{SC}}{R_{Sh}}. \qquad (2.17b)$$

Therefore, equation (2.15) is reduced to:

$$\begin{aligned} I = \frac{V}{R_S} - I_{SC} - \frac{R_{Sh}V}{R_S(R_S + R_{Sh})} \\ + \frac{1}{V_T R_S}\boldsymbol{lambertw}\left[V_T R_S\left(I_{SC} - \frac{V_{OC}}{R_S + R_{Sh}}\right)\exp(-V_T V_{OC})\right. \\ \left. \times \exp(V_T)\left(R_S I_{SC} + \frac{R_{Sh}V}{R_S + R_{Sh}}\right)\right] \qquad (2.18) \end{aligned}$$

where $V_T = q/nk_B T$. Note that Equation (2.18) is an explicit expression with the independent variable on the right side, and the number of unknown parameters is reduced from five (I_0, I_{Ph}, n, R_S, and R_{Sh}) to only three parameters (n, R_S, and R_{Sh}). Thus, this reduced equation is more efficient and accurate to extract the device parameters.

2.2.2 External and Internal Quantum Efficiency

The spectral response of the solar cell was tested using external quantum efficiency (EQE). EQE measurements were performed using chopped-light and a monochromator system from Protoflex. The system was modified such that two lock-in amplifiers were employed for lock-in photocurrent detection from the cell under test and the other to monitor light fluctuation as a base reference to improve the signal/noise ratio.

By measuring the reflectance of the device, internal quantum efficiency (IQE) or internal photon conversion efficiency (IPCE) can be calculated from the relation:

$$IQE = \frac{EQE}{1 - R} \tag{2.19}$$

There is no light transmitted in the Mo/CZTSSe/CdS/ZnO/ITO/Ni-Al substrate devices, hence transmittance (T) can be excluded in the denominator of Equation (2.19).

2.2.3 Photoluminescence

Power- & Temperature-Dependent Photoluminescence

The PL spectra were recorded by a Hamamatsu time-correlated single photon counting (TCSPC) system equipped with an InGaAs photo-multiplier (PMT) detector pre-cooled to -80 °C before measurement. A solid state laser was used to excite the sample. The laser has a repetition rate of 15 kHz with pulse duration of 1 ns and a wavelength of 532 nm. Power-dependent PL measurements were performed by altering the laser power with the laser beam passing through a calibrated motorized neutral density filter before reaching the sample. To calibrate the laser beam spot size, a pinhole with well-defined diameter of 127 µm was used. The laser beam has a Gaussian TEM_{00} profile and the laser intensity after passing through the pinhole with radius r can be described by: $I(r) = I_0 \exp(-ln2 \times r^2/b^2)$, where I_0 is the original laser intensity, and b is the beam radius at full-width-half-maximum (FWHM) intensity. By measuring the laser power with ($I(r)$) and without (I_0) the pinhole (diameter of 127 µm), the beam radius was found to be 171 µm. Therefore, the laser intensity (laser power/πb^2) and laser fluence (laser intensity/15 kHz) can be calculated accordingly. For temperature-dependent PL, the sample was placed in a Janis SuperTran-VP continuous liquid He flow cryostat and using a Cryocon temperature controller integrated into the system.

Time-Resolved Photoluminescence (TRPL)

The recombination lifetimes at different photon energies were probed at 7 K to gauge the degree of carrier localization in the different materials. The lifetime measurements were recorded using as low as possible laser fluence (rate of success in Poisson probability of < 15%) to avoid a high carrier injection which lowers the measured lifetime due to nonlinear effect. All PL measurements were carried out on completed CIGSSe and CZTSSe solar cell devices. No difference was found in PL measurements between the device and bare film.

2.2.4 Suns-V_{OC} and Suns-J_{SC}

Suns-V_{OC} was measured using the Sinton Tool Suns-V_{OC} illumination voltage tester on the finished devices (Z1-Z6).[65] To achieve high light-intensity of up to ~300 suns, the neutral density filter (NDF) was removed from the light source and an additional NDF was added in front of the photo-detector that monitors the Suns intensity (to prevent saturation). The flash light lasts for about 15 ms, with the light intensity and the V_{OC} recorded concurrently as the light decays quickly from ~300 suns to 0.3 suns. The measurement can be repeated with a small shunt resistance (R = 1 Ω) connected across the device-under-test (parallel connection) to measure J_{SC} (Suns-J_{SC} measurement). Therefore, Jsc-V_{OC} plot was obtained by combining separate Suns-V_{OC} and Sun-J_{SC} measurements.

To probe the depth sensitivity, optical band-pass filters (SP600 and LP600) were inserted between the light source and the device-under-test during Suns-V_{OC} and Suns-J_{SC} measurement. Illumination with longer wavelength penetrates deeper/closer to the back contact due to a lower absorption coefficient. More details of the measurement technique can be found in Ref.[66]

2.2.5 Physical Characterizations

Glancing Incidence X-Ray Diffraction (GIXRD)

Glancing-incidence X-ray diffraction (GIXRD) with Cu Kα X-ray (λ = 1.54 Å) was performed on the CZTSSe bare films grown on Mo-substrate (sisters' films to Z1-Z6, denoted by Z1'-Z6') using Bruker D8 Advance X-ray diffractometer. In GIXRD, the X-ray source-arm is fixed at a glancing angle with respect to the sample's surface. Glancing incidence angles of 1°, 2° and 10° were used to probe the depth-sensitivity of related phases on the as-grown CZTSSe (Z1'-Z6') thin films on Mo/SLG substrate. GIXRD with all three incidence angles were performed consecutively without moving the sample as to ensure the depth sensitivity is accurate for each set of data.

Field-Emission Scanning Electron Microscopy (FE-SEM)

Field-emission scanning electron microscope (FE-SEM, JEOL JSM-7600F) was used to image the morphology of the as-grown CZTSSe films on Mo/SLG substrate (Z1'-Z6'), exfoliated CZTSSe layers on secondary quartz substrate (exfoliated Z1'-Z6'), and the left-over regions on the Mo substrate after exfoliation (Leftover Z1'-Z6'). No pre-coating of metallic films was performed on the samples before imaging, so that charging effect (typically on high E_g materials) could be observed to differentiate the insulating secondary phases and the semiconducting CZTSSe.

Raman Mapping

Micro-Raman mapping (LabRAM Aramis from Horiba JobinYvon) was performed on Z1'-Z6', exfoliated Z1'-Z6', and Leftover Z1'-Z6'. The Raman scattering system is equipped with laser excitation wavelength of 514 nm and focused with a 50x optical lens onto the samples. Raman mapping was done on a random area of 135×135 μm^2 by a point-by-point (81 points in total) scan with a grid size of 15×15 μm^2, where the sample is moved by a *x*-*y* motorized translation sample stage. Raman mapping on each sample results in 81 Raman spectrum. Raman mapping was done to ensure that the overall phonon vibrations for the respective sample was well represented, not just by a single point Raman scan.

X-Ray Photoelectron Spectroscopy (XPS) & XPS Depth Profile

To investigate the chemical composition and chemical environment at the back interface, surface-sensitive X-ray photoelectron spectroscopy (XPS, Omicron) and XPS depth profiling were performed on the exfoliated-Z6' inside ultrahigh vacuum chamber. A wide scan was performed followed by narrow scan on each element (Cu *2p*, Zn *2p*, Sn *3d*, S *2p*- Se *3p*). To derive the elemental composition, peaks related to each element were fitted using Gaussian-Lorentzian profile after Shirley background subtraction (with XPSPeak software). As the detection sensitivity varies between different element, the integrated area of the fitted peak was divided by the relative sensitivity factors (RSF) of the respective element (RSF for Cu *2p*: 4.2; Zn *2p*: 4.8; Sn *3d*: 4.3; S *2p*: 0.54; Se *3p*: 1.05) to obtain the actual peak area for the respective element. The atomic % for each element was then calculated by dividing the actual area (of the fitted peak) for the respective element to the total actual areas for all the elements (Cu, Zn, Sn, S, Se). Depth profiling was done by Ar^+ sputtering followed by XPS scans (wide and narrow scans), which was repeated with different sputtering duration until the elemental composition stabilize (reaches the bulk). Similar fitting process was done to calculate the elemental atomic % at each sputtered layer. Preferential sputtering of elements can be neglected here as all the elements' atomic % stabilized to constant value after certain sputtering duration.

2.3 Fabrication of CZTSSe & CIGSSe Thin Films and Solar Cells

All thin films and solar cells were provided by IBM T.J. Watson Research Center. Fabrication of thin film absorbers, hydrazine solution preparation and spin coating were performed in a nitrogen-filled glove box. *Caution: hydrazine is highly toxic and explosive and must be handled using appropriate protective equipment to prevent physical contact with either vapor or liquid.* For CIGSSe, the precursor solutions were prepared by dissolving separately In_2Se_3 with Se addition and Cu_2S with S addition, followed by mixing the individual solution. A single layer of 120 nm thick was first spin-coated from a 0.3 M CIGSSe solution with slightly higher Ga content $Cu_{0.92}In_{0.72}Ga_{0.28}(S,Se)_2$ onto a Mo-coated soda lime glass substrate, followed by three layers spin-coated from a 1.1 M CIGSSe solution with $Cu_{0.92}In_{0.8}Ga_{0.2}(S,Se)_2$ composition, resulting in a film thickness of ~2 μm. The film was annealed on a ceramic hot plate with a temperature of 540°C as described previously.[23, 67] Devices were completed with chemical-bath-deposited CdS (60 nm), RF magnetron sputtered ZnO (80 nm), and indium-doped tin oxide (ITO, 130 nm).

For CZTSSe with varying S/(S+Se) ratio, five CZTSSe thin films and solar cell devices (denoted by Z2-Z6) with E_g of 1.08, 1.20, 1.28, 1.38, 1.49 eV (extrapolated from EQE measurement) were fabricated. The CZTSSe films were processed using hydrazine pure-solution approach, following the procedures described in Ref.[24, 68, 69] and targeting a Cu-poor and Zn-rich compositions (Cu/(Zn+Sn) = 0.8 and Zn/Sn = 1.1) in the precursor solution for all Z2-Z6. To control the S/(S+Se) ratio, hydrazine-based pure S-solution and high-Se-content-solution were prepared individually and later mixed in appropriate ratios. Multiple layers were spin-coated onto Molybdenum-coated soda lime glass followed by annealing at a temperature in excess of 500°C.[24, 68, 69] The thickness of the annealed films were probed by cross-sectional field-effect scanning electron microscopy (FE-SEM) and found to be ~1.7 µm for Z2-Z5, and ~0.9 µm for Z6. Thicker film of Z6 is not successfully synthesized as significant cracks will be developed. For complete solar cell devices, 25 nm of CdS was deposited on the annealed CZTSSe films by chemical-bath deposition, followed by deposition of 10 nm ZnO and 50 nm ITO layers with RF magnetron sputtering.[24, 68, 69]

Finally, a 2 µm thick Ni-Al collection grid and 110 nm thick MgF_2 antireflection coating were deposited on all the CIGSSe and CZTSSe devices by electron-beam evaporation. The device area of approximately 0.45 cm^2 was defined by mechanical scribing. Besides Z2-Z6, a pure-selenide record CZTSe thin film (E_g = 1.0 eV, absorber's thickness of ~2.0 µm) and device (denoted by Z1) fabricated by co-evaporation was added for comparison.[19]

2.4 Conclusion

In summary, we have developed an exfoliation process to isolate the solar-grade CZTSSe thin film from the Mo/SLG substrate. A high sensitivity AC Hall measurement system was also developed based on rotating parallel dipole line (PDL) concept utilizing a diametric magnet pair (DMP) system. The DMP system has an ideal configuration to perform AC Hall measurements due to several reasons, such as large and uni-directional magnetic field (*x*-direction) on the sample, good uniformity of magnetic field with merely 2% of non-uniformity on a typical 5×5 mm sample, compact and low cost with no cooling required etc.

Numerical lock-in analysis is also critical for the success of our AC Hall measurement. It validates the Hall signal and extracts the in-phase Hall resistance for the calculation of carrier density and carrier mobility. This system enables Hall measurement in a versatile of thin films with high sheet resistance, low carrier density and/or low carrier mobility. Electrical properties of challenging thin film materials, such as CZTSSe, CIGSSe, Zn(O,S) (for Cd-free buffer),[70] MoO_3, Cu_2O, lead perovskite $CH_3NH_3PbI_3$ have been successfully extracted using our AC Hall measurement. AC Hall measurements on CZTSSe and CIGSSe thin films will be showcased in **Section 3.3**, other examples will be demonstrated in **Appendix** .

Additional features could be added into the current rotating PDL Hall system. For example, the DMP system can be implemented in a cryostat for temperature-dependent Hall measurement, where a small slave diametric magnet can be placed inside the cryostat with the master magnet located outside of the cryostat. Furthermore, the DMP system can also be utilized for other experiments, such as the photo-electromagnetic (PEM) effect measurement for the extraction of important parameters (carrier lifetime, density, mobility, diffusion length etc.) for both the majority and minority carriers.[71, 72]

CHAPTER 3 Electrical Properties of Thin Film Polycrystalline $Cu_2ZnSn(S_xSe_{1-x})_4$

3.1 Introduction

The current best kesterite solar cell with 12.6% power conversion efficiency (PCE) is achieved by polycrystalline $Cu_2ZnSn(S_xSe_{1-x})_4$ (CZTSSe) thin film solar cells with bandgap (E_g) of 1.13 eV.[20] The Shockley-Queisser (SQ) limit predicts that a solar cell with E_g of 1.13 eV has a *theoretical maximum* open-circuit voltage (V_{OC}) of *883 mV* and a short-circuit current density (J_{SC}) of *43.4 mA/cm^{-2}*. However, the experimental device parameters for the record CZTSSe solar cell has much lower V_{OC} of *513 mV* and J_{SC} of *35.2 mA/cm^{-2}*,[20] which corresponds to *58% of the SQ-V_{OC} and 81% of the SQ-J_{SC}*. In the case of the record $Cu(In,Ga)Se_2$ (CIGSe) solar cell with the same E_g of 1.13 eV, the performance was much better with PCE of 21.7%, V_{OC} of 748 mV (*85% of SQ-V_{OC}*) and the J_{SC} is 36.5 mA/cm^{-2} (*84% of SQ-J_{SC}*).[73] The large difference in V_{OC} between these two solar cells clearly indicates the V_{OC} deficit issue in CZTSSe solar cells. V_{OC} deficit, defined as the bandgap divided by Coulomb charge and subtracted by V_{OC} ($V_{OC,def} = E_g/q - V_{OC}$) poses the biggest hurdle for CZTSSe solar cells. The large $V_{OC,def}$ in CZTSSe also lowers the fill factor (FF) to 69.8% by the empirical relation between V_{OC} and FF,[38] which is comparably lower than the FF of 79.4% in the record-CIGSSe solar cell.[20, 73]

The bandgap of the current generation $Cu_2ZnSn(S_xSe_{1-x})_4$ solar cells is tuneable by controlling the S/(S+Se) ratio, ranging from 1.0 eV in the pure selenide $Cu_2ZnSnSe_4$ (CZTSe) to 1.5 eV in the pure sulphide Cu_2ZnSnS_4 (CZTS) absorbers. Intuitively, V_{OC} can be enhanced by increasing the E_g through S/(S+Se) ratio in CZTSSe. Indeed, V_{OC} increases with higher S/(S+Se) ratio. Unfortunately, the *$V_{OC,def}$*

increases at a larger degree. In other words, the increment of V_{OC} with E_g in CZTSSe solar cells falls short from expectation. In addition, the *J_{SC} loss* resulted from the reduced light absorption with increased E_g is more severe compared to the SQ prediction of J_{SC} (SQ-J_{SC}). For instance, with *$E_g = 1.45$ eV*, the *SQ Limit* predicts a solar cell *PCE = 32.7%, $V_{OC} = 1.18$ V*, and *$J_{SC} = 30.8$ mA/cm^2*.[74] However, the pure sulphide record CZTS solar cells (E_g = 1.45 eV) with a PCE of 8.4% has a V_{OC} of merely 661 mV (*55.9% of SQ-V_{OC}*) and J_{SC} of 19.5 mA/cm^{-2} (*63.3% of SQ-J_{SC}*),[17] which poses a huge loss in both V_{OC} and J_{SC} as bandgap increases. Therefore, the current record CZTSSe solar cell with E_g of 1.13 eV is achieved by making a good balance between J_{SC} and $V_{OC,def}$. In-depth investigation has to be done to understand: **(A)** the significant V_{OC} deficit issue in CZTSSe compared to CIGS(Se) solar cell, and **(B)** the increasing $V_{OC,def}$ and J_{SC} loss observed in CZTSSe solar cells with higher S/(S+Se) ratio.

In this chapter, a series of high performance $Cu_2ZnSn(S_xSe_{1-x})_4$ solar cells and thin films with E_g ranging from 1.0 - 1.5 eV were characterized electrically. To assess the fundamental limitation of solution-processed CZTSSe, it is useful to compare with state-of-the-art $Cu(In,Ga)(S,Se_2)$ (CIGSSe) solar cell and thin film fabricated by the same solution processing technique. The solar cell device parameters were characterized by current density-voltage (J-V) measurement under solar simulator equipped with AM1.5G sunlight. The spectral response were characterized by Quantum Efficiency (QE) measurement and E_g was intrapolated from the inflection point of d(QE)/dλ. To obtain the important electrical properties, the CZTSSe and CIGSSe thin films grown on Molybdenum (Mo) substrate were isolated by mechanical exfoliation and characterized using self-developed Rotating Parallel Dipole Line (PDL)

Hall measurement system (as described in **CHAPTER 2**) for the extraction the resistivity (ρ), majority hole concentration (*p*), and hole mobility (μ_h).

In summary, V_{OC} deficit is generally large in CZTSSe and increases with E_g. In addition, J_{SC} loss is also observed in high E_g CZTSSe as a result of the increasing series resistance. Resistivity measurement indicates that the interfacial resistance could be the dominant factor for the J_{SC} loss in high E_g CZTSSe solar cells. This will be discussed in more details in CHAPTER 5. Furthermore, Hall Effect measurement shows a decreasing net carrier concentration as E_g of CZTSSe increases. Nevertheless, the optimum carrier concentrations of 10^{15}-10^{16} cm^{-3} for photovoltaic application were observed for all CZTSSe, similar to the carrier concentration in CIGSSe and other solar cell materials. For the hole mobility, CZTSSe generally have low μ_h compared to CIGSSe. This partly explains the low V_{OC} in CZTSSe as low μ_h will subject to more recombination losses. However, the hole mobility does not depend on E_g, and thus further investigations were required to explain the increasing $V_{OC,def}$ with E_g, which will be discussed in more details in CHAPTER 4.

3.2 Electrical Characteristics of $Cu_2ZnSn(S_xSe_{1-x})_4$ Solar Cells

The light (LJV) and dark J-V (DJV) curve of the studied CZTSSe (represented by Z3 with S/(S+Se) = 0.34) and CIGSSe were plotted in **Figure 3-1(a)** and **(c)** respectively. The LJV curves for all the CZTSSe (Z1-Z6) and CIGSSe were fitted using Lambert-W function described previously. The fitted curves match the experimental LJV curves perfectly, indicating an accurate fit and extraction for the device parameters. Spectral responses were tested by quantum efficiency measurement, as shown in **Figure 3-1(b) and (d)** for the full bandgap (E_g) range of CZTSSe (Z1-Z6) and CIGSSe solar cells, respectively. We differentiate the quantum efficiency data so that E_g was intrapolated from the inflection point of the differentiation d(QE)/dλ. The E_g for CZTSSe ranges from 1.00 (Z1), 1.08 (Z2), 1.20 (Z3), 1.28 (Z4), 1.38 (Z5), to 1.49 eV (Z6), whereas the E_g for CIGSSe is 1.16 eV. The device parameters and E_g are summarized in **Table 3-1** and **Figure 3-2**.

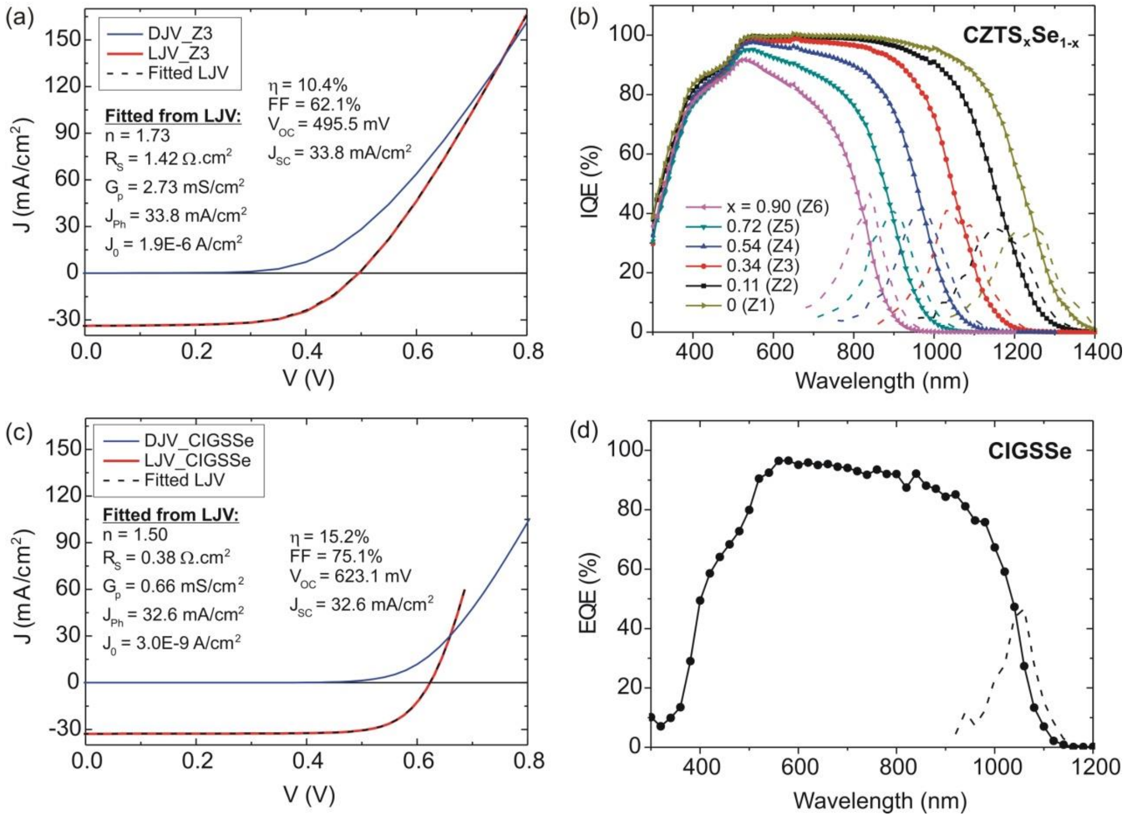

Figure 3-1. DJV and LJV curves for **(a)** CZTSSe (Z3) and **(c)** CIGSSe devices, with listed device parameters fitted with the help of Lambert W-function. Quantum efficiency data for **(b)** full bandgap range CZTSSe (Z1-Z6) and **(d)** CIGSSe. The bandgaps (E_g) were intrapolated from the inflection point of d(QE)/dλ (dash line). Note: LJV curve of CIGSSe is certified by Newport, DJV curve is measured in-house after certification (which efficiency drops).

Table 3-1. Device parameters of solar cells extracted from LJV measurement.

Device	S/(S+Se)	E_g [eV]	PCE [%]	FF [%]	V_{OC} [mV]	J_{SC} [mA cm^{-2}]	$V_{OC,def}$ [mV]	R_{SL} [Ω cm^2]	G_{SL} [mS cm^{-2}]	J_0 [A cm^{-2}]	n_L
Z1*	0	1.00	11.6	67.3	423.3	40.6	576.7	0.5	2.4	4.0E-7	1.4
Z2	0.11	1.08	10.5	64.5	424.4	38.5	655.6	0.8	2.6	1.6E-6	1.5
Z3	0.34	1.20	10.4	62.1	495.5	33.8	704.5	1.4	2.7	1.9E-6	1.7
Z4	0.54	1.28	9.8	61.8	531.8	29.8	748.2	1.6	2.2	3.6E-6	2.0
Z5	0.72	1.38	9.1	61.1	577.3	25.8	802.7	1.8	1.9	2.3E-6	2.4
Z6	0.9	1.49	6.0	50.9	557.0	21.3	933.0	2.6	6.7	8.6E-6	3.0
CIGSSe	-	1.16	15.2	75.1	623.1	32.6	547.0	0.4	0.7	3.0E-9	1.5

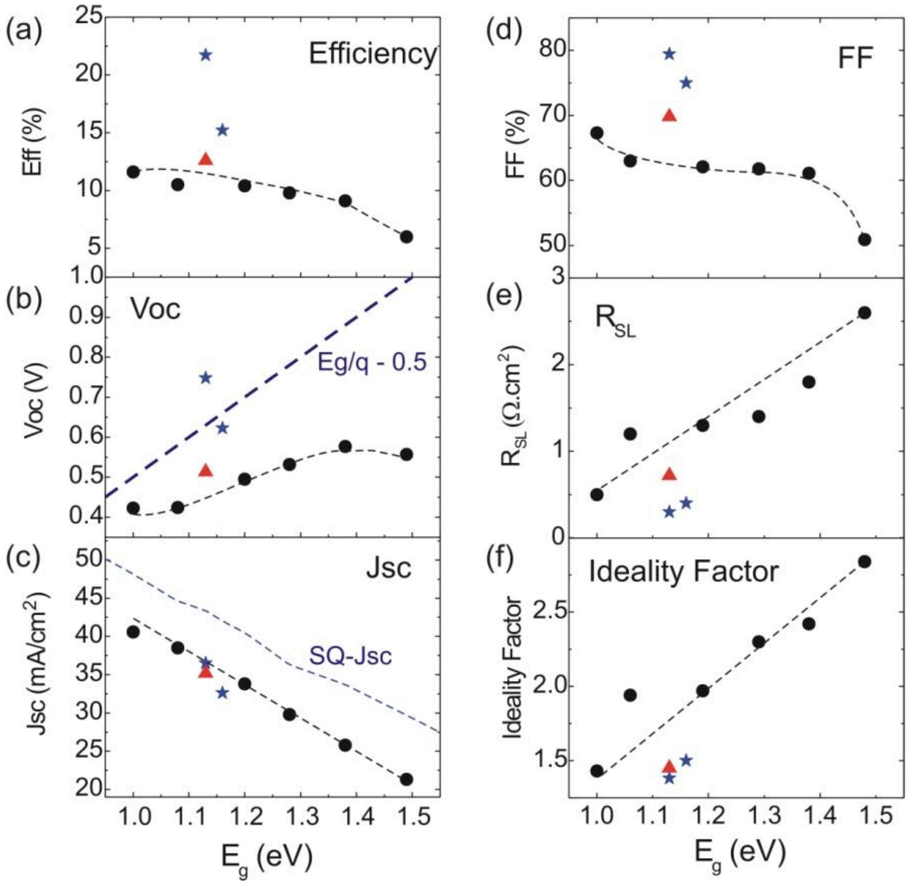

Figure 3-2. Device parameters extracted from LJV, black dots are the CZTSSe devices used in this study, *red triangle* is the record 12.6% CZTSSe solar cell and *blue stars* are the record-CIGSe solar cell (E_g = 1.13 eV) from ZSW and IBM solution processed CIGSSe solar cell (E_g = 1.16 eV).

By increasing the S/(S+Se) ratio in CZTSSe, the E_g increases as lattice constant decreases due to smaller S-atom. V_{OC} should increase as a result of the higher E_g, However, the $V_{OC,def}$ (E_g/q - V_{OC}) widened from 577 mV to 933 mV as E_g increases from 1.00 eV to 1.48 eV (Z1-Z6). The increasing $V_{OC,def}$ issue does not only occur in this study, but it is generally observed for CZTSSe. As mentioned earlier, the record CZTSSe solar cell (PCE: 12.6%, E_g: 1.13 eV) has a *$V_{OC,def}$ of 617 mV* and increases to $V_{OC,def}$ of 789 mV in the record pure-sulphide CZTS solar cell (PCE: 8.4%, E_g: 1.45 eV).[17, 20] Compared to the record- Si, GaAs and CIGS solar cells with $V_{OC,def}$ of less than 400 mV,[75] $V_{OC,def}$ issue underpins the biggest hurdle for CZTSSe technology regardless of processing techniques. Low V_{OC} indicates a high carrier recombination (radiative or non-radiatively) in the bulk of the absorber layer or at the junction interfaces, which increases both the reverse saturation current (J_0) and the diode ideality factor (n_L), as shown in **Table 3-1**. Furthermore, intrinsic defect physics such as electrostatic potential fluctuation induced by non-uniform distribution of charged defects in highly-doped materials could also contribute to $V_{OC,def}$. This will be discussed in detail in **CHAPTER 4**.

Table 3-2. A comparison between the solar cell parameters and the respective SQ-limits with respect to the bandgaps. Notably, the achievable J_{SC} relative to the SQ-J_{SC} decreases (as highlighted) for Z2-Z6 as bandgap increases.

Device	**Eg**	**Eff**	**SQ-Eff**	**V_{OC}**	**SQ-V_{OC}**	**J_{SC}**	**SQ-J_{SC}**	**J_{SC}/ (SQ-J_{SC})**	**FF**	**SQ-FF**
	eV	%	%	V	V	mA/cm^2		%	%	%
Z1	1.00	11.6	31.51	0.423	0.763	40.6	48.2	84.2%	67.3	85.7
Z2	1.08	10.3	32.30	0.492	0.837	38.5	44.6	*86.3%*	63.0	86.6
Z3	1.20	10.4	33.36	0.496	0.940	33.8	40.5	*83.5%*	62.1	87.7
Z4	1.28	9.8	32.94	0.532	1.031	29.8	36.3	*82.1%*	61.8	88.7
Z5	1.38	9.1	33.56	0.577	1.117	25.8	33.7	*76.6%*	61.1	89.3
Z6	1.49	6.0	32.29	0.557	1.209	21.3	29.7	*71.7%*	50.9	90.0
*CZTSSe	1.13	12.6	33.42	0.513	0.883	35.2	43.4	81.1%	69.8	87.2
CIGSSe	1.16	15.2	33.44	0.623	0.911	32.6	42.0	77.6%	75.1	87.5
*CIGSe	1.13	21.7	33.42	0.746	0.883	36.6	43.4	84.3%	79.3	87.2

The second observation with increasing E_g is the reduction in J_{SC}. It is expected that J_{SC} decreases due to reduced absorption of the solar spectrum. However, it was noted that the gap between experimental obtained J_{SC} and theoretical predicted maximum value, $J_{SC,max}$ (or SQ-J_{SC}, assuming 100% collection efficiency) widened as E_g increases (**Figure 3-2(c)**): J_{SC} in Z2 is *86.3%* of the $J_{SC,max}(E_g = 1.08 \text{ eV})$ and further reduced to *71.7%* of the $J_{SC,max}(E_g = 1.49 \text{ eV})$ in Z6 (**Table 3-2**). J_{SC} loss was also observed in the high E_g record-CZTS solar cell, as pointed out in **Section 3.1**. Aside from the optical losses, the reduction of J_{SC} could be associated with the series resistance R_{SL}, which gradually increases from 0.5 Ω.cm^2 to 2.6 Ω.cm^2 as E_g increases from 1.00 to 1.48 eV (**Table 3-1**). In general, R_{SL} could be attributed by two factors: (1) bulk absorber's resistivity and (2) interfacial resistance. By doing resistivity measurement, contribution (1) could be derived quantitatively (**Section 3.3**), whereas the interfacial resistance will be investigated in more detail in **CHAPTER 5** for a comprehensive understanding.

Both the increasing $V_{OC,def}$ and R_{SL} with E_g will result in a decreasing *FF* by the empirical relations given below:[38,76]

$$FF_S = FF_0(1 - 1.1\, r_s) + \frac{r_s^2}{5.4} \tag{3.7a}$$

where, $$FF_0 = [\upsilon_{\mathrm{OC}} - \ln(\upsilon_{\mathrm{OC}} + 0.72)]/(\upsilon_{\mathrm{OC}} + 1) \tag{3.7b}$$

where r_s is the normalized resistance given by $r_s = \mathrm{R_{SL}} \times \mathrm{J_{SC}/V_{OC}}$, and υ_{OC} is the normalized voltage given by $\upsilon_{\mathrm{OC}} = \mathrm{qV_{OC}/nk_BT}$. In the presence of shunt conductance (G_{Sh}), the final FF will be reduced further, given as:

$$FF = FF_S\left(1 - g_{Sh} FF_S \frac{\nu_{OC}+0.7}{\nu_{OC}}\right) \tag{3.7c}$$

where $g_{Sh} = G_{Sh} R_{CH}$ is the normalized shunt conductance, with the characteristic resistance of a solar cell $R_{CH} = V_{OC} / I_{SC}$. G_{Sh} (or G_{SL}) for Z1-Z5 and CIGSSe are all below 3 mS/cm^2, and thus the effect of G_{Sh} on FF can be neglected. In fact, the calculated FF_S (68.5%, 63.2%, 62.4%, 61.6%, 62.1%, 75.9% for Z1-Z5 and CIGSSe, respectively) matches very closely to the experimental FF (**Table 3-1**). *Therefore, the investigations can be narrowed down to just the* $V_{OC,def}$ *and the* J_{SC} *loss in Z1-Z5.*

However, the sudden jump of G_{SL} in Z6 (G_{SL}: 6.7 mS/cm^2) resulted in the deviation of calculated FF_S (57.2%) from the experimental FF (50.9%). Once G_{SL} is factored in the calculated *FF* by Equation (3.7c), the calculated *FF* (50.9%) matches well with the experimental FF in Z6. The high G_{SL} in Z6 could potentially contribute to the large $V_{OC,def}$. The sudden increase of G_{SL} could be due to shunting path resulted from the formation of conducting (low-E_g) secondary phases, which will be discussed in **Section 5.3**. Note that the high G_{SL} problem may not be the general case for high S-content CZTSSe, especially when the equilibrium phases formation could vary with different processing techniques, and high performance CZTS solar cells are usually obtained by vacuum processing technique (e.g. co-evaporation).[17] However, the solution-processed CZTSSe solar cells with high S-content studied here have decent PCE as well. Therefore, it is worthwhile to investigate the effect of secondary phase's formation on the $V_{OC.}$

3.3 Hall Characteristics of Polycrystalline $Cu_2ZnSn(S,Se)_4$ Thin Films

The film resistivity ρ of the CZTSSe absorber was measured using the Van der Pauw method.[77] The Hall measurement was performed using a self-developed rotating parallel dipole line Hall system, as described in **Section 2.1.3** earlier.[60] This system is the key to extract the Hall signal in low mobility or insulating films like our CZTSSe layers. It operates based on lock-in detection of the Hall signal under oscillating magnetic field.

Figure 3-3(a) shows the resistivity (ρ) of CZTSSe (Z2-Z6) and CIGSSe thin films exfoliated from the Mo/soda-lime-glass (SLG) substrate. By multiplying the resistivity with their respective film thickness (t = 2.2, 1.6, 1.7, 1.7, 1.8, 0.9 μm for Z1-Z6 respectively, and 1.9 μm for CIGSSe), the bulk resistance of the absorber layer can be calculated by the relation:

$$R_{S,\,\mathrm{bulk}} = \rho \cdot t \tag{3.8}$$

where ρ is the resistivity and t is the thickness of the thin films. Note that $R_{S,\,\mathrm{bulk}}$ derived here serves as an *upper bound* to the intrinsic resistivity for the thin film absorber layers, because the resistivity values measured from the exfoliated samples represent the *in-plane* resistivity which could suffer more due to grain boundary scattering, compared to the *out-of-plane* resistivity of a thin film where the thickness only spans through 1-2 grains. The $R_{S,\text{ bulk}}$ and $\mathrm{R_{SL}}$ (extracted earlier from the LJV curve) were plotted together in **Figure 3-3(b)**.

In CIGSSe (marked by star), the value of $R_{S,\text{ bulk}}$ is close to the extracted $\mathrm{R_{SL}}$, with the residual resistance ($R_{s,\ res} = \mathrm{R_{SL}} - R_{S,\text{ bulk}}$) of merely 0.27 $\Omega.\mathrm{cm}^2$. In the pure-Se CZTSSe (Z1), $R_{s,res}$ is also small with just 0.35 $\Omega.\mathrm{cm}^2$. However, as $\mathrm{E_g}$ of CZTSSe increases, $R_{s,res}$ widened gradually, which suggests that there exists an additional contribution to the substantial increase of $\mathrm{R_{SL}}$ besides the thin film bulk resistance $R_{S,\text{ bulk}}$. Therefore, interfacial resistance could play an important role in high $\mathrm{E_g}$ CZTSSe, which limits the $\mathrm{J_{SC}}$ and this will be discussed in more details in **CHAPTER 5**.

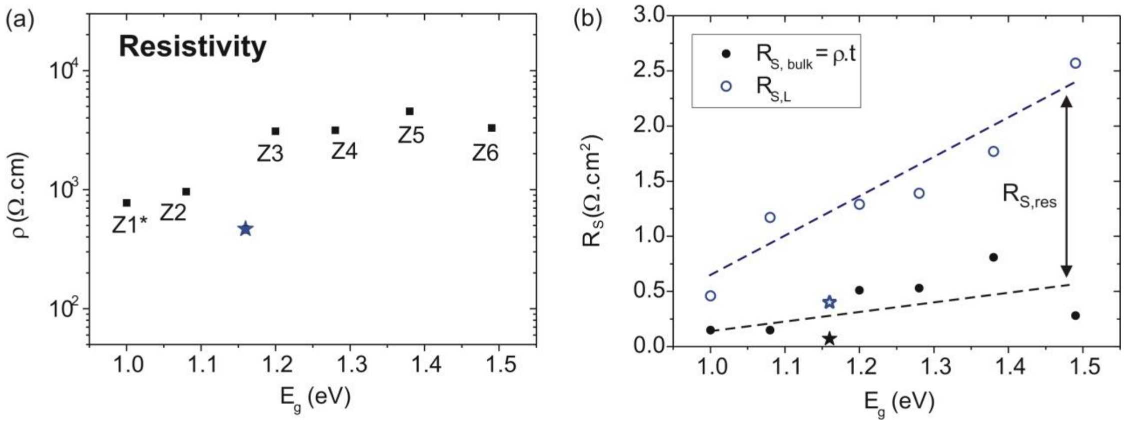

Figure 3-3. (a) Resistivity of CZTSSe (Z2-Z6) and CIGSSe. **(b)** $\mathrm{R_{S,L}}$ (extracted from LJV) re-plotted together with the bulk resistance of the absorber layer ($R_{S,bulk}$), calculated from the product of resistivity and their respective film thickness. The residual series resistance ($R_{S,res}$) is the difference between $\mathrm{R_{S,L}}$ and $R_{S,bulk}$. CIGSSe data is marked by star.

For Hall Effect measurement, **Figure 3-4** shows the post-analysis (self-developed graphical user interface) for the raw data and post-processing signal of CZTSSe (Z3). On the left panel: the top figure shows the oscillation of the magnetic field (B-field) detected by the field sensor (mounted beneath the master magnet) as a function of time. As the sensor was not mounted directly on/near the sample, the units shown in the y-axis were not the actual magnitude of the B-field. The B-field on the sample (located at the centre between the master and mirror magnets) is found from the calibrated B-field with respect to magnets' separation distance, as explained in **Section 0**. The middle-left pane shows the as-recorded Hall oscillation signal as a result from the oscillating B-field. The bottom-most pane shows the processed Hall signal by numerical lock-in and phase-sensitive detection (PSD) techniques. With a certain time constant for the lock-in integration, the out-of-phase Emf contribution (Y, blue line) and the Hall signal (X, red line) will stabilize to a constant value eventually. A positive (negative) X-value indicates the material is a p-type (n-type) semiconductor, and the stabilized X-value is the amplitude of the Hall resistance (R_H).

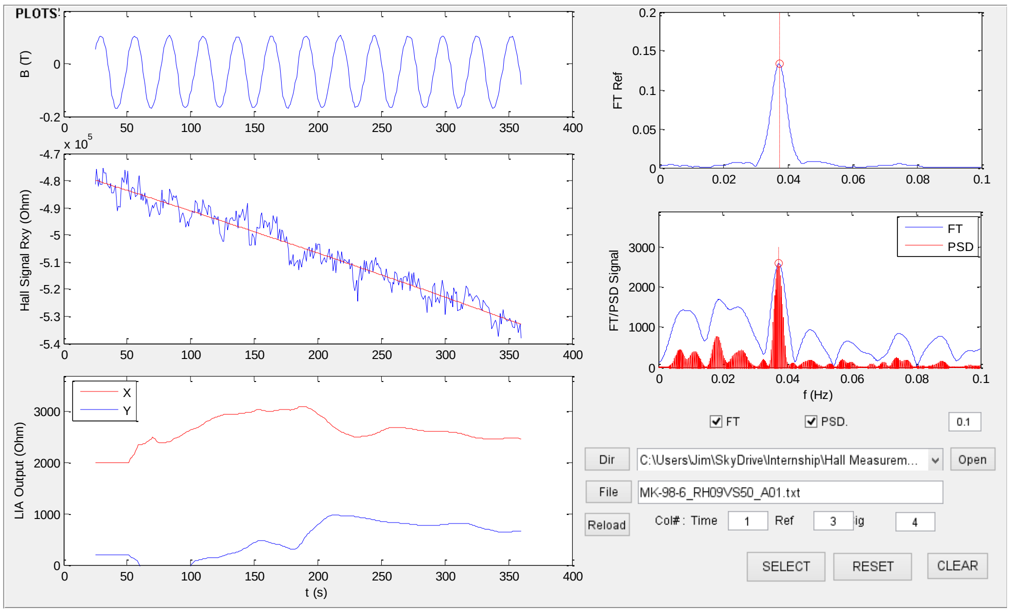

☑ FT ☑ PSD. 0.1

Dir: C:\Users\Jim\SkyDrive\Internship\Hall Measurem...

File: MK-98-6_RH09VS50_A01.txt

Col# : Time 1 Ref 3 ig 4

Figure 3-4. Hall signal post-processing using fast Fourier transform and phase-sensitive detection for CZTSSe-Z3.

On the right-panel: the top-pane shows the Fourier transform (FT) of the B-field and the bottom-pane shows the FT (blue line) of the Hall oscillation in frequency domain. Both the B-field and the Hall-signal oscillating at the same frequency eliminate the ambiguity of the Hall-signal. In addition, the PSD integration (red) which peaks at the same frequency further verified that the Hall-signal is real. To extract meaningful electrical properties for the material, R_H is used for the calculation of majority carrier density (p) and majority carrier mobility (μ_h) given by the relation:

$$p = \frac{B}{q \cdot t \cdot R_H} \tag{3.9a}$$

$$\mu_h = \frac{1}{p \cdot q \cdot \rho} \tag{3.9b}$$

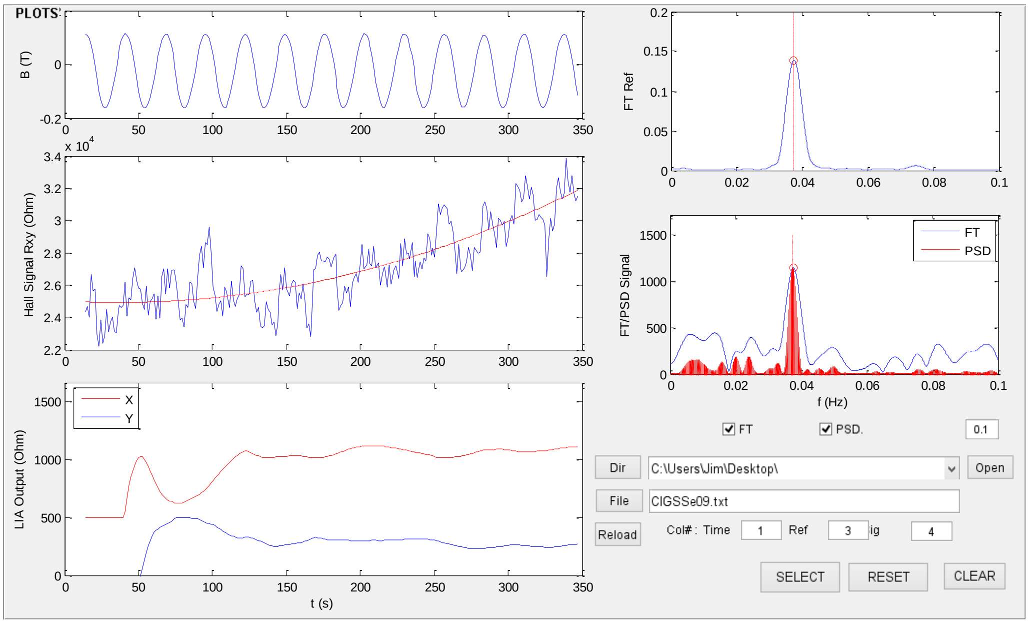

☑ FT ☑ PSD. 0.1

Dir C:\Users\Jim\Desktop\

File CIGSSe09.txt

Col# : Time 1 Ref 3 ig 4

Figure 3-5. Hall signal post-processing using fast Fourier transform and phase-sensitive detection for CIGSSe.

Figure 3-5 shows a similar Hall measurement raw data and post-processed signal for the CIGSSe thin film, with a clearer Hall oscillation observed due to its higher hole mobility. The Hall signal was further verified by the FT and PSD integrated peak at the same oscillation frequency as the B-field. The derived p and μ_h

for CZTSSe (Z1-Z6) and CIGSSe were summarized in **Figure** 3-6. The carrier density in CIGSSe is 3.52×10^{15} cm^{-3}, whereas the carrier density in CZTSSe ranges from 1.73×10^{16} cm^{-3} (Z1) to 1.40×10^{15} cm^{-3} (Z6). A decreasing trend in carrier density with E_g was observed in CZTSSe. Nevertheless, the carrier concentration for CZTSSe and CIGSSe obtained here are in line with typical solar cell material which has a carrier concentration between 10^{15}- 10^{16} cm^{-3}. The origin of the hole carriers has been discussed in **SECTION 1.2.4**. Noted that these are the *net* carrier density which do not provide much information on the defect density and compensation ratio. The defect physics of the material will be studied in more detail in **CHAPTER 4**.

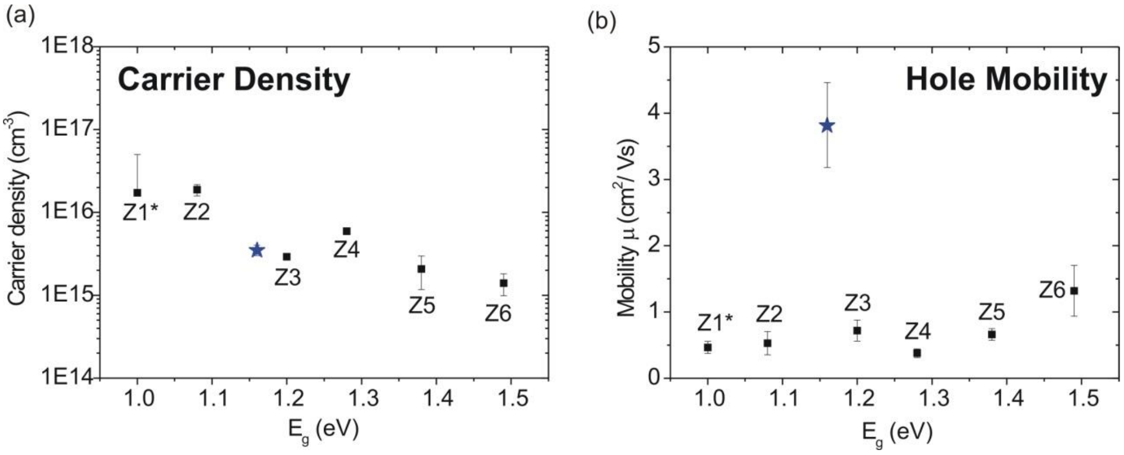

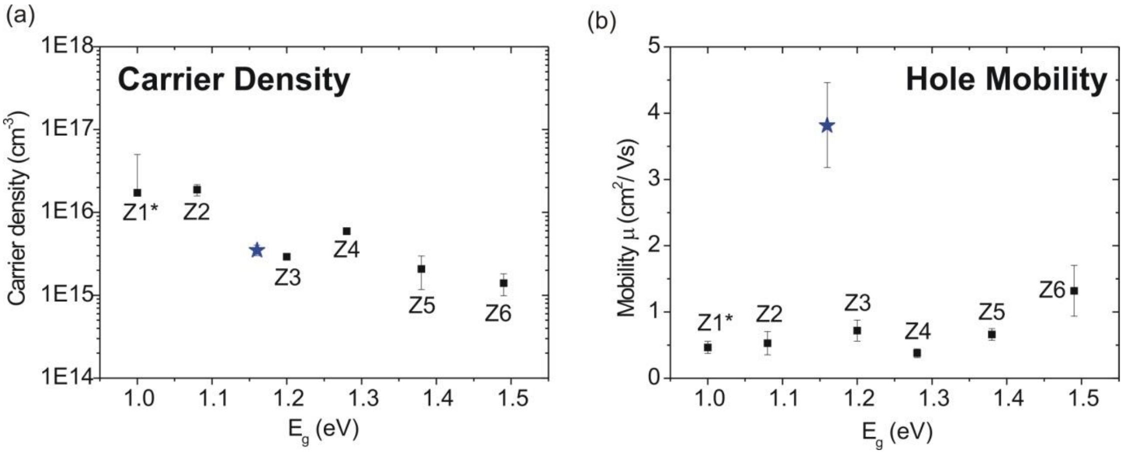

Figure 3-6. Carrier densities and hole mobilities of CZTSSe (Z1-Z6) and CIGSSe (marked by star) thin films measured by Rotating PDL Hall system.

Table 3-3. Resistivity (ρ), hole carrier density (*p*) and hole mobility (μ_p) extracted from Hall measurement. Bulk series resistance of absorber layers ($R_{S,CZTSSe}$) are calculated by ρ×t. The metal ratio for the thin films are included as well.

Films	t [µm]	Cu/(Zn+Sn)	Zn/Sn	ρ [Ω.cm]	p [cm^{-3}]	μ_p [cm^2 V^{-1} s^{-1}]	$Rs_{,CZTSSe}$ [Ω.cm^2]
Z1'	1.88	0.850	0.982	7.74×10^2	1.73×10^{16}	0.46	0.15
Z2'	1.61	0.915	1.010	9.63×10^2	2.74×10^{16}	0.53	0.15
Z3'	1.66	0.913	1.010	3.09×10^3	2.92×10^{15}	0.72	0.51
Z4'	1.70	0.921	1.010	3.15×10^3	5.93×10^{15}	0.38	0.53
Z5'	1.78	0.964	0.950	4.55×10^3	2.08×10^{15}	0.66	0.81
Z6'	0.85	0.870	1.090	3.30×10^3	1.43×10^{15}	1.32	0.28

For hole mobility, μ_h in CIGSSe was found to be 3.82 cm^2/V.s, higher than the μ_h of CZTSSe (Z1-Z6) ranging from 0.38- 1.32 cm^2/V.s. Low carrier mobility is generally observed in CZTSSe, including the high performance (PCE ~ 9 - 12%) CZTSSe solar cell with reported average μ_h ~ (0.6 ± 0.3) cm^2/V.s.[66] Low carrier mobility suggests that the photo-generated hole carriers are prone to a higher recombination probability before transporting to the electrode for efficient charge collection. The recombination loss due to low carrier mobility will contribute to the higher $V_{OC,def}$ generally observed in CZTSSe solar cell. However, unlike carrier density, the hole mobility does not depend on E_g of CZTSSe. Therefore, further characterizations are required to explain the increasing $V_{OC,\ def}$ with E_g (CHAPTER 4).

3.4 Conclusion

In conclusion, from the LJV measurement and extraction of device parameters on the full E_g range CZTSSe, a general understanding on the electrical limitation for the solar cell was obtained, as summarized in **Figure 3-2**. V_{OC} deficit is the number one problem in CZTSSe technology, and $V_{OC,def}$ becomes more severe with increasing E_g

or higher S/(S+Se) ratio. Secondly, J_{SC} loss due to increased R_{SL} becomes significant in high E_g CZTSSe. Furthermore, high G_{SL} was also found in Z6 with highest S/(S+Se) ratio. Having known the general electrical limitations, the factors affecting these electrical parameters were investigated in more details by resistivity and Hall measurement.

Resistivity and Hall measurement were carried out to find out the resistivity, (net) majority carrier density, and hole mobility of CIGSSe and CZTSSe (Z1-Z6) absorber layers. From the resistivity measurement, the series resistance contributed by the bulk absorber layer ($R_{S,bulk}$) can be derived. $R_{S,bulk}$ was found to be similar to R_{SL} (extracted from LJV) in CIGSSe and Z1, but the difference between the two ($R_{S,res} = R_{SL} - R_{S,bulk}$) gradually increases with E_g in CZTSSe, imposing further probe into the interfacial resistance contributing to the increasing R_{SL} and J_{SC} loss in the high E_g CZTSSe. From the Hall Effect measurement, carrier density of 10^{15}-10^{16} cm^{-3} were derived for CIGSSe and CZTSSe (Z1-Z6), in line with the typical carrier density for solar materials. However, the defect density and defect physics need further investigation. Last but not least, the hole mobility for CZTSSe were generally lower than CIGSSe, which indicates high possibility of recombination losses that contribute to $V_{OC,def}$. However, μ_h independent with E_g renders no explanation for the increasing $V_{OC,def}$ observed. Therefore, further characterizations from the aspects of bulk and interfacial losses are investigated in the following chapters for a comprehensive understanding.

CHAPTER 4 Photoluminescence of Thin Film Polycrystalline $Cu_2ZnSn(S,Se)_4$

4.1 Introduction

Under open-circuit condition, photo-generated electron-hole pair in a solar cell will eventually recombine to return to their equilibrium state, either by radiative or non-radiative recombination. If radiative transition is the only path for carrier recombination, the solar cell will have high V_{OC} and PCE.[78] This is because detrimental defects are not contributing to the solar cell output, such as deep non-radiative defects and Auger quenching are of minimal. For radiative recombination in semiconductors, several transitions have been observed including band-to-band transition (BB, free-electron and free-hole in the conduction band and valence band, respectively), free-to-bound (FB, free-electron and bound-hole at defect), donor-acceptor pair (DAP, both carriers bound to defects), excitons and bound excitons transitions.[79] In high-quality semiconductor such as epitaxial growth GaAs, BB transition with a sharp photoluminescence (PL) peak is usually observed.

The above radiative transitions are associated to lightly-doped material with low doping level or low defect density, such that the point defects are distributed randomly in the material without interacting with other defects. In such cases, the conduction band minimum (CBM), valence band maximum (VBM) and the defect energy level within the bandgap (E_g) is discrete and well-defined. Therefore, the defect-related peak and BB transition could be clearly resolved in the PL spectrum. On the other hand, highly doped semiconductor has high defect density such that interaction between defects occurs and the defect levels suffer a broadening. A material is considered highly doped if the average distance between impurities is shorter than the impurity Bohr radius. A semiconductor is considered as n-type (p-type) heavily doped when the heavy doping condition is met, *i.e.* the product of the donor (acceptor) concentration N_d (N_a) and the impurity Bohr radius is much larger than unity, $N_d a_e^3 \gg 1$ ($N_a a_h^3 \gg 1$).

As most of the defects are charged, band-tails caused by electrostatic potential fluctuations are induced by a random distribution of unscreened charged defects.[80] These charged defects may be donors, acceptors, or both in the case of highly compensated semiconductors. The spatially-varying charge density leads to a local perturbation of the band structure which results in a fluctuating conduction and valence band.[81] The exponentially decaying density of state for the band tails with energy smaller than E_g results in a broad asymmetric photoluminescence (PL) spectrum at room temperature.[80, 82] The average depth of the electrostatic potential fluctuation (γ) of the bands can be estimated by:[80, 83]

$$\gamma(R) = \frac{e^2}{4\pi\varepsilon_r\varepsilon_0}\frac{(N_t R^3)^{1/2}}{R} \tag{4.1}$$

where ε_0 is the permittivity of vacuum, ε_r is the relative permittivity (or dielectric constant), N_t is the total defect density with mean square fluctuation on the order of $(N_t R^3)^{1/2}$ within a volume R^3. N_t includes all radiative and non-radiative charged defects with energy states inside of E_g. Note that the depth of the fluctuating potential is proportional to N_t, which plays a crucial role in the intrinsic bulk properties of a semiconductor.

It is noted that the two prevalent models for understanding the sub-bandgap defect structures of CIGSSe and CZTSSe, *i.e.* the QDAP (quasi donor/acceptor pair) and the electrostatic potential fluctuation models are inherently inter-related. In the electrostatic potential fluctuation model, the average depth γ of the fluctuating bands of the semiconductor is estimated by Equation (4.1), whereas the QDAP model describes the distribution of radiative donors and acceptor states (part of N_t) that contribute to this potential fluctuation. The QDAP model can be used to estimate the average separation between donor and acceptor and its density based on the Coulombic interaction between the charged donor and acceptor, as reflected in the recombination photon energy of:[8, 9]

$$E = E_g - E_D - E_A + \frac{e^2}{4\pi\varepsilon_0\varepsilon_r s} \tag{4.2}$$

where E_D and E_A are the donor and acceptor energy level separated from the CBM and VBM respectively, and s is the separation distance between donor and acceptor. Due to the interaction and clustering of charged defects, the "quasi" term is used to distinguish QDAP from the conventional donor-acceptor-pair (DAP) recombination with no interaction between defects, though Equation (4.2) is also used to describe the photon energy of DAP recombination.

This chapter investigate the contribution of bulk intrinsic losses in the CZTSSe absorbers' to the $V_{OC,def}$ problem by photoluminescence study. The power-dependent, temperature-dependent PL, and the carrier lifetime of $Cu(In,Ga)(S,Se)_2$ (CIGSSe), CZTSSe with low (Z2) and high (Z6) S/(S+Se) ratio were measured. All the three samples were prepared using hydrazine pure-solution approach to allow a fair comparison. A new method was introduced to assess γ qualitatively by examining the carrier lifetime as a function of photon energy ($d\tau/dE$). Furthermore, the upper bound of N_t can be estimated from the power-dependent PL spectra, which can be used to calculate γ. Both methods show that γ(CIGSSe) < γ(CZTSSe1) < γ(CZTSSe2). Furthermore, the “activation energy” (E_a) is derived from the Arrhenius relation of the PL intensity vs. temperature, where E_a is defined as the energy required to de-trap carriers from the localized states they occupy at 7K and redistribute them into other states; the value of E_a depends on two factors: (i) the energetic depth of the state with respect to E_g and (ii) the availability of other states, including the band edge as well as the non-radiative states. Thermal re-distribution of carriers from radiative to non-radiative defect states would result in the observation of a higher value of E_a.[84] It was observed that E_a(CIGSSe) < E_a(CZTSSe1) < E_a(CZTSSe2), indicating a higher density of non-radiative defects and (or) a deeper defect level in CZTSSe compared to CIGSSe. By examining the temperature-dependence of the defect peak, it can be shown that the shallow E_a in CIGSSe allows carriers thermalization into the band tail at high temperatures, but this does not occur for CZTSSe and the thermalized carriers are effectively quenched by non-radiative channels. The values of γ and E_a have a direct impact on the V_{OC} of the solar cells.

4.2 Defect Physics of Polycrystalline $Cu_2ZnSn(S,Se)_4$

4.2.1 QDAP Defect Density

Figure 4-1 shows the PL spectra on hydrazine solution-processed CIGSSe, CZTSSe with low (Z2) and high (Z6) S/(S+Se) ratio, recorded as a function of incident laser fluence at 7K. At low laser fluence, the dominant recombination involves sub-bandgap states, as indicated by the main PL peaks for the samples (~1.08, ~0.95, ~1.20 eV for CIGSSe, Z2 and Z6, respectively) which are significantly below E_g. From the power law relationship $I \sim P^m$, where I is the PL intensity proportionate to the laser power P with the exponent m, the recombination mechanism can be assessed. When $m > 1$, the recombination is associated to excitonic BB transition, whereas $m < 1$ indicates defect-related recombination.[85] As seen in **Figure 4-1**, the intensity of the low energy PL peak saturates at high laser fluence due to the finite number of defect states available.

The saturation of peak height indicates that $m < 1$, and thus the main PL peaks can be assigned to QDAP emission similar to Ref.[86]

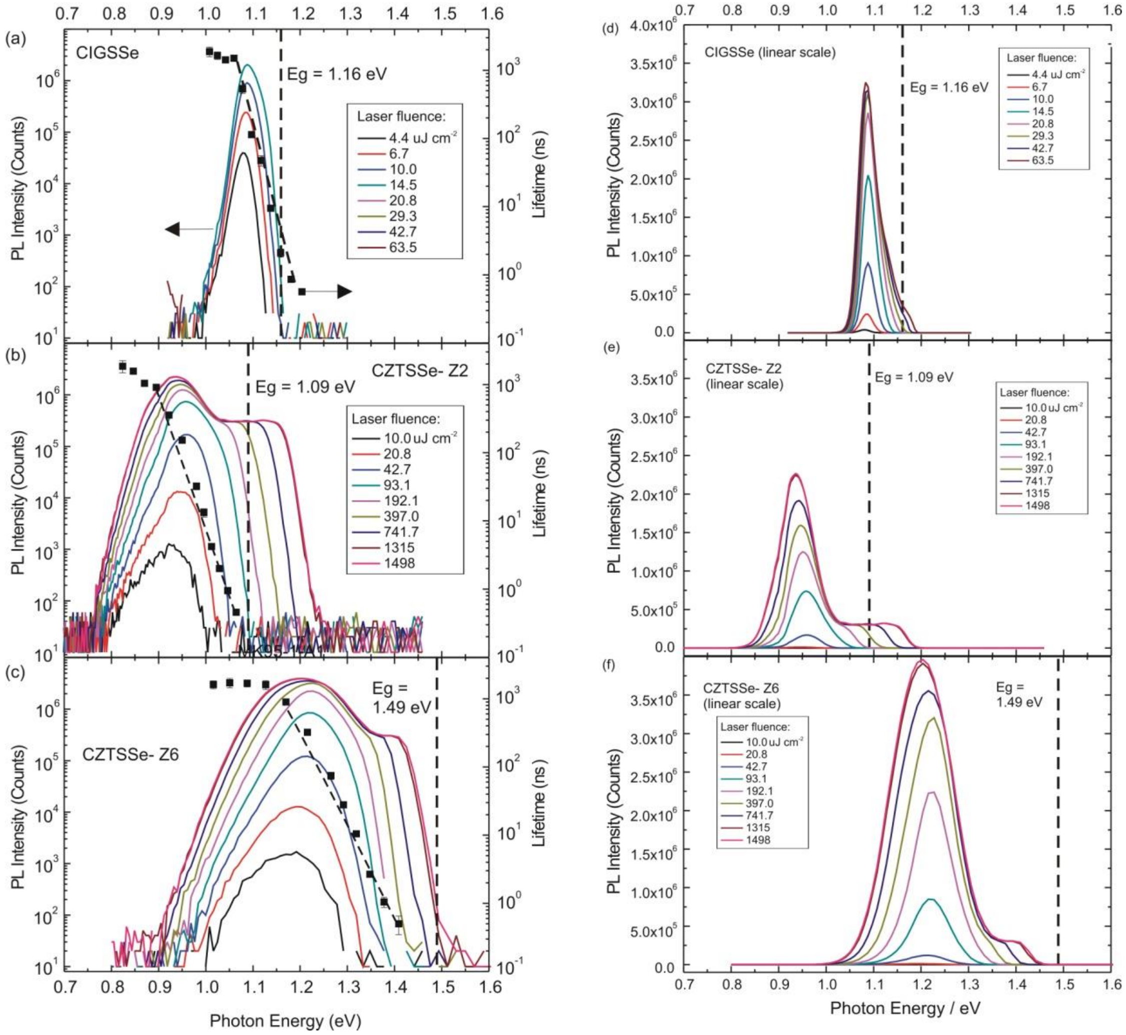

Figure 4-1. Power-dependent PL (left axis) recorded at 7K for (a) CIGSSe, (b) CZTSSe with low S/(S+Se) ratio (Z2) and (c) CZTSSe with high S/(S+Se) ratio (Z6). The vertical dashed line corresponds to the band gap (E_g) of each sample. The laser fluence for Z6 is the same as Z2. The fitted recombination lifetimes at different photon energies are marked by the black square symbols (right axis). Right panels show the PL spectra in linear scale.

The conventional DAP transition in non-interacting point defects can be found in textbook.[79] The transition processes are as follow: photo-excited carriers are trapped at the charged donor (D^+) and acceptor (A^-) sites to produce neutral donor (D^0) and acceptor (A^0) centers. In returning to equilibrium, electrons at D^0 will recombine radiatively with holes at A^0. This process is known as DAP transition which can be described by the reaction:[79]

$$D^0 + A^0 \longrightarrow \hbar\omega + D^+ + A^- \tag{4.3}$$

The emitted photon energy ($\hbar\omega$) is increased by the amount of $e^2/4\pi\varepsilon_0\varepsilon_r s$ as stated in the last term of Equation (4.2) because the energy of the final state in reaction (4.3) is lowered by the Coulombic attraction between the charged D^+ and A^-.[79] The same Equation (4.2) is also used to estimate the QDAP density in previous reports by making two assumptions:[86] (i) Coulombic attraction between D^+ and A^- is negligible at low laser fluence, *i.e.* the distance between the charged D^+ and A^- is too far apart to interact; (ii) the saturation of the blue-shift magnitude for the QDAP peak indicates that all QDAP states are occupied, *i.e.* maximum Coulombic attraction. Therefore, the average separation distance s between donor and acceptor can be estimated by equating the last term in Equation (4.2), $e^2/4\pi\varepsilon_0\varepsilon_r s$, to the magnitude of the saturated blue-shift. In addition, the QDAP density can be estimated by assuming an uniform distribution of defects within a spherical volume, *i.e.* $r = (4\pi N_D/3)^{-1/3}$.[86]

The peak positions of the PL spectra in **Figure 4-1** were fitted using asymmetric double sigmoidal function (available in *OriginPro8*):

$$y = y_0 + A \cdot \frac{1}{1 + \exp(-\frac{x - x_c + w_1/2}{w_2})} \cdot \left[1 - \frac{1}{1 + \exp\left(-\frac{x - x_c - w_1/2}{w_3}\right)}\right] \tag{4.4}$$

where y_0 is the maximum amplitude, w_1 is the FWHM of the peak, w_2 is the variance of low-energy side, and w_3 is the variance of high-energy side. The magnitude of the saturated blue-shift was derived, by subtracting $x_c(P1)$ of the saturated blue-shifted peak by $x_c(P2)$ at lowest possible laser excitation. Thus, the saturated blue-shift magnitude of the QDAP peak positions can be derived and used to estimate the QDAP density, with QDAP density: CIGSSe < CZTSSe1 < CZTSSe2 as shown in **Table 4-1**.

The significant difference in magnitude between QDAP density and the photo-generated electron-hole pair ($N_{\text{é-h}}$) by the laser fluence could be due to the assumption of fully absorbed laser excitation by the materials and a high non-radiative recombination rate such that generated electron-hole pair do not necessarily result in radiative emitted photon. However, $N_{\text{é-h}}$ > QDAP density indicates a reasonable estimate of the defect densities.

Table 4-1. QDAP density extracted from the saturated blue-shift magnitude of the QDAP peak.

Device (ε_r)	**Peak position**			**QDAP density** (cm^{-3})	**Laser fluence for P2** ($\mu J\ cm^{-2}$)	**$N_{\text{è-h}}$** (cm^{-3})
	P1 (eV)	P2 (eV)	*s* (nm)			
CIGSSe (12.0)[10]	1.080	1.088	15.52	6.38×10^{16}	14.5	2.7×10^{18}
	(±6.2E-5)	(±4.5E-5)	(±0.97)	($\pm 1.19 \times 10^{16}$)		
CZTSSe1 (8.1)[11]	0.940	0.960	8.84	3.46×10^{17}	93.3	2.5×10^{19}
	(±0.005)	(±1.7E-4)	(±2.32)	($\pm 2.73 \times 10^{17}$)		
CZTSSe2 (6.7)[11]	1.175	1.224	4.35	2.89×10^{18}	192.5	5.2×10^{19}
	(±8.0E-4)	(±4.6E-4)	(±0.28)	($\pm 5.58 \times 10^{17}$)		

Assuming the deep defect states do not contribute to the conducting holes or electrons, QDAP density can be considered as the sum of acceptor density (N_a) and donor density (N_d), *i.e.* $N_a + N_d$, whereas the Hall carrier density is the net charge carrier density, *i.e.* $N_a - N_d$ (for *p*-type semiconductor). Therefore, by combining both the QDAP and Hall carrier density, the respective N_a and N_d can be estimated by solving the algebraic equations. The Hall carrier density of the respective thin films can be found in Section 3.3. Therefore, N_a and N_d of CIGSSe, Z2 and Z6 can be derived, as tabulated in **Table 4-2**. The respective compensation ratio (κ) can also be estimated accordingly (N_d/N_a).

Table 4-2. Acceptor density (N_a) and donor density (N_d) estimated from QDAP density and Hall carrier density.

	CIGSSe	**CZTSSe- Z2**	**CZTSSe- Z6**
QDAP Density ($N_a + N_d$, cm^{-3})	$6.38{\times}10^{16}$ ($\pm1.19 \times 10^{16}$)	$3.46{\times}10^{17}$ ($\pm2.73 \times 10^{17}$)	$2.89{\times}10^{18}$ ($\pm5.58 \times 10^{17}$)
Hall Carrier Density ($N_a - N_d$, cm^{-3})	$3.52{\times}10^{15}$ ($\pm5.25 \times 10^{14}$)	$2.74{\times}10^{16}$ ($\pm2.92 \times 10^{15}$)	$1.43{\times}10^{15}$ ($\pm4.14 \times 10^{14}$)
$\mathbf{N_a}$ (cm^{-3})	$3.37{\times}10^{16}$ ($\pm5.96 \times 10^{15}$)	$1.87{\times}10^{17}$ ($\pm1.37 \times 10^{17}$)	$1.45{\times}10^{18}$ ($\pm2.79 \times 10^{17}$)
$\mathbf{N_d}$ (cm^{-3})	$3.01{\times}10^{16}$ ($\pm5.96 \times 10^{15}$)	$1.59{\times}10^{17}$ ($\pm1.37 \times 10^{17}$)	$1.44{\times}10^{18}$ ($\pm2.79 \times 10^{17}$)
Compensation Ratio, κ (N_d/N_a)	89.5%	85.3%	99.9%

The defect density in CZTSSe is higher than that of CIGSSe, and Z6 with higher S/(S+Se) ratio has higher defect density and κ than Z2. As defect density increases and net charge carriers (or free carriers) density reduces, the depth of the fluctuating potential (γ) will increase due to increased perturbation by charged defects and reduced screening by free carriers, with the maximum screening length r_s (or radius) given by the relation:[83]

$$r_s = \frac{N_t^{1/3}}{p^{2/3}} \tag{4.5}$$

and thus, γ is reduced to:[83]

$$\gamma(r_s) = \frac{e^2}{4\pi\varepsilon_r\varepsilon_0}\frac{N_t^{2/3}}{p^{1/3}} \tag{4.6}$$

where N_t is the total charged defect density and p is the free carrier density.

Note that the QDAP density extracted here are derived from radiative PL emission, which may not truly reflect the total defect density (N_t), considering that there may be deep defects and non-radiative defects. N_t could be estimated from the power-dependent PL spectra described below.

4.2.2 Total Defect Density

In **Figure 4-1**, as the laser fluence increases beyond a *threshold* above which all charged defects (N_t, including non-radiative defects) within E_g become occupied, a distinct "shoulder" emission appears at higher photon energy. The shoulder emission involves band- or band-tail related recombination as reflected by the short recombination lifetime (< 10 ns) as carriers become more delocalized. This will be discussed in more detail in **Section 4.2.4** later. Therefore, by calculating the electron-hole pair generated ($N_{é\text{-}h}$) at the threshold laser fluence at which the shoulder emission appears, N_t can be roughly estimated.

The threshold laser fluence occurs at 29.3, 192.1, 397.0 μJ cm^{-2} for CIGSSe, Z2 and Z6 respectively. A conservative assumption was made- the incident light is fully absorbed by all the three films within the first 100 nm (absorption coefficient of 10^5 cm^{-1} at 532 nm),[87, 88] and thus the corresponding electron-hole pairs generated ($N_{é\text{-}h}$) in the absorbers represent the upper bound values. As a result, the *upper bound* of N_t ($2 \times N_{é\text{-}h}$) are calculated to be 0.16, 1.0, and 2.2 × 10^{20} cm^{-3} for CIGSSe, Z2 and Z6, respectively.

4.2.3 Potential Fluctuation

By substituting the tunnelling length $R = \hbar/\sqrt{m_r\gamma}$ into Equation (4.1),[83] γ can be estimated using the following equation:[83]

$$\gamma^5 = (\frac{e^2}{4\pi\varepsilon_0\varepsilon_r})^4 \frac{N_t^2\hbar^2}{m_r m_0} \qquad (4.7)$$

where m_r is the reduced effective mass given by $m_r = (m_e m_h)/(m_e + m_h)$, m_e is the electron effective mass, m_h is the hole effective mass, m_0 is the electron mass, and $\hbar$ is the reduced Planck's constant. The calculated and experimental values for dielectric constants and effective masses of CIGSSe and CZTSSe can be found in Ref.[10, 11, 87] Therefore, the *upper bound* of γ can be extracted using the estimated (upper bound of) N_t, as summarized in **Table 4-3**.

Table 4-3. A summary of parameters extracted from CIGSSe, Z2, and Z6. *ε_r for Z2 is obtained from bandgap interpolation from Ref.[11] and [87].

	CIGSSe	**CZTSSe1**	**CZTSSe2**
$\mathbf{E_g}$ (eV)	1.16	1.09	1.49
$\boldsymbol{m_e^*}$ (m_0) (Ref.[87, 89])	0.09	0.07	0.18
$\boldsymbol{m_h^*}$ (m_0) (Ref.[26, 29])	0.25	0.09 - 0.33	0.22 - 0.71
$\boldsymbol{\varepsilon_r}$ (Ref.[10, 11, 87])	12.0	8.1*	6.7
Threshold laser fluence (µJ cm^{-2})	29.3	192.1	397.0
$\mathbf{N_{\acute{e}\text{-}h}}$ (cm^{-3})	7.9×10^{18}	5.1×10^{19}	1.1×10^{20}
Upper bound of $\mathbf{N_t}$ (cm^{-3})	1.6×10^{19}	1.0×10^{20}	2.2×10^{20}
Upper bound of $\boldsymbol{\gamma}$ (meV)	36.1	107-115	141-144

Band gap fluctuation was not expected to exist in these three materials as proven by the drastic increase in recombination lifetimes of the main PL peak probed at low temperature (more than three orders of magnitude) compared to the recombination lifetimes probed at room temperature (**Figure 4-2** below), indicating that spatial tunnelling (*i.e.* through highly localized states) is required for electron-hole recombination.[31] In the case of band gap fluctuation, E_g is fluctuating spatially where the trough states of the local conduction band has the same k-vector with the peak state of the local valence band,[31] and thus carrier tunnelling is not mandatory for recombination. Therefore, the large density of charged defects is expected to contribute to the spatial potential fluctuations γ of the bands.

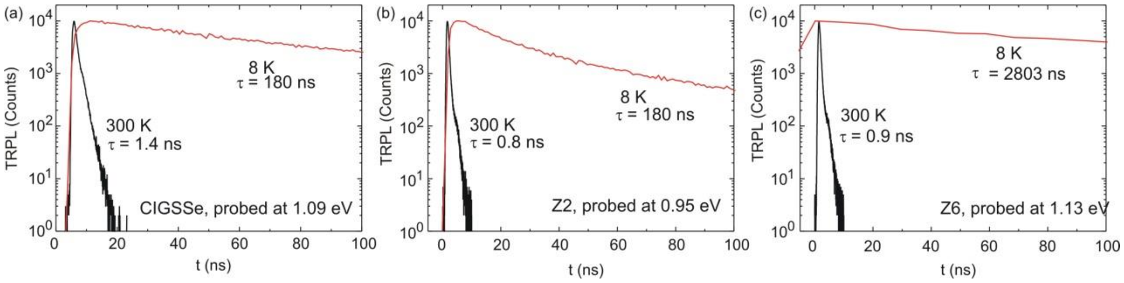

Figure 4-2. Recombination lifetime probed at the sub-E_g main PL peak of (a) CIGSSe, (b) Z2 and (c) Z6.

4.2.4 Degree of Carrier Localization

In equilibrium, laser generated electron-hole pairs first fill up the defect and band-tail states with lower energy before filling up the high energy band-tail or band states. Carriers trapped in defects and low energy band-tail states are localized, which tunneling probability is low for recombination with their electron or hole counterpart, resulting in a long recombination lifetime. On the other hand, carrier in the high energy band-tail and band states are more delocalized and results in a short recombination lifetime. Therefore, by freezing the carriers at low temperature to their lowest possible energy states and probing the recombination lifetime at various photon energies, the degree of carrier localization, and thus their respective electronic structures in these three materials can be gauged, as depicted in **Figure 4-3** below.

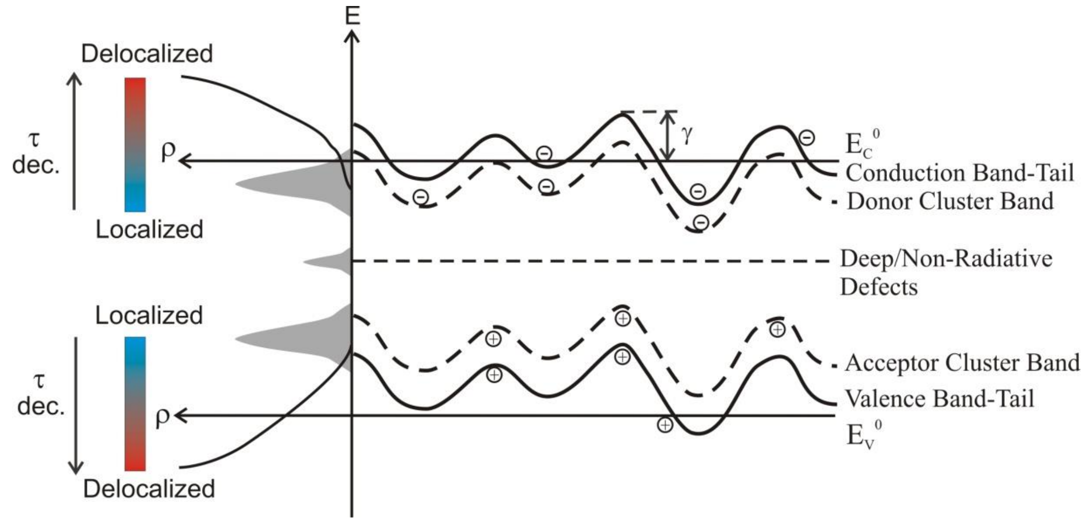

Figure 4-3. Schematics of electrostatic potential fluctuation induced by the non-uniform distribution of charged defects (high local distribution of charged defects results in stronger perturbation and deeper band-tail states). With deeper γ, the density of states of the band tail states span a wider energy range, which is reflected in a slower change of recombination lifetime with respect to photon energy (the slope dτ/dE is smaller).

Time-resolved photoluminescence (TRPL) decay probed at each photon energy is fitted by quadratic recombination model:[90]

$$I(t) = \frac{I_0 \exp(-t/\tau)}{1 + (C/A)n_0[1 - \exp(-t/\tau)]} \tag{4.8}$$

where $I(t)$ is the PL intensity at time t, I_0 is the PL intensity at time zero, A and C are the coefficients for linear and quadratic recombination processes, and τ is the recombination lifetime. The fitted τ at various photon energies were plotted on a logarithmic scale (right axis) in **Figure 4-1** and re-plotted in **Figure 4-4**. For all the CIGSSe, Z2 and Z6 samples, two slopes in lifetime vs. photon energy data (dτ/dE) in exponential scale were observed. The first slope corresponds to photon energies below the QDAP peak energy; within this regime, τ is almost constant in the order of ~1 μs. This indicates that the QDAP recombination is primarily limited by the tunneling probability between spatially separated charged donor and acceptor, and the long τ signifies a low probability of tunneling. Note that the tunneling probability does not solely depend on the separation distance between the charged donor and acceptor, other factors such as the barrier height (γ), barrier width (*R*), carriers' energy and their effective masses could contribute as well, given by the relation:[80]

$$\text{Tunneling probability} = \exp\left[-\frac{R\sqrt{m^* \,\Delta}}{\hbar}\right] \tag{4.9}$$

where $\Delta = E_h - E_e$, where E_e is the energy from the electron Fermi level (which depends γ, larger E_e indicates less energetic electron) and E_h is the energy from the hole Fermi level. This is similar to the carrier tunnelling probability of quantum well.[91] Therefore, a lower τ for the QDAP recombination in Z6 was not observed although the QDAP separation distance is shorter (**Table 4-1**), given the larger carriers' effective mass, γ and *R*.

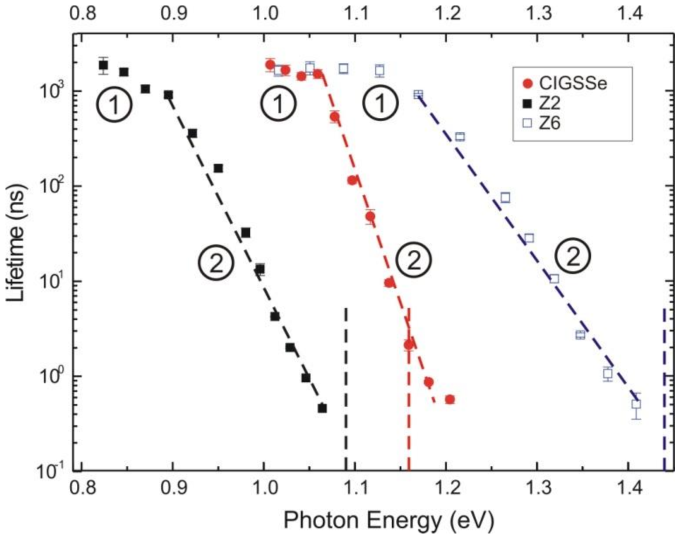

Figure 4-4. Recombination lifetime probed at various photon energy at low temperature (7K) for CIGSSe, CZTSSe-Z2 and Z6. Two slopes of dτ/dE in exponential scale are marked with "1" and "2".

The second slope observed in dτ/dE relationship occurs at photon energies larger than the QDAP peak energy. In this regime, τ decreases rapidly with increasing energy, ranging from 1 μs to 10 ns. The fast-changing τ with energy is due to the increasingly delocalized carriers at higher energy states of the overlapping defect band and the band-tail, resulting in a faster recombination. Note that there may be an energetic overlap among the defect band, the band-tail and the band states (as depicted in **Figure 4-3**). Thus, the band- and band-tail related recombinations are indistinguishable as they were intermixed in the PL spectrum and the lifetime shows a mono-exponential decay with respect to photon energy. At photon energies in the shoulder emission region, the recombination lifetimes decrease down to < 10 ns for all the three samples. Recombination with such short lifetime involves high-energy band-tail or band-related transitions (*i.e.* band-to-impurity (BI), band-to-tail (BT), band-to-band (BB), tail-to-impurity (TI), tail-to-tail (TT)), where the shorter lifetimes represent transition from more delocalized states. As the band- and band-tail related recombinations were indistinguishable, a model is proposed here wherein each PL spectrum contains contributions from multiple recombination mechanisms: with increasing photon energy, the transition of recombination mechanisms is of the order: [$d\tau/dE$ slope 1] QDAP (impurity-to-impurity, II) → [$d\tau/dE$ slope 2] TI → TT → BI → BT → BB, *i.e.* increasing degrees of carrier delocalization. Furthermore, a hypothesis can be made such that the sharp decrease of τ with energy (the second slope) occurs when band- and band-tail related recombination are involved, *i.e.* TI, TT, BI, BT, BB.

Fast recombination which involves highly delocalized carriers with recombination lifetimes of ~0.5 ns and photon energy > E_g have been reported in GaAs as band-to-band (BB) transition.[92] BB recombination with such short lifetime was also observed in CIGSSe and Z2, as shown by the shoulder emission which extended beyond the room-temperature E_g (**Figure 4-1(a) and (b)**). However, BB transition with photon energy > E_g was not observed in Z6 for the same conditions of carrier injection (**Figure 4-1**(**c)**). This is due to the severe band tail, or large γ, and/or higher concentration of non-radiative defect states, which require a higher density of photo-generated carriers to fill up all these sub-E_g states. Although the recombination of Z6 involves more localized states, a short τ (~ 0.5 ns) was still observed at high photon energy, which is due to the high non-radiative recombination rate (explained later in **Section 4.2.5**) which reduces the overall recombination lifetime by the relation:[80, 93]

$$\frac{1}{\tau} = \frac{1}{\tau_{radiative}} + \frac{1}{\tau_{non-radiative}} \tag{4.10}$$

BB transition with photon energy > E_g should be observed in Z6 if a higher laser fluence (> 1.5 mJ/cm^{-2}) was used, as indicated by the slight extension of the shoulder emission at (slightly increased from 1315 to 1498 µJ/cm^{-2}) the maximum laser fluence (**Figure 4-1c**).

From the second slope of dτ/dE in the higher photon energy, the degree of the fluctuating potential can be qualitatively gauged. With larger γ, the density of the band-tail states extends further into the band gap, spanning a larger energy range inside E_g. Since band-tail related recombination are likely to occur when τ varies from 10 ns - 1 µs, a wider energy span of the band-tail will result in a shallower dτ/dE slope. In other words, a steep dτ/dE slope would be observed in a sample with shallow γ. Therefore, a direct indication of the degree of the potential fluctuation can be done by measuring τ at different photon energies. Indeed, the slope of τ vs. photon energies is inversely proportional to γ, with dτ/dE: CIGSSe > CZTSSe-Z2 > CZTSSe-Z6. The γ derived here is also in consistent with the IQE data shown in **Figure 3-1**, with sub-E_g absorption decay slower with longer wavelengths if γ is deeper, *i.e.* the FWHM of d(QE)/dλ peak is broader when γ is deeper.

4.2.5 Defects' Level Derived from Arrhenius Relation

For temperature-dependent PL, a moderate laser fluence was used such that the laser fluence is high enough for PL collection (at high temperature), but low enough to avoid the shoulder emission (band or band-tail relation transition) to occur (*i.e.* the "threshold" laser fluence described earlier). The laser fluence used for each sample is different and adjusted such that the PL emission likely stems from pure QDAP recombination. Therefore, the changes of the PL spectral shapes with temperature are associated with defect recombination and the defect's activation energy (E_a) can be extracted. E_a extracted from the Arrhenius relation could have several contributions, including the depth of the defect states from the band edge (*i.e.* donor or acceptor energy levels), as well as the density of non-radiative states which quench the photo-generated carriers. Both deeper defect levels and the availability of non-radiative states will increase the extracted E_a value from an Arrhenius plot.[86]

Figure 4-5 shows the PL spectra of CIGSSe, Z2 and Z6 recorded as a function of temperature with respective fixed laser fluence, as stated in the figure. An obvious difference between CIGSSe and CZTSSe (Z2 and Z6) was immediately observed- the

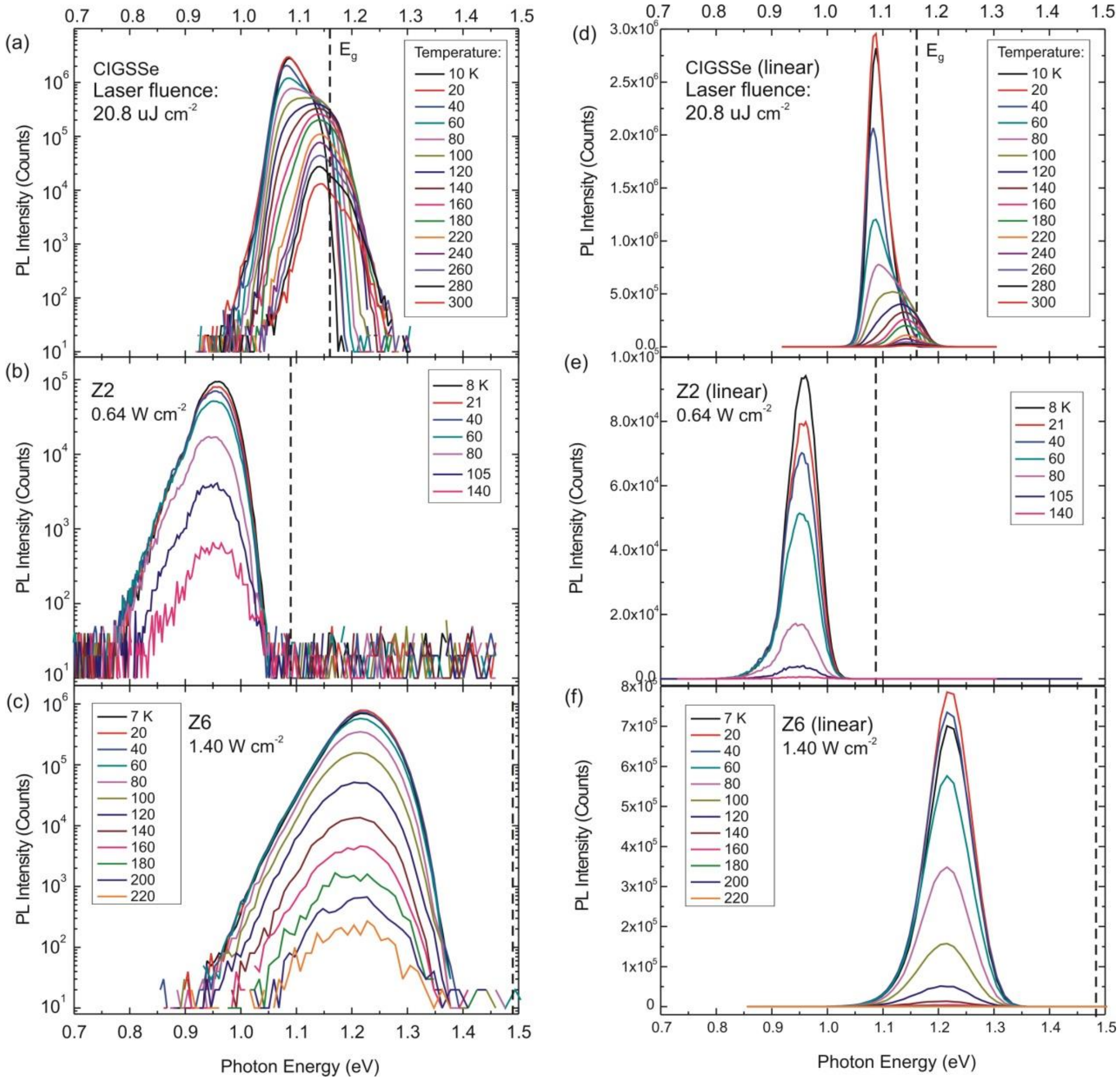

Figure 4-5. Temperature-dependent PL with laser fluence below threshold laser fluence to avoid band-related recombination ("shoulder emission"). Right panels show the PL spectra in linear scale.

PL peak in CIGSSe blue-shifted as temperature increases, whereas such significant blue-shift in peak position were not observed in both Z2 and Z6. The area under curve of PL spectrum (integrated PL intensity) at various temperature were found out and normalized to their respective maximum integrated PL intensity in each case, as plotted **Figure 4-6.** The normalized PL intensity saturates at low temperature (region 1: T < 80 K). As temperature increases (region 2: 80-180 K), carriers were ionized and re-distributed into other energy states, which could include the higher-energy band-tail and band states (depending on the depth of the defects), as well as the non-radiative defect states which quench the PL. As Z2 was excited with a lower laser fluence (to avoid the occurrence of band or band-tail related "shoulder" emission), the PL intensity was lower and PL was fully quenched beyond a temperature of 140 K. Therefore, an Arrhenius rate relation (Integrated intensity I_{PL} = exp(E_a/k_B for all the three materials were fitted on temperature region 2 for a fair comparison of E_a. In addition, previous report has inferred that E_a extracted from 95-170 K is likely related to bulk defects,[84] thus the data gathered between 80-180 K (Region 2) is sufficient for the extraction of E_a for the bulk defects (including the effect of non-radiative states). From the Arrhenius plot in **Figure 4-6**, the extracted E_a values from region 2 are found to be 20.1 ± 7.6 meV, 47.9 ± 6.8 meV and 67.1 ± 26.9 meV for CIGSSe, Z2 and Z6 respectively.

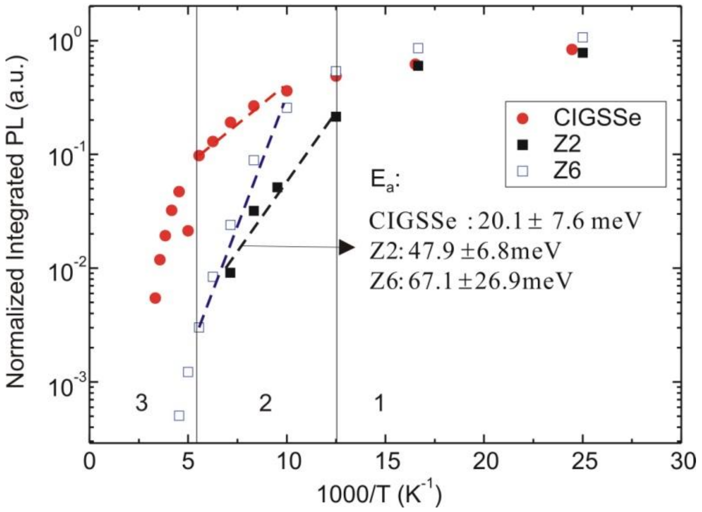

Figure 4-6. Arrhenius plot from temperature-dependent PL. E_a are extracted from region 2 and the dash line shows the Arrhenius fit.

E_a of CIGSSe is shallow and comparable to the thermal energy at room temperature (k_BT ~25 meV, where k_B is the Boltzmann constant). Therefore, the blue-shift of PL peak observed with increased temperature can be explained by ionization of carriers trapped on defect states (at low temperature) to high-energy band-tail or band states (at high temperature), *i.e.* QDAP recombination at low temperature to

BT/BB transition at high temperature, with photon energy close to E_g at room temperature. As carriers become more delocalized at high temperature, they are viable to non-radiative centers or lattice vibration (phonons) activated at high temperature, and thus the PL was quenched with lower PL intensity observed at high temperature. The shallow E_a in CIGSSe also explains the fact that a distinct kink (as in CZTSSe) was not observed in the power-dependent PL spectra of CIGSSe (**Figure 4-1**) because the QDAP recombination and the band-related recombination are not as well separated in energy.

E_a of CZTSSe (Z2 and Z6) is more than doubling compared to CIGSSe, and much larger than the thermal energy at room temperature. This could explain the lack of blue-shift in peak position with temperature in Z2 and Z6, as carriers trapped in the deep defect states were not effectively ionized at high temperature. In addition, the density of non-radiative recombination centers or non-radiative recombination rate could also affect the extracted value of E_a, as discussed earlier. Note that a higher laser was used to excite Z2 and Z6 compared to CIGSSe, but a lower PL intensity was observed at high temperature. Furthermore, the decay rates of PL intensity with temperature are also faster in Z2 and Z6 compared to CIGSSe. These two arguments clearly indicate that higher densities of non-radiative recombination centers are present in CZTSSe.

Comparing the E_a values for Z2 and Z6, the higher E_a value in Z6 with higher S/(S+Se) ratio could have at least two possible explanations: (1) a higher density of bulk non-radiative recombination centers occur in Z6; non-radiative centers are usually deep or mid-gap states, and it is possible that the sample with higher S-content has a higher density of such centers, such as mid-gap S-vacancies as a result of the high volatility of sulphur during annealing.[25, 26] This is also consistent with the deeper defect band at 0.8 eV from the valence band maximum observed in transient photocapacitance spectroscopy, which becomes closer to the center of the gap in high E_g CZTSSe and thus more harmful.[94] (2) Z6 contains deeper intrinsic defect levels; for example, the dominant acceptor defect (*i.e.* the Cu_{Zn} antisite) and other defects (V_{Sn}, Cu_{Sn}, Zn_{Sn}, Zn_{Cu}, Sn_{Cu},Sn_{Zn}, Cu_i, Zn_i, V_S) are found to be deeper in the sulphide-CZTS compared to the selenide-CZTSe by first-principle density functional theory calculation.[25] Note that the deeper defect states and higher density of non-radiative recombination centers could also contribute to the unfavorable increase in ideality factor for higher E_g CZTSSe as shown in **Table 3-1**.

4.3 Conclusion

CZTSSe with low (Z2) and high (Z6) S/(S+Se) ratio were probed by power- and temperature-dependent PL measurement, in comparison with CIGSSe fabricated by similar hydrazine solution-based processing. From power-dependent PL measurement, QDAP density could be estimated from the blue-shift magnitude of the QDAP PL peak, with QDAP density: CIGSSe (10^{16} cm^{-3}) < Z2 (10^{17} cm^{-3}) < Z6 (10^{18} cm^{-3}). Combining with Hall carrier density, the acceptor (N_a) and donor density (N_d) could be derived and the compensation ratio (N_d/N_a) can be calculated. The higher defect density in CZTSSe and the higher compensation ratio in Z6 compared to Z2 will result in a deeper potential fluctuation induced.

QDAP density obtained from PL measurement may not reflect the total defect density (N_t), which could include deep and non-radiative defects. Therefore, N_t was derived from the "threshold" laser fluence which the band-tail related shoulder emission appear, as an indication that sub-E_g states were fully occupied. In highly doped (with high N_t) CZTSSe, defect interaction occurs and electrostatic potential fluctuation induced by charged defects become severe. With estimated N_t, the upper bound for the depth of fluctuating potential (γ) can be calculated and found to be: CIGSSe (36.1 meV) < Z2 (~110 meV) < Z6 (~ 142 meV). This is qualitatively reflected in the changes of recombination lifetime with respect to energy ($d\tau/dE$) also, as reflected by the degree of carrier localization in different energy states.

From temperature-dependent PL measurement, an obvious blue-shift in peak position was observed in CIGSSe as temperature increases, due to thermalization of trapped carriers. But this was not observed in CZTSSe. This is due to a deeper defect level as extracted from Arrhenius relation: CIGSSe (20 meV) < Z2 (48 meV) < Z6 (67 meV). A deeper E_a value could also be due to a higher density of non-radiative recombination centers which quench the PL. This is reflected in CZTSSe with higher PL quenching rate as temperature increases. The higher E_a value in Z6 could possibly be due to the presence of a higher density of non-radiative centers due to S-vacancies.

In a nutshell, the intrinsic absorber quality with deeper electrostatic potential fluctuation, deeper defect levels and higher density of non-radiative recombination centers have a direct impact on the open-circuit voltage (V_{OC}) of CZTSSe solar cells, which also shows a clear trend in $V_{OC,def}$: CIGSSe (547 mV) < Z2 (588 mV) < Z6 (933 mV). Therefore, further improvement in CZTSSe solar cells should focus on reducing defect density and non-radiative recombination channels.

CHAPTER 5 Interfacial Losses of Full Bandgap Range $Cu_2ZnSn(S_xSe_{1-x})_4$ Solar Cells

5.1 Introduction

Earth abundant $Cu_2ZnSn(S_xSe_{1-x})_4$ (CZTSSe) solar cell technology has achieved 12.6% power conversion efficiency (PCE) with an absorber's band gap (E_g) of 1.13 eV.[20] The open-circuit voltage deficit ($V_{OC,def}$: E_g/q - V_{OC}) remains the number one problem in CZTSSe solar cell technology. By increasing the S/(S+Se) ratio, the open-circuit voltage (V_{OC}) is increased but $V_{OC,def}$ is also widened, limiting the maximum attainable V_{OC} and PCE. For example, pure-selenide $Cu_2ZnSnSe_4$ (CZTSe) solar cell with record PCE of 11.6% has a $V_{OC,def}$ of 577 mV[19] while the pure-sulfide Cu_2ZnSnS_4 (CZTS) solar cell with record PCE of 8.4% has a $V_{OC,def}$ of 789 mV.[17] Similarly, the full bandgap range CZTSSe studied here also shows an increasing $V_{OC,def}$ with S/(S+Se) ratio (or E_g), as shown in **Figure 3-2**.

Intrinsic factors such as low carrier mobility, as derived in **Section 3.3**, could lead to recombination loss and higher $V_{OC,def}$ generally observed in CZTSSe solar cells. In addition, the QDAP density and total defect density (N_t) also increases with E_g, leading to a deeper induced fluctuating potential (γ) in CZTSSe by the non-uniform distribution of charged defects (**Section 4.2**). Furthermore, the defect activation energy (E_a) was found to be deeper, and non-radiative recombination was believed to be more effective in high E_g CZTSSe. The deeper γ, E_a, and higher density of non-radiative recombination centers could all contribute to the increasing $V_{OC,def}$ observed in high E_g CZTSSe. Other factors such as low dielectric constant, has also been reported to contribute to $V_{OC,def}$ due to reduced screening of the potential fluctuation.[31, 87] As

$V_{OC,def}$ increases significantly with increasing E_g, there could be additional *extrinsic* factors related to S/(S+Se) ratio or interfacial losses that contribute to $V_{OC,def}$.

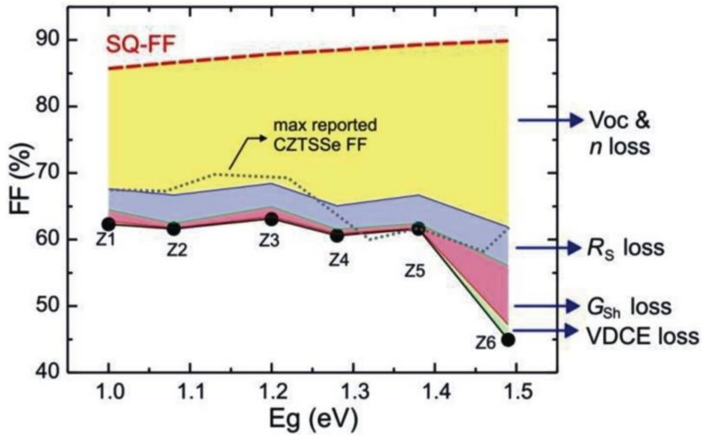

Figure 5-1. Fill factor trend vs. E_g in CZTSSe solar cell, showing the 1 sun J-V fill factor FF (solid dots) of the samples in this study (Z1-Z6) and the corresponding FF according to Shockley-Quisser limit using AM1.5G spectrum (SQ-FF).[9] Various components of the FF losses are shown (see text). Dotted gray line are the maximum CZTSSe FF reported in literature.[22]

Similarly, the J_{SC} deficit due to electrical loss in CZTSSe could also have *intrinsic* and *extrinsic* factors, as indicated in **Section 3.3**. The bulk resistance contributed by the absorber layer ($R_{s,bulk}$ = ρ.t) is minute and could not explain the high series resistance (R_{SL}) observed in high E_g CZTSSe solar cells. This suggests that the *interfacial resistances* could play a significant role in the J_{SC} loss for high E_g CZTSSe solar cells. The high R_{SL} also contributes to the second pressing issue in kesterite technology: the relatively low device fill factor (FF). For example, the current champion CZTSSe device has FF = 69.8% compared to FF = 79.4% in the champion Cu(In,Ga)Se_2 solar cell with the same E_g of 1.13 eV.[20, 73] **Figure 5-1** shows the various contributing factors to FF losses, deriving from Equation (3.7a-c), which includes the V_{OC} and ideality factor (*n*) loss, R_{SL} loss, G_{Sh} loss, and the voltage-dependent collection efficiency (VDCE) loss. As seen in the figure, R_{SL} poses the second most significant factor to FF losses (except in Z6 due to high G_{Sh}). Thus, understanding the dominant contribution from interfacial resistance becomes very important.

R_{SL} of the record CZTSe, CZTSSe, and CZTS solar cells are 0.5, 0.7, and 4.5 $\Omega.cm^2$ respectively,[17, 19, 20] while other literature also reported a high R_{SL} for pure-sulfide CZTS solar cell (> 4 cm^2).[35, 37, 95] The extraordinarily high R_{SL} in CZTS could also be similarly due to interfacial losses as observed here (**Figure 3-3**). One possible causes could be due to the formation of (high E_g) interfacial secondary phases which act as charge blocking layer. Redinger *et al*. has shown that the higher R_{SL} in CZTSSe compared to the CZTSe grown with the same method was attributed to the ZnS formation at the CZTSSe/CdS heterojunction.[35] In another report, ZnS was also detected at the front interface by UV-Raman scattering and R_{SL} was reduced significantly from 13.6 to 3.8 $\Omega.cm^2$ after removing the surface-ZnS by chemical etching using hydrochloric acid (HCl).[36]

Secondary phases were also found at the CZTS/Mo interface: ZnS was found at the back interface in the champion CZTS solar cell.[17] Scragg *et al.* observed ZnS, $Cu_{2-x}S$ and SnS at the back interface of CZTS/Mo.[96] In addition, Fairbrother *et al.* studied the formation mechanism of CZTS by doing physical characterizations (X-ray diffraction and Raman scattering) of thin films sulfurized at various temperature and annealing time; he found that ZnS diffuses to the back interface as annealing time progress, and with sufficient annealing time at 550 °C, the eutectic liquid mixture of Cu_2S and SnS will react with the solid-ZnS and gaseous-S_2 to form CZTS, but excessive ZnS will remain un-reacted and segregate at the CZTS/Mo interface.[37] Therefore, secondary phases formation and their segregation could be dependent on processing technique and also S/(S+Se) ratio. The above reviews show that secondary phases typically co-exist and impact the electrical behavior, especially in pure-sulfide CZTS.

Besides secondary phases formation, thick $MoSe_2$ in the CZTSe/Mo interface was also demonstrated to impact R_{SL} adversely.[97-99] Similar to CIGS solar cell, a thin (~10 nm) interfacial $MoSe_2$ layer will be helpful to improve the adhesion between CZTSSe thin film and the Mo back contact and help to form an ohmic back contact.[100] However, an over-thick $MoSe_2$ layer will deteriorate the electrical contact and increases R_{SL}.[97] Two methods have been proposed to reduce the $MoSe_2$ thickness in CZTSe solar cell by preventing downward-diffusion of Se to Mo back contact: (1) pre-alloying process utilizing the alloy layer as a temporary Se barrier[97] and (2) depositing TiN blocking layer at the Mo to prevent Se diffusion.[99] Both methods can significantly reduce R_{SL}, with method (1) reducing the thickness of $MoSe_2$ layer to < 10 nm.[97]

This chapter aims to investigate interfacial losses that contribute to $V_{oc,def}$ and J_{SC} loss, especially in the high E_g CZTSSe solar cell. This chapter focuses on the investigation of various sources of R_{SL} in the studied kesterite devices; specifically the characteristics of the CZTSSe/Mo interface for CZTSSe with varying S/(S+Se) ratio (Z1-Z6) were investigated. This interface may give rise to large extra parasitic resistance that contribute to the device's R_{SL}. Colour J-V and high intensity colour J_{SC}-V_{OC} measurement were performed to investigate the electrical characteristics of the front (CdS/CZTSSe) and rear (CZTSSe/Mo) junction respectively. Using exfoliation technique to isolate the CZTSSe film from the underlying Mo layer, physical characterizations were done to identify the location of various secondary phases, and to relate their impact to the series resistance. Last but not least, a low E_g secondary phase was found to exist on the p-n interface of Z6 (high E_g CZTSSe) solar cell, which may provide a shunting path and contribute to high G_{Sh} and $V_{oc,def}$. Therefore, phase stability, together with defect physics (as discussed in CHAPTER 4) has to be taken into consideration in further improving the CZTSSe solar cell technology.

5.2 Electrical Characteristics of Interfaces

The Hall Effect measurement on exfoliated films indicates a *p*-type film with decreasing carrier density by almost a factor of 10× from 1.7×10^{16} to 1.4×10^{15} cm^{-3} as the bandgap increases (Z1 to Z6). The mobility ranges from 0.4 to 1.3 cm^2 V^{-1} s^{-1}, independent of E_g as shown in **Table 3-3**. The decrease in carrier density is partly responsible for the increase in series resistance through larger bulk resistance and more propensities towards non-ohmic back contact.

Figure 5-1 presents the E_g dependent characteristics of FF for the CZTSSe samples in this study (Z1-Z6). The maximum possible FF limit was also plotted according to the Shockley-Queisser limit (SQ-FF) under AM1.5G illumination.[8, 9] For comparison, the best CZTSSe FF reported to date is shown as a dotted line [22] and the breakdown analysis of FF losses from all the factors is presented. It was observed that the FF loss factors, (G_S loss and VDCE) loss, have much less contribution compared to (V_{OC} loss, *n* loss and R_S loss), thus we focus on the R_S loss factor as $V_{OC,def}$ issue has been studied extensively in CHAPTER 3.

It was observed that R_{SL} increases with E_g (or S-content) in **Figure 3-3**. The (overall) series resistance was contributed by various factors: (1) Top contact resistance (includes distributed resistance of the contact grid), (2) transparent conducting oxide (TCO) resistance, (3) CdS buffer layer resistance, (4) CZTSSe absorber resistance, (5) back metal contact (Mo) spreading resistance, (6) front CdS/CZTSSe interface or barrier resistance, (7) CZTSSe/Mo back contact resistance. In a good thin film solar cell like CIGSSe, the absorber with the thickest layer dominates R_S; However, the front (CdS/CZTSSe) and rear junction (CZTSSe/Mo) resistance remain largely undetermined and could become dominant in CZTSSe solar cells.

Among these R_S loss factors, the top stack contribution (1-3: Ni/Al contact grid, TCO and CdS) and bottom Mo spreading resistance (5) are approximately fixed in all devices and independent of the absorbers' E_g. Their total contributions are estimated to be $< 0.3\ \Omega\ \text{cm}^2$. The absorber (4) and interfacial junction resistance (6: front, and 7: rear) are expected to vary with E_g or the sulfur composition. **Figure 3-3** has shown that the R_{SL} extracted from the J-V curves of the full devices as a function of E_g does not fully account for the overall increasing R_{SL}. Therefore, the substantial increase of R_S in high E_g devices suggests an additional contribution, which can be narrowed down to the impact at either the front or rear interface which could serve as a current blocking barrier or non-ohmic junction.

5.2.1 Front Interface Secondary Barrier Issue

The possibility of a front interface (CdS/CZTSSe) secondary barrier was first considered, which could severely harm the FF if the conduction band offset (CBO) are large and "spike-like" with CBO ≥ 0.5 eV [12, 101] because the large barrier blocks the minority carrier transport. In high-performance hydrazine-processed and vacuum-processed CZTSSe devices (E_g = 1.0- 1.5 eV) the CBO between the CdS and CZTSSe is found by UV photo-electron spectroscopy to be spike-like with offset < 0.5 eV.[102] There is also report of a cliff-like CBO in high E_g-CZTS/CdS interface by ultraviolet and inverse photo-electron spectroscopy.[103] Therefore, we do not expect the front interface to degrade the FF severely since there is no evidence of a barrier larger than 0.5 eV.

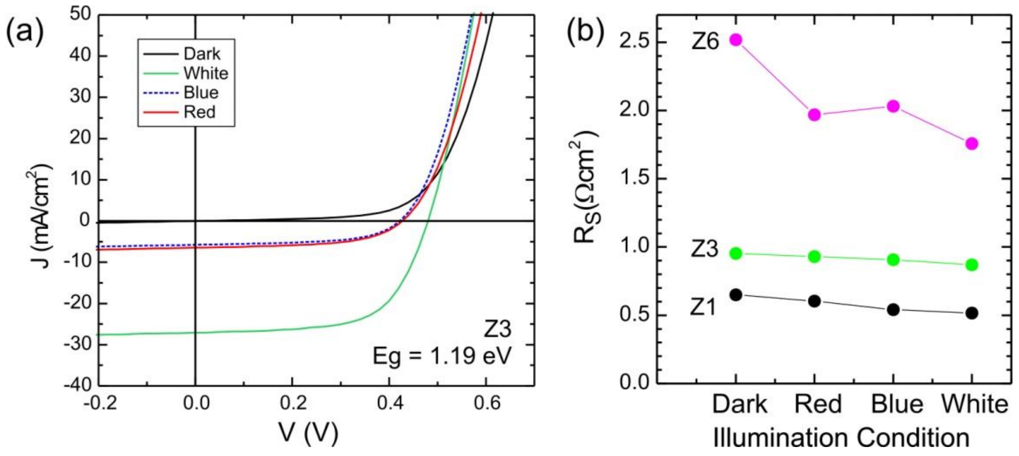

Figure 5-2. Front interface (CdS/absorber) secondary barrier diagnostics: **(a)** J-V under dark, light, red (600 nm long pass filter) and blue (600 nm short pass filter) illumination. **(b)** R_S as a function of illumination condition.

The above hypothesis can be tested by performing J-V sweeps under 1 sun illumination (100 mW/cm^2) with different light illumination, *i.e.* white (no filter), blue (short pass 600 nm filter, "SP600"), red (long pass 600 nm filter, "LP600") and dark as shown in **Figure 5-2**. It was observed that there is no distortion in the red J-V curve ("red kink") that can occur in devices with significant secondary barrier at the front interface.[12] Upon extracting the device parameters with the help of Lambert-W function on all the color *J-V* curves (within one device), the FF and R_S were found to be similar between various illumination conditions,[104] as shown in **Figure 5-2(b)**. However, there is a mild increase in series resistance from white → blue → red to dark, which is common in thin film solar cell and could also be due to a mild photo-doping effect. Note that similar observations are also found in the rest of the devices, thus it can be concluded that the secondary barrier is not a significant factor in the FF losses in these devices.

5.2.2 Back Contact Interface Secondary Barrier Issue

The characteristics of the back contact (CZTSSe/Mo) interface was examined using high intensity (~300 Suns) Suns-V_{OC} (or J_{SC}-V_{OC} study) on the full devices.[66] Besides

J_{SC}-V_{OC} measurement with full sun spectrum, blue (using SP600) and red (using LP600) illuminations were used to probe the depth sensitivity. The long wavelengths illumination (red) penetrates deeper and reach out more to the back contact interface due to lower absorption coefficients.

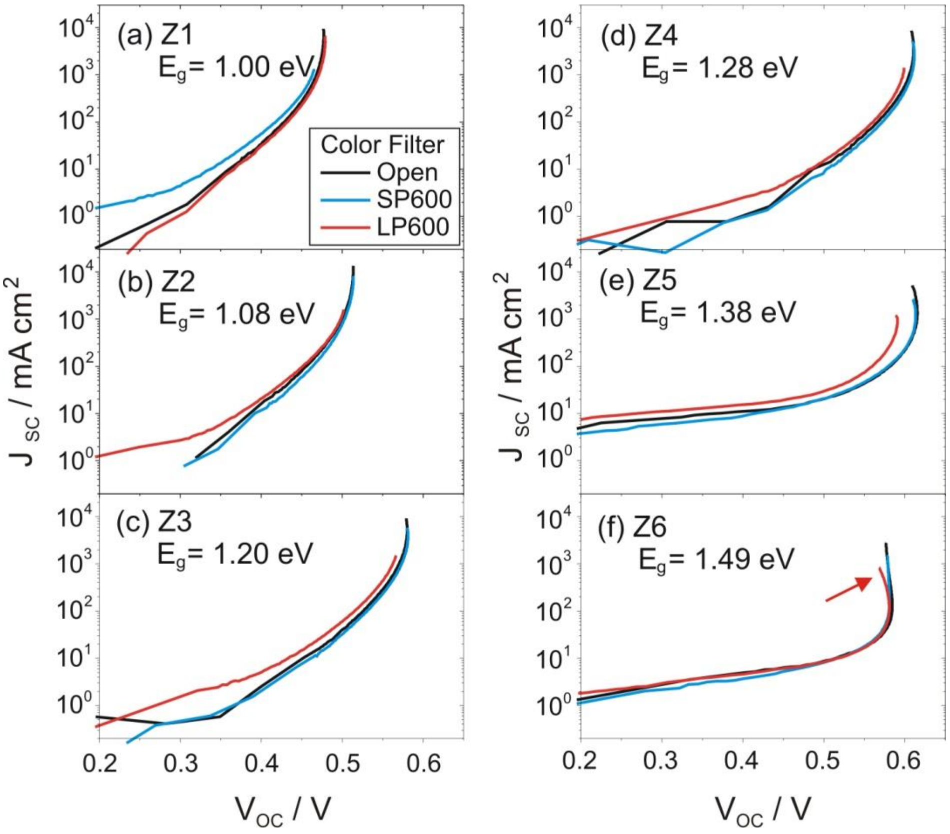

Figure 5-3. Back interface (CZTSSe/Mo) diagnostics with high intensity J_{SC}-V_{OC} measurement (~300 suns max.) [66] at three different illumination conditions: (1) No Filter (2) Blue (SP600); and (3) Red (LP600) illumination. Backward V_{oc} bending becomes more severe as E_g increases, indicating a non-ohmic back contact at high-S CZTSSe. This is most obvious in Z6 when the "red" J_{SC}-V_{OC} curve (see arrow) gives a more severe bending than the "blue" curve.

Figure 5-3 shows the J_{SC}-V_{OC} for each device with E_g ranging from 1.00 to 1.49 eV. V_{OC} pinning at high light intensity was observed in low E_g devices (Z1-Z3), which could be due to low bulk conductivity and/or bulk or interface defects.[66] With higher E_g (Z4-Z6), increasing V_{OC} backward bending was observed. The V_{OC} bending behavior was best observed in Z6 with red-illumination (arrow in **Figure 5-3 (f)**) compared to the illumination without filter ("Open") and with blue-illumination

(SP600). Previous report has shown that the V_{OC} bending behavior can only be explained by non-ohmic back contact issue.[66] This suggests the presence of non-ohmic back contact at the CZTSSe/Mo interface in high E_g CZTSSe solar cells (Z4-Z6). We note that the variations in absorbers' thickness may affect the penetration depth of the red-light, but Z2-Z5 with similar thickness show an increasingly bending behavior as E_g increases, and thus it can be concluded that the non-ohmic back contact were developed in the high E_g CZTSSe devices.

There are two possible causes for the presence of non-ohmic back contact: (1) very low carrier density (as shown in **Figure** 3-6) for high E_g CZTSSe results in the formation of Mott-Schottky back contact; (2) presence of secondary phases acting as a charge blocking layer at the back contact interface. Factor (1) has been explained earlier, which the carrier density for Z6 was reduced to as low as 1.4×10^{15} cm^{-3}. This provides at least one mechanism to account for the non-ohmic back contact in high E_g samples. The following physical characterizations intend to investigate the occurrence of secondary phases at the CZTSSe/Mo back interface.

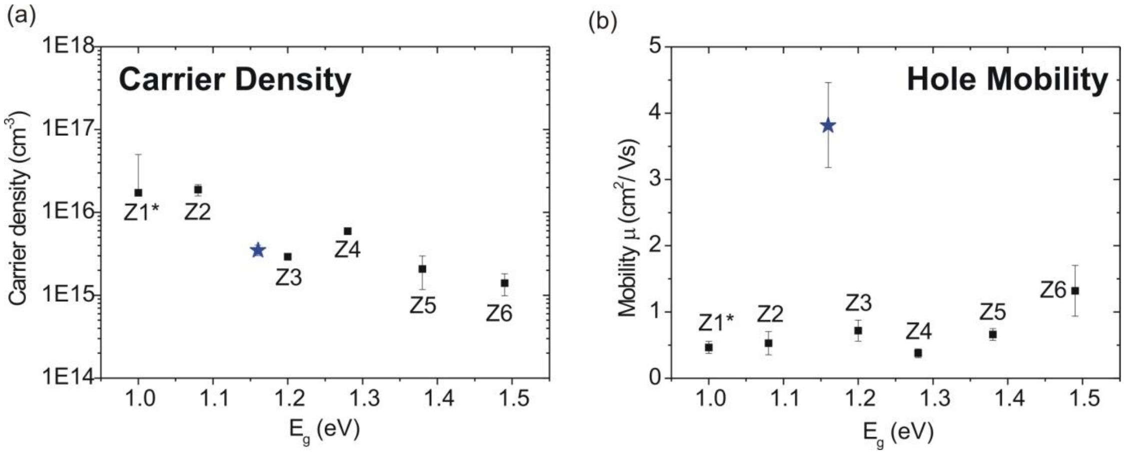

5.3 Physical Characteristics of Interfaces

Glancing Incidence X-ray Diffraction (GIXRD)

Glancing-incidence X-ray diffraction (GIXRD) was scanned on the *as-grown* sisters' CZTSSe/Mo thin films (Z1'-Z6'), as shown in **Figure 5-4** with a glancing incidence angle of 10°. The peak intensities were normalized to the main (112) peak intensity of CZTSSe, and shifted vertically for clarity. CZTSSe-related peaks are marked with the diffraction plane indices (*hkl*), and it was observed that the XRD peaks shifted to higher 2θ angle as the S/(S+Se) ratio increases. This is understood as Se-substitution by smaller S-atom reduces the CZTSSe's lattice constant and the inter-planar distance. Mo-peak from Mo/SLG substrate was also observed, indicating that the X-ray penetrates throughout the absorbers' thickness with an incidence angle of 10°. A higher Mo-peak intensity at 40.5° was observed in Z6 due to the thinner absorber's thickness.

XRD peak at ~14.6° (marked by arrow in **Figure 5-4**) was observed in high-E_g CZTSSe films (Z4'-Z6'), with an increasing normalized (to remove signal variation effect due to different absorbers' thickness) peak intensity as the E_g increases. Normalizing the XRD peaks to the Mo-peak intensity at 40.5° also shows an increasing normalized peak intensity at ~14.7° (not shown), indicating that this peak is closely related to the S/(S+Se) ratio.

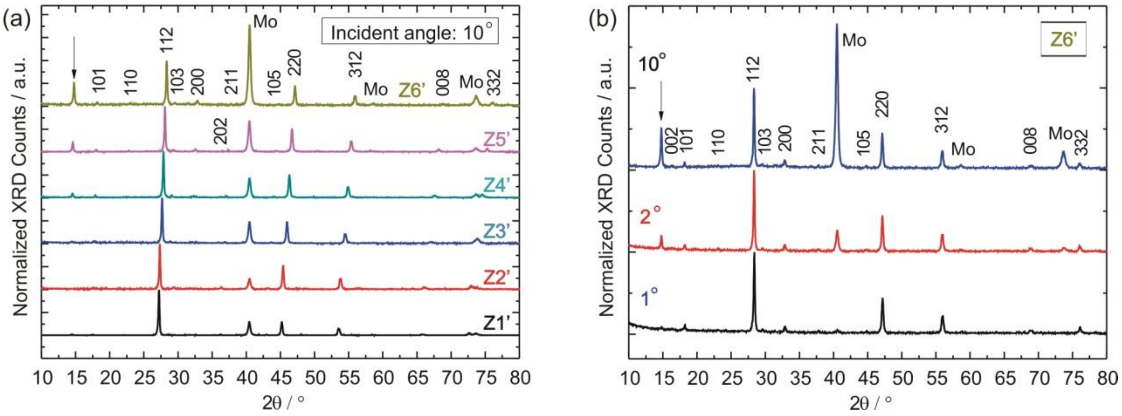

Figure 5-4. Glancing-angle X-ray diffraction (GIXRD) with **(a)** incident angle of 10° for Z1'-Z6' (bare-CZTSSe films grown on Mo substrate). XRD peak at ~14.6° (marked by arrow) was found in high S/(S+Se) CZTSSe (Z4'-Z6'). **(b)** GIXRD on Z6' with different incident angles. Increasing intensity of the ~14.6° peak suggests that the related phase is located at the back interface. The XRD counts are normalized to the (112) peak and shifted vertically for clarity.

The ~14.6° peak can be assigned to the (001) diffraction plane of hexagonal-SnS_2 (ICDD PDF-00-023-0677). It was noted that this peak shifted to higher 2θ angle as E_g increases (Z4': 14.52°; Z5': 14.60°; Z6': 14.76°), indicating a S-Se-mixed $Sn(S,Se)_2$ phase could form at the high-E_g CZTSSe. To know the segregation location of this phase, GIXRD with different incident angle (1°, 2°, 10°) was done on Z6', as smaller incident angle is more surface-sensitive (indicated by the absence of Mo-peak). **Figure 5-4(b)** shows that the normalized peak intensity at 14.76° increases with the incidence angles, indicating that the $Sn(S,Se)_2$ phases formed in high-E_g CZTSSe samples should be located at the back interface (CZTSSe/Mo). There could be other secondary phases with XRD peaks overlap with the peaks of CZTSSe.

Field-Effect Scanning Electron Microscopy (FE-SEM)

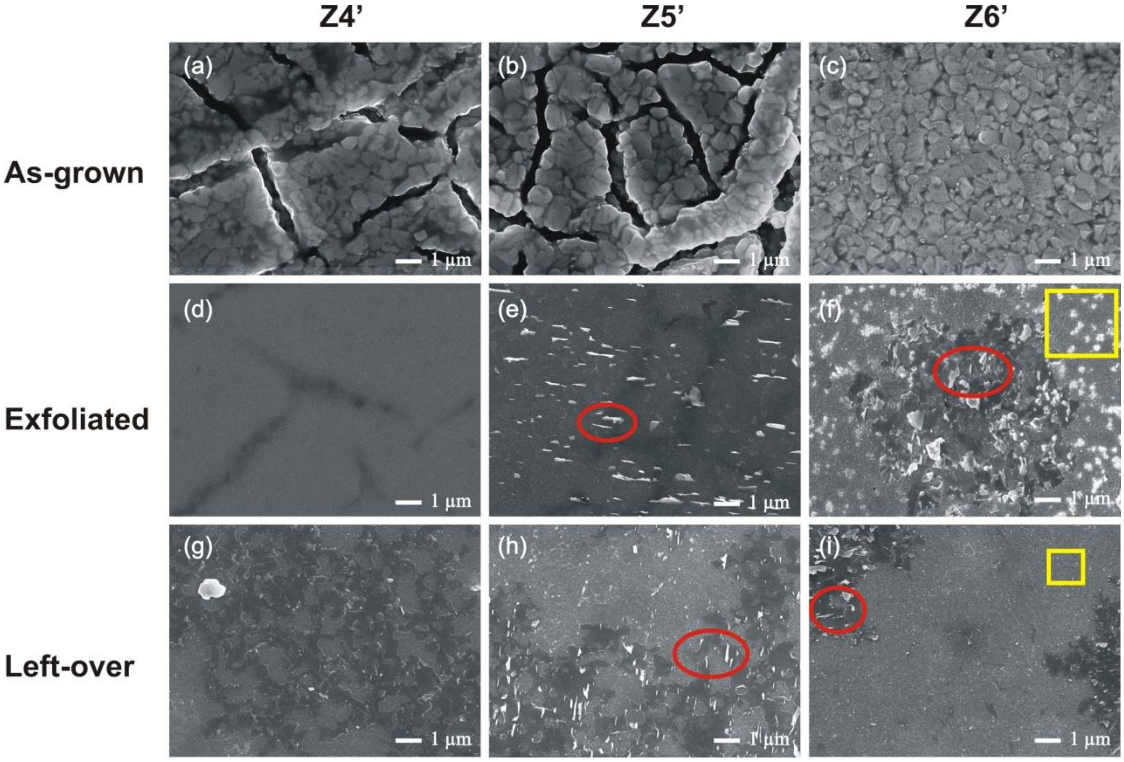

Figure 5-5. FESEM images of as-grown **(a-c)**, exfoliated **(d-f)** and leftover region on Mo substrate **(g-i)** of Z4'- Z6'. Significant amount of $Sn(S,Se)_2$ flake-like structures were observed at the exfoliated and left-over region of Z5' and Z6' (red circles). Bright-dot structures (possibly ZnS) were also observed in the exfoliated and left-over region of Z6' (yellow triangles). FESEM images for Z1'-Z3' are provided in the in Figure 5-6.

SnS_2 is a polytypic layered compound with a flake-like structure and an indirect E_g of ~2.2 eV.[105] With this information, we exfoliated the bare CZTSSe films from the Mo-substrate and image under scanning electron microscope (SEM). **Figure 5-5** shows the SEM images of the as-grown CZTSSe films on Mo substrate (a-c: Z4'-Z6'), the exfoliated CZTSSe films on quartz substrate (d-f: Exfoliated Z4'-Z6') and the left-over region on the Mo substrate after exfoliation (g-i: Leftover Z4'-Z6'), all in the same magnification. Significant cracks were observed on the as-grown Z4' and Z5', especially in Z5', that partly account for the high bulk absorber $R_{S,\text{ CZTSSe}}$ of Z5' above the extrapolated line (**Figure 3-3(b)**). Importantly, a significant amount of flake-like structures (bright contrast due to charging in higher E_g of $Sn(S,Se)_2$) were observed in both (due to the brittle behavior of layered compound) the Exfoliated *Z5'-Z6'* and the Leftover *Z5'-Z6'*. The increasing amount of the flake-like structures as E_g increases is consistent with the GIXRD results described above (**Figure 5-4(a)**). In addition, bright-dot structures were also observed in the exfoliated-Z6' (**Figure 5-5 (f)**), which could be another secondary phase with high E_g (possibly ZnS). Both the flake- and dot-like structures were not observed in Z1'-Z3', as shown in **Figure 5-6** below.

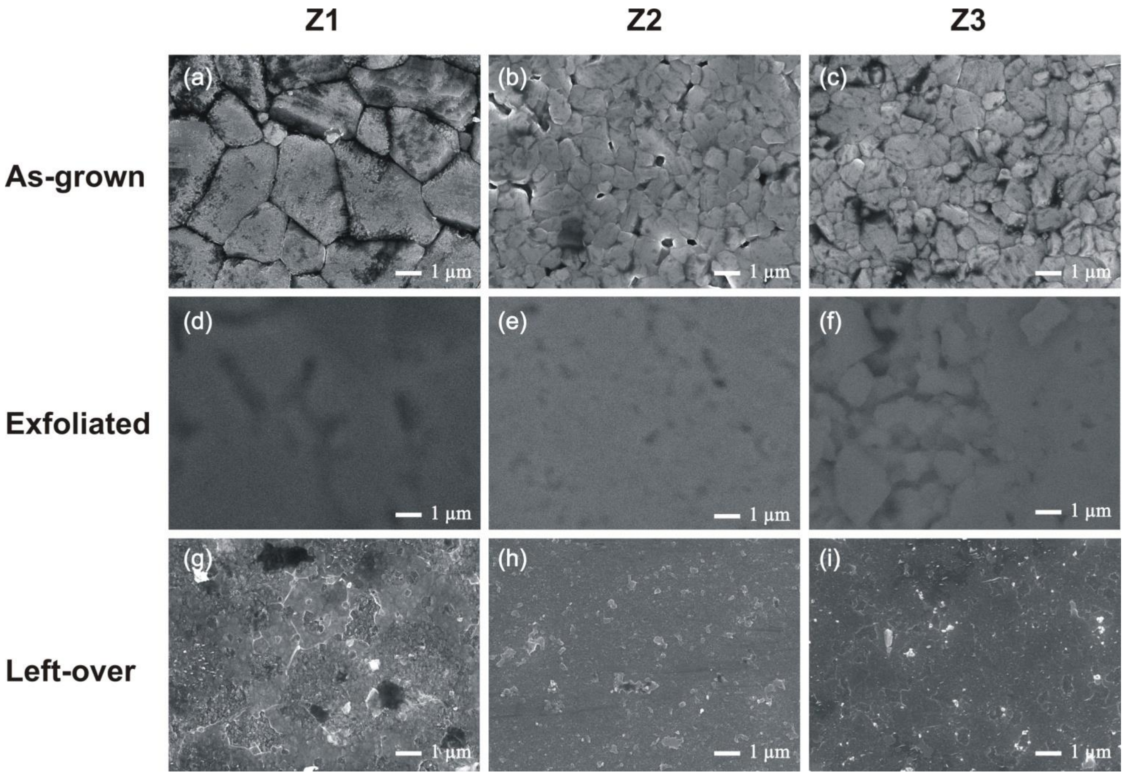

Figure 5-6. FESEM images of as-grown (a-c), exfoliated (d-f) and leftover region on Mo substrate (g-i) of Z1, Z2 and Z3. No obvious flake-like and bright-dot structures were observed in the exfoliated and leftover region of these low S/(S+Se) CZTSSe samples.

Raman Scattering/Raman Mapping

Raman mapping with laser excitation wavelength of 514 nm has a penetration depth of 50 to 150 nm for Z2'-Z6', depending on the absorption coefficient. Therefore, the probing depth is considered "surface" sensitive compared to the absorbers' thickness. By probing on the as-grown- (surface), exfoliated-CZTSSe (back interface) films and the left-over regions on Mo-substrate after exfoliation (back interface), complementary information on the location of the secondary phases can be obtained (**Figure 5-7**). For easy reference, all the 81 Raman spectra from the mapping were consolidated and represented by a single curve if all the 81 curves have an overlapping Raman spectrum. **Figure 5-7 (a)** shows such an example where all the 81 curves overlap from the Raman mapping on the as-grown Z2'-Z6'. All the curves were normalized to the peak with maximum intensity and shifted vertically for clarity. CZTSSe with intermediate S/(S+Se) ratio exhibits a bimodal behavior in phonon vibrations. The main peaks are attributed to the A_1 vibration mode of S (Z2' to Z6': 191, 202, 213, 216, 233 cm^{-1}) and Se atoms (Z2' to Z6': 322, 324, 325, 325, 329 cm^{-1}) surrounding the cations.[106] The peak shift is due to the increased vibrational frequency resulted from lighter S atoms.[107] Note that a small peak at ~280 cm^{-1} (marked by arrow in **Figure 5-7 (a)**) was observed on the *surface of Z6' only*, which could be attributed to $Cu_2Sn(S,Se)_3$ (CTSSe).[37] If this is the case, this might explain the high G_S in Z6 due to the low E_g (0.67- 1.35 eV) of CTSSe compared to E_g of Z6 (1.49 eV), providing a shunting path for the photo-generated carriers.[108]

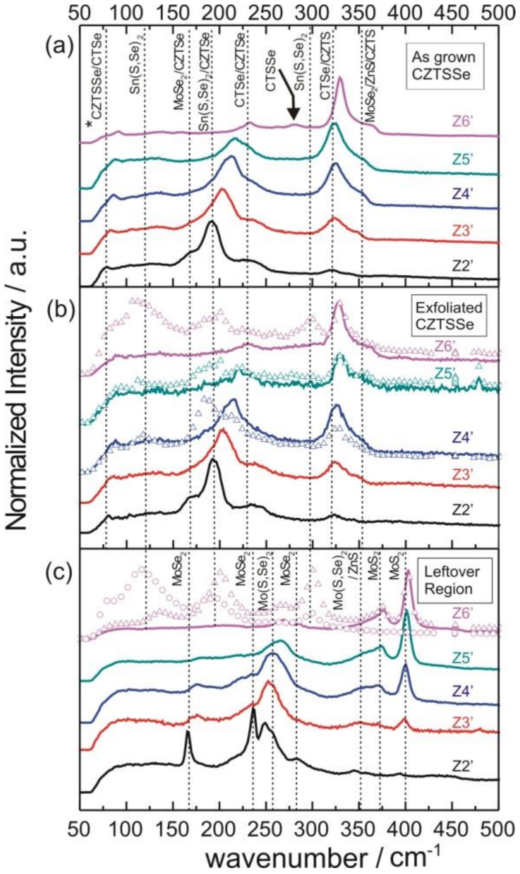

Figure 5-7. Raman spectra on (a) as-grown (Z2'-Z6'), (b) Exfoliated Z2'-Z6' and (c) Leftover Z2'-Z6'. "Special" Raman spectra (hollow symbols) which appear in a few point scans (among the 81 point scans in Raman mapping) were observed in the Exfoliated *Z4'-Z6'* and Leftover-*Z6' only*. Each curve is normalized to the peak with maximum intensity and shifted vertically for clarity.

Figure 5-7(b) shows the Raman spectrum for the Exfoliated Z2'-Z6', which probe bottom surfaces of CZTSSe in the CZTSSe/Mo back interface. The exfoliated-Z2' and Z3' show exactly the same Raman spectra with their as-grown (surface) counterparts, with overlapping 81 curves from the Raman mapping. With increasing S/(S+Se) ratio, "*special*" (indicated by hollow triangle symbols) Raman spectra deviate from the majority Raman spectra (indicated by solid curves) in the Exfoliated *Z4'-Z6'* only. These "special" peaks were found at 183 cm^{-1} for Exfoliated-Z4'; 193 cm^{-1} for Exfoliated-Z5'; 114, 201 and 302 cm^{-1} for Exfoliated-Z6'. With mixed S-Se content in Z4'-Z6', all these "special" peaks could be attributed to **Sn(S,Se)$_2$**.[109] Similar peaks were also found in the Leftover-Z6' (**Figure 5-7 (c)**), due to the significant amount of flake-like structures observed in the SEM image [**Figure 5-5 (f)**] and the brittle behavior of layered $Sn(S,Se)_2$ structure.[105] Leftover Z2'-Z5' did not show the $Sn(S,Se)_2$- related Raman peaks, but obvious Raman peaks of **MoS_2** (377 and 403 cm^{-1}),[110] **$MoSe_2$** (165, 237 and 283 cm^{-1}) [110] and **$Mo(S,Se)_2$** (249-265, 345-350 cm^{-1}) [111] were observed. These peaks were not observed in the exfoliated films, indicating the $Mo(S,Se)_2$ phases were remained on the Mo-substrate after exfoliation. As UV laser and NIR laser are not available for (near) resonant Raman spectroscopy, ZnS(e) and $Cu_2SnS(e)_3$ secondary phases cannot be ruled out from this investigations as they have overlapping Raman spectrum with CZTSSe.[112] In addition, it was believed that ZnS or Zn(S,Se) phases exist at the back interface (CZTSSe/Mo) of Z6' as SEM shows a "bright-dot" structures (**Figure 5-5 (f)**).

X-ray Photoelectron Spectroscopy (XPS) and XPS Depth Profiling

To summarize the physical characterizations obtained so far, flake-like-$Sn(S,Se)_2$ and $Mo(S,Se)_2$ phases were observed at the back interface of high-E_g CZTSSe. However, dot-like structures (possibly a high E_g secondary phase) observed in SEM image of exfoliated-Z6' (**Figure 5-5 (f)**) could not be identified by GIXRD or Raman spectroscopy. Therefore, X-ray photo-electron spectroscopy (XPS) and XPS depth profiling on the Exfoliated-Z6' was performed. **Figure 5-8 (a)** shows the wide-scan XPS spectra for the as-loaded and sputtered (at various time duration) Exfoliated-Z6'. Immediately from the wide-scan spectrum of the as-loaded Exfoliated-Z6', the obvious Zn *2p* and Sn *3d* peaks were observed accompanied by the adventitious C *1s* and O *1s* peaks, without the presence of Cu *2p* peak. Even after 30s sputtering to remove the adventitious C, Cu *2p* peak are still comparably weaker than Zn *2p* and Sn *3d* peaks. This indicates a **Zn- and Sn-rich back interface**, consistent with other physical characterizations shown above. With sputtering duration increases, the relative intensity of Cu *2p* peak increases with the adventitious C *1s* and O *1s* peaks faded.

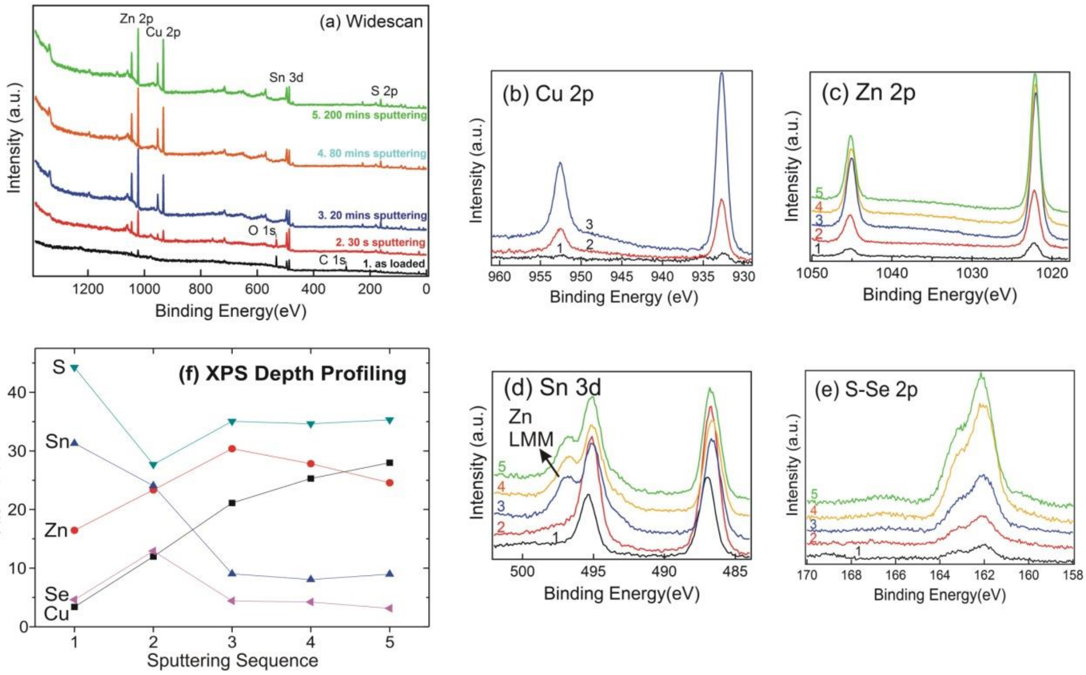

Figure 5-8. XPS **(a)** wide-scan on as-loaded and sputtered Exfoliated-Z6' (shifted vertically for clarity); **(b)-(e)** narrow scans on Cu *2p*, Zn *2p*, Sn *3d* and S-Se *2p* peaks respectively; The shoulder peak of Line 2 (30s sputtering) in (d) is the Auger peak of Zn $L_3M_{45}M_{45}$, found typically in CZTS crystals.[113] **(f)** Atomic % at each sputtered layer.

Figure 5-8 (b-e) shows the narrow scans on the elements Cu *2p*, Zn *2p*, Sn *3d* and S-Se *2p* peaks respectively, after each sputtering events (1: as loaded, 2: 30 s sputtering, 3: 20 mins sputtering, 4: 80 mins sputtering, 5: 200 mins sputtering, cumulative time duration). There were literally no peak-shift for Cu *2p*, Zn *2p*, and S-Se *2p* peaks, but a small red-shift in binding energy for Sn *3d* peak with increasing sputtering time was observed (Sn $3d_{5/2}$ peak shifted from 487.0 to 486.7 eV). This peak shift could be due to the changing chemical environment around Sn-atom, with transition from hexagonal-$Sn(S,Se)_2$ at the back interface to the bulk tetragonal-CZTSSe. The peaks' position of Sn *3d* correspond well to an oxidation state of +4.[114] Transition to +2 state at the back interface (as-loaded) is not likely as the binding energy observed here was higher than the sputtered one.[115]

Peak shift in Zn *2p* is not observed, probably due to the similar tetragonal crystal structure (chemical environment) between ZnS and CZTSSe, with Zn surrounded by four chalcogen atoms. Furthermore, a shoulder peak was observed near the Sn $3d_{3/2}$ peak, which is attributed to Zn-Auger peak $L_3M_{45}M_{45}$ was normally seen in CZTSSe crystal.[113] This indicates that the CZTSSe phase was only detected after 20 mins sputtering (shorter sputtering was not done) - a clear sign of secondary phases formation at the back interface.

To examine the chemical composition at each sputtered layer, the areas under curves of Cu $2p_{3/2}$, Zn $2p_{3/2}$, Sn $3d_{5/2}$ and S-Se *2p* were fitted by applying Shirley-background subtraction followed by a Lorentzian-Gaussian fit. Area-under-curve of the fitted peaks was normalized by the relative sensitivity factor (RSF) for respective element and the atomic % of each element was calculated. As-loaded XPS scans show a Zn- and Sn-rich composition (with almost no Cu) at the back interface [**Figure 5-8 (f)**]. After subsequent sputtering, Sn atomic % drops, followed by the reduction of Zn atomic %, whereas Cu atomic % increases. It is only after 200 mins of sputtering that Cu atomic % exceeds Zn atomic %. This indicates that a thick Zn-rich layer was formed at the back interface. Thickness of the post-sputtered film (after 200 mins sputtering) was found to reduced by 200-300 nm, indicating that the Zn-rich layer at the back interface is significantly thick, consistent with previous report on the record-CZTS solar cell.[17] Furthermore, as the X-ray spot for XPS detection has an oval profile with diameters ~2×3 mm, the Zn- and Sn-rich secondary phases formed at the back interface of Z6' could be considered continuous and thus contribute significantly to the R_{SL} of Z6. Although a continuous dot-structure was not seen in the FE-SEM image of Exfoliated-Z6', the possibility of amorphous ZnS formation at the back interface should not be excluded.

5.4 Discussions on Secondary Phase Formation

$Sn(S,Se)_2$, $Mo(S,Se)_2$ and Zn(S,Se) phases were found at the back interface of high-E_g CZTSSe. In high S/(S+Se) ratio, the sulfide-based secondary phases may dominate. All these secondary phases have a large E_g, with E_g of 2.24 eV for the hexagonal SnS_2,[105] and 3.68 eV for the zinc-blende ZnS.[116] For SnS_2, it is also reported that the band alignment with CZTSSe may induce a hole blocking layer for charge injection into the Mo-electrode.[105] Having a huge E_g in ZnS, there is no doubt that ZnS may also act as a hole blocking layer. Although MoS_2 has a lower E_g (1.23 eV) than CZTS and a benign valence band offset to CZTS for hole injection,[117] but several reports have shown a detrimental effect on increasing R_S with thick $MoSe_2$ in the CZTSe/Mo interface, as the conversion of Mo to $MoS(e)_2$ could reduce the thickness of Mo and thus increase the contact resistance.[97-99]

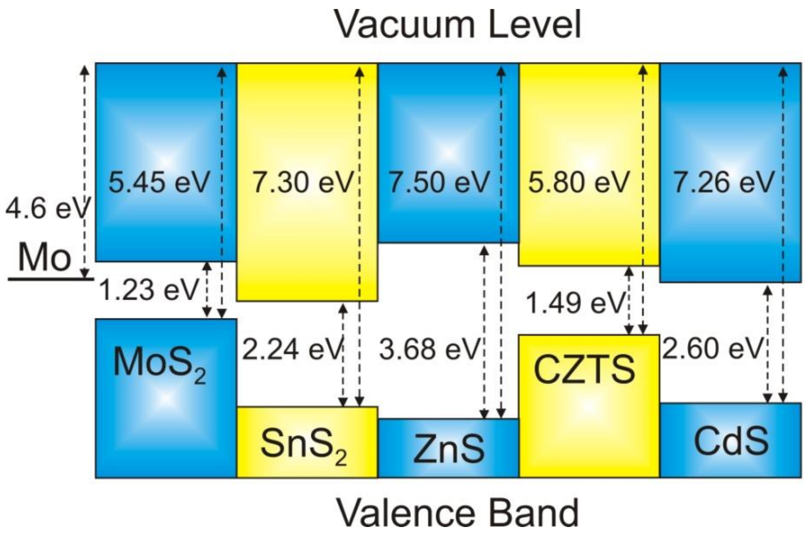

Figure 5-9. Band alignment of CZTS with different other compounds.

From the physical characterizations, we observe an increasing trend on the formation of secondary phases as S/(S+Se) ratio increases, consistent with other reports. This could be understood from the calculated phase diagram in CZTSe and CZTS by Chen *et al.*[25] Assuming a slightly Cu-poor environment in both CZTS and

CZTSe (a fixed chemical potential of Cu, μ_{Cu} = -0.2 eV), SnS_2 will form even at relatively Sn- poor environment (μ_{Sn} ~ -1.3 eV) in CZTS, while a higher tolerance of Sn-chemical-environment (μ_{Sn} ~ -1.0 eV) is observed in CZTSe to avoid the formation of $SnSe_2$. Similarly, Cu_2SnS_3 in CZTS (start to form at μ_{Sn} ~ -2.0 eV) is also more likely to occur compared to Cu_2SnSe_3 in CZTSe (start to form at μ_{Sn} ~ -1.4 eV). In other words, the μ_{Sn} range (between -1.20 to -0.65) for stable CZTSe phase is more negative (poorer Sn-environment) than the μ_{Sn} range (between -1.10 to -0.40) for stable CZTS phase. This may help to explain the $Sn(S,Se)_2$ phase observed in Z5'-Z6' and Cu_2SnS_3 observed in Z6', as the same metal composition in the precursor solution [Cu/(Zn+Sn) = 0.8; Zn/Sn = 1.1] were used in the fabrication for all Z1-Z6. Although such phases could be avoided in CZTS by reducing Sn-content, Sn-related defects (e.g., vacancies V_{Sn}, substitutional defects Cu_{Sn} and Zn_{Sn}) with deep energy levels are likely to occur which will deteriorate the solar cells.[25]

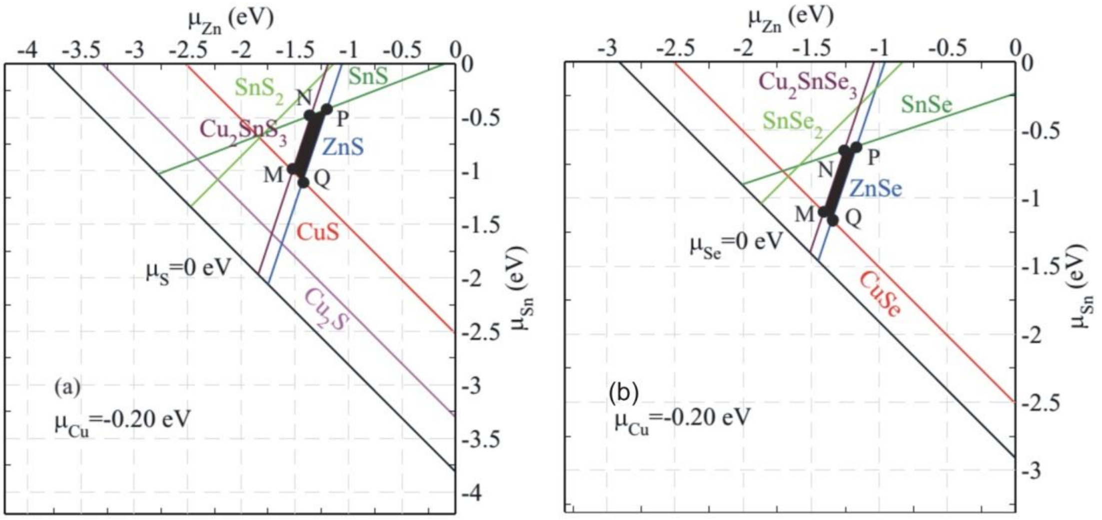

Figure 5-10. The calculated stable chemical potential region (black area) of Cu_2ZnSnS_4 (left) and $Cu_2ZnSnSe_4$ (right) in (μ_{Sn}, μ_{Zn}) planes with fixed μ_{Cu} at -0.20 eV.[25]

Similar argument for ZnS (start to form at μ_{Zn}~ -1.75 eV) in CZTS and ZnSe (start to form at μ_{Zn}~ -1.40 eV) in CZTSe can also be made to explain the Zn-rich phases forming at the high S/(S+Se) CZTSSe.[17, 37, 96] Therefore, secondary phases typically co-exist with CZTS, which inhibits the device performance by acting as highly resistively dead region (high R_S) or providing shunting path (high G_S) which quench the device's FF. This partly explains the record-CZTSSe solar cells generally have a lower range of E_g between 1.13-1.16 eV.[20, 40, 68, 118] Existence of low bandgap secondary phases also provide additional loss factor on the high $V_{OC,def}$ of high-E_g CZTSSe solar cells, besides the intrinsic deeper defects, potential fluctuation and low carrier mobility.

5.5 Conclusion

In conclusion, CZTSSe solar cells over a full bandgap range (1.0- 1.5 eV) were studied and an increasing R_S was observed, contributing to the J_{SC} loss and lower FF as the S/(S+Se) ratio (or the bandgap) increases. Several factors contributing to R_S were discussed, with the interfacial resistance being the dominant loss factor. From color J-V measurement, no evidence of resistive front *p-n* interface was found. However, J_{SC}-V_{OC} measurement revealed a non-ohmic back contact developed in the high-E_g CZTSSe solar cells. The non-ohmic back contact could be due to Schottky barrier formation (as carrier concentration reduces at higher bandgap) and/or secondary phases formation at the CZTSSe/Mo back interface.

With different physical characterizations on the sisters' bare CZTSSe films and the exfoliated-films, $Sn(S,Se)_2$, Zn(S,Se) and $Mo(S,Se)_2$ phases were found at the CZTSSe/Mo interface in Z5'-Z6' (with high S/(S+Se) ratio). The presence of these high bandgap secondary phases at the back interface could act as charge (hole) blocking layer, which contribute to the high R_S and low FF observed in high bandgap CZTSSe solar cells. The presence of secondary phases in high S/(S+Se) ratio could be understood from the theoretical phase diagram. Compared to CZTSe, CZTS has a lower tolerable range of chemical potential (more negative) in forming secondary phases.

As secondary phases are generally found at the back interface, back contact engineering (exfoliation followed by chemical etching of secondary phases and re-deposition of metal electrode) could be designed to improve the device performance, especially for the high bandgap CZTSSe solar cells. Lastly, the presence of low bandgap secondary phases at the front p-n interface (CZTSSe/CdS) of Z6' may provide a shunting path and contribute to the high $V_{OC,def}$ and high shunt conductance observed.

CHAPTER 6 Enhanced Grain Growth and Suppressed Non-Radiative Recombination in $Cu_2ZnSn(S,Se)_4$ by Antimony Doping

6.1 Introduction

Previous chapters have described the intrinsic and extrinsic limitations of CZTSSe solar cell fabricated by hydrazine pure-solution process, which provides a few directions for improvement. Sb-doping has been reported to promote grain growth and improve the intrinsic quality of the CZTSSe absorbers with improved V_{OC}.[119, 120] However, the effect on solar cell performance was not clearly understood. For example, the largest-grain-size CZTSSe with the highest Sb-doping concentration do not necessarily give the highest open-circuit voltage (V_{OC}) and power-conversion efficiency (PCE). Therefore, further investigation is required to understand the mechanism of improvement for better utilization. In this chapter, hydrazine was replaced with other non-toxic solution processing for green synthesis of CZTSSe, and focus on improving the intrinsic crystal quality by external doping (Sb) on CZTSSe fabricated by non-toxic solution processing.

Many approaches have been proposed to produce CZTSSe absorber layers, including vacuum deposition,[121-123] electro-deposition,[124-127] nanocrystal approach [128-131] and other solution processing methods.[132-136] Until now, a majority of high efficiency kesterite solar cells were fabricated by hydrazine-solution process CZTSSe.[20, 118] However, the highly toxic and flammable nature of hydrazine restrains the commercialization using this method. Recent reports on non-hydrazine precursor solution methods have shown rapid progress in device performance.

Zeng et al. have achieved 5.1% efficiency on CZTSSe solar cells by spray pyrolysis of an aqueous precursor solution.[132] Ki and Hillhouse have first demonstrated solution process based on dimethyl sulfoxide (DMSO) solution followed by selenization.[137] Followed by Schnabel et al. and Xin et al., who have also prepared CZTSSe absorber using DMSO as the solvent, demonstrating device efficiency of 7.5% and 8.3% respectively although carbon-rich fine-grain layers were observed at the Mo/CZTSSe interface.[133, 138] Recently, Li-doped CZTSSe with DMSO-based solution processing also shown a clean back interface without carbon-rich fine grain layers, with significant improved PCE of 11.8%.[139] Besides DMSO, 2-methoxyethanol was also used as the solvent for solution-processing of Cu_2ZnSnS_4 (CZTS) absorber, without the carbon-rich fine-grain layers being observed at CZTS/Mo interface.[134, 140] Su et al. have reported the fabrication of Na-doped Cu_2ZnSnS_4 (CZTS) solar cells with an efficiency of 5.1%,[86] indicating that 2-methoxyethanol is a suitable solvent to prepare high efficiency CZTSSe solar cells with an electronically clean interface.

In this chapter, facile solution processing method using 2-methoxyethanol to fabricate CZTSSe absorber layers was reported and device efficiency of 6.0% was achieved. Further improvement with efficiency beyond 8% was demonstrated by 0.5 mol% antimony (Sb) doping in the precursor solution. Further doping beyond 0.5 mol% results in larger grain size and lower series resistance (R_{SL}), but the open-circuit voltage (V_{OC}) was lowered. Photoluminescence was done to highlight and provide further understanding on the effect of Sb and its doping concentration.

6.2 Sb-Doped $Cu_2ZnSn(S,Se)_4$ Solar Cells Fabricated by Non-Toxic Solution Processing

The CZTSSe and devices in this chapter were fabricated in-house in Energy Research

Institute of NTU (ERI@N). The precursor solution was prepared by dissolving $CuCl_2$ (0.38 M), $ZnCl_2$ (0.28 M), and $SnCl_2$ (0.20 M) in 2-methoxyethanol. Note that $ZnCl_2$ is hydroscopic and thus the actual concentration may be less. After vigorous stirring, a white-coloured precipitates was formed in the solution. Chemical reactions in such a mixture have been reported previously. When mixing in a solution, Cu^{2+} ions are reduced by Sn^{2+} to form Cu^{1+} and Sn^{4+} (Reaction 6.1).[133] Thiourea (1.6 M) was then added into the solution. After stirring for several minutes, a clear pale-yellow-coloured solution was produced. The dissolution of the white-coloured precipitates is due to the formation of metal complexes via the coordination of $S{=}C(NH_2)_2$ with metal atoms through the metal-sulfur bond.[133]

$$2Cu^{2+} + Sn^{2+} \rightarrow 2Cu^{1+} + Sn^{4+} \tag{6.1}$$

For Sb doping, additional $SbCl_3$ was dissolved into the precursor solution. The doping percentages (0.5 mol%, 1.0 mol% and 2.0 mol%) were calculated based on the concentration of Cu ion and $SbCl_3$ (1.9 mM, 3.8 mM and 7.6 mM) was added accordingly.

Precursor films were fabricated by spin coating the precursor solutions onto Mo-coated soda-lime-glass substrate (size of ~1.5×4 cm^2) at 3000 revolution-per-minute for 10 s, followed by annealing at 260 °C in air for 2 minutes. The film deposition process was repeated 10 times to achieve the required thickness (1 µm). The precursor films were selenized in Ar/Se atmosphere at 520 °C for 12 minutes in a quartz tube contained in a graphite box. Cadmium sulphide (CdS) buffer layer with thickness of 50 nm was deposited on top of the selenized CZTSSe absorbers by chemical bath deposition. The device fabrication was finished by sputtering a 500 nm i-ZnO/aluminium zinc oxide (AZO) transparent conducting layer followed by evaporation of Ni/Al grid electrodes (28 devices per substrate). No antireflection coating (ARC) was coated on the finished devices. The final device area was defined by mechanical scribing, with total and active cell area of 0.16 and 0.12 cm^2 respectively.

6.3 Physical Characteristics of Sb-Doped $Cu_2ZnSn(S,Se)_4$

The XRD profiles in **Figure 6-1** show nearly amorphous phase in the as-deposited film. The two peaks at 40.5^0 and 73.6^0 are assigned to the Mo back-contact according to JCPDS 03-065-7442. The two broad peaks at 28.6^0 and 47.4^0 correspond to the two main peaks of kesterite Cu_2ZnSnS_4 (JCPDS 00-02-0575). This means that kesterite CZTS phase is formed after annealing at 260 ^{0}C in air, although the crystallinity is low. After selenization, sharp distinct peaks at 27.4^0, 45.6^0 and 54.1^0 were observed, indicating a greatly improved crystallinity. These peaks fall in between the characteristics peaks of kesterite Cu_2ZnSnS_4 (JCPDS 00-02-0575) and $Cu_2ZnSnSe_4$ (JCPDS 00-052-0868). The shift of the XRD peaks towards lower 2θ values after selenization is due to the replacement of sulphur by selenium which enlarges the crystal unit cell.[132]

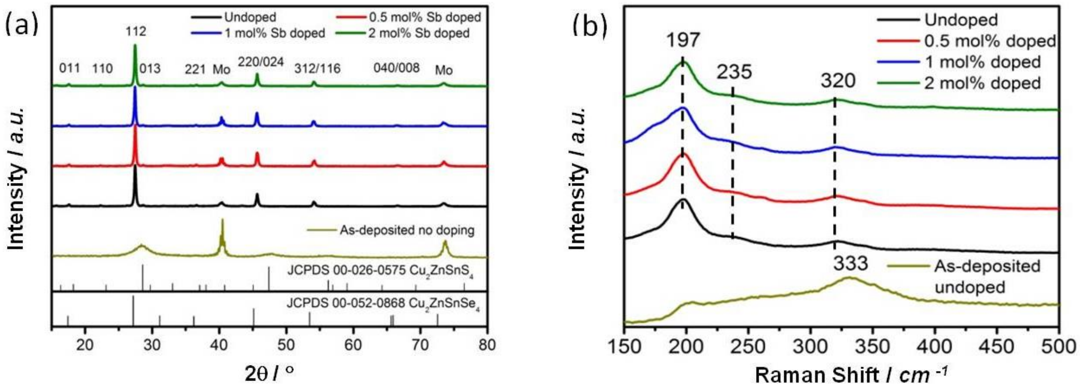

Figure 6-1. (a) XRD and (b) Raman profiles of the as-deposited undoped Cu_2ZnSnS_4 precursor film and the annealed $Cu_2ZnSn(S, Se)_4$ absorber layers with undoped, 0.5,

1.0 and 2.0 mol% of Sb doping. All absorber layers are deposited onto Mo/SLG substrates. The reference JCPDS XRD pattern for Cu_2ZnSnS_4 and $Cu_2ZnSnSe_4$ are plotted at the bottom of (a).

The samples were further evaluated by Raman spectroscopy. The result for the as-deposited film in **Figure 6-1(b)** shows a broad peak at 333 cm^{-1}, corresponding to the A_1 vibration mode of the S atoms in amorphous CZTS.[141] After selenization, partial replacement of S by Se atoms results in the shifting of major A_1 peaks to the lower wavenumbers at 175, 197 and 235 cm^{-1} due to reduced vibration frequency resulted from heavier Se atoms. In addition, the Raman profile of CZTSSe with intermediate S/(S+Se) ratio exhibits a bimodal behaviour and thus 333 cm^{-1} peak is shifted slightly towards 320 cm^{-1}.[107] No other peak was identified from Raman spectra down to the depth where the laser could penetrate. However, secondary phases cannot be ruled out as $Cu_2SnS(Se)_3$ and ZnS(Se) have similar XRD and Raman peak positions with CZTSSe.

The compositional profiling by energy-dispersive X-ray spectroscopy (EDX) shows an average Cu/(Zn+Sn) ratio of 0.84 and Zn/Sn ratio of 1.05, close to the reported optimum range for high efficiency devices.[128] Note that the atypical decrease in Zn/Sn ratio after selenization could be due to the over-calculated concentration of the hydroscopic $ZnCl_2$ in the precursor solution, as mentioned above. The cross sectional scanning electron microscopy (SEM) images of fully fabricated CZTSSe solar cells with different Sb doping concentrations are shown in **Figure 6-2**. The film thicknesses of the CZTSSe absorber layers are all close to 1 µm. Slight difference in the thicknesses is expected for the spin coating processes. It should be noted that carbon-rich fine-grain layer was not observed in all selenized CZTSSe absorbers, even though the selenization temperature (520 °C) was lower compared to previous reports.[134, 140] One reason could be due to the low boiling point (125°C) of 2-methoxyethanol compared to DMSO (189 °C). This highlights the benefit of using 2-methoxyethanol in comparison to DMSO to achieve an electronically clean interface.

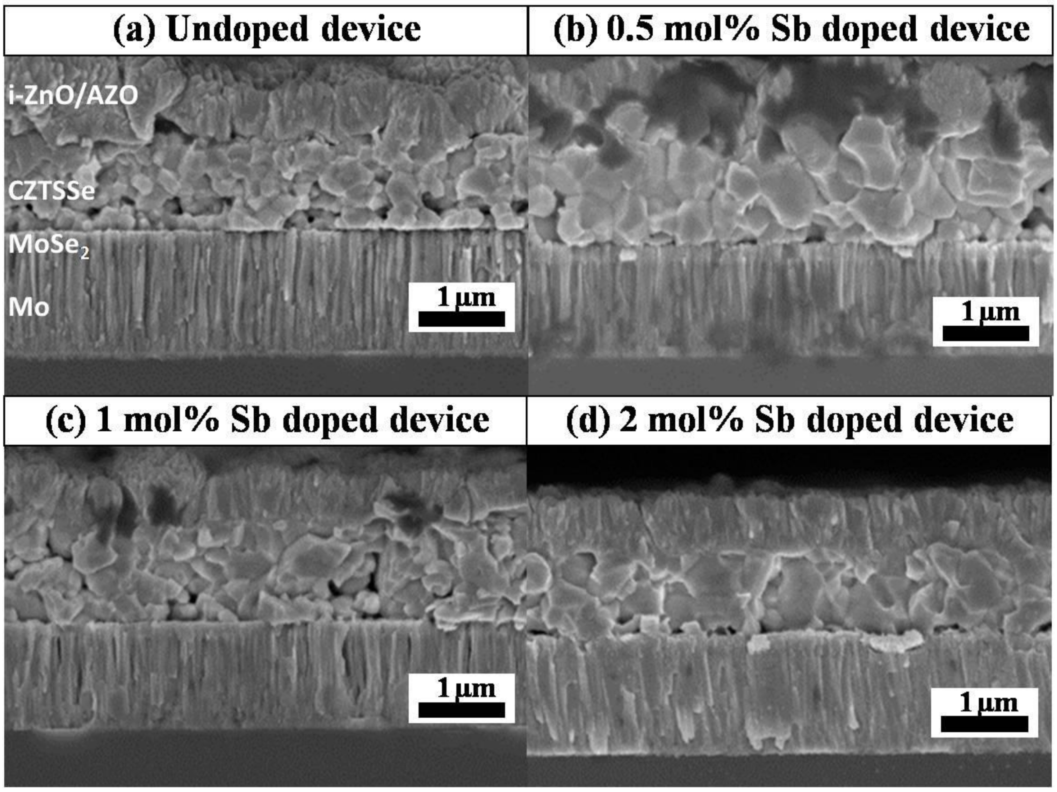

Figure 6-2. Cross sectional SEM images of (a) undoped, (b) 0.5 mol% Sb doped, (c) 1 mol% Sb doped, d) 2 mol% Sb doped CZTSSe devices.

Enhanced grain growth in the CZTSSe absorber was observed with Sb doping, with larger grain size when doping concentration was increased. The undoped CZTSSe in **Figure 6-2(a)** features a grain size of 100-200 nm. When doped with 0.5 mol% Sb, the grain size was significantly enlarged to around 500 nm (**Figure 6-2(b)**). Subsequent increase to 1.0 mol% Sb (**Figure 6-2(c)**) did not result in obvious change in grain size, but further increase to 2.0 mol% Sb (**Figure 6-2(d)**) result in grain size close to 1 µm, which is comparable with the absorber's thickness. Due to the minute amount of Sb in the absorber film, EDX was not able to probe the quantitative amount of Sb.

However, the presence of Sb inside the absorber layer was confirmed by secondary ion mass spectrometry (SIMS), as shown in **Figure 6-3**. The figure represents the SIMS depth profile for the major elements present in the absorber film of 0.5 mol% Sb-doped CZTSSe. Higher doping concentrations in the precursor solutions are expected to yield higher Sb-content in the final film, as suggested by the increased grain size.

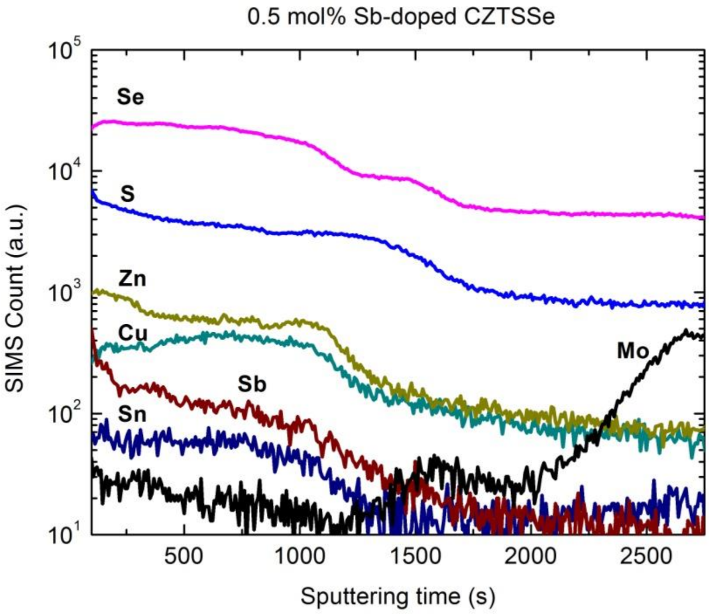

Figure 6-3. SIMS depth profile for the major elements presence in the absorber film with 0.5 mol% Sb doping.

6.4 Electrical Characteristics of Sb-Doped $Cu_2ZnSn(S,Se)_4$

Figure 6-4 shows the raw EQE data (solid line) and differentiated d(EQE)/dλ curve (dash line) for the extraction of band gap (E_g). The noisy signal at 750-900 nm of the spectrum is due to the spiky spectrum of the Xenon-light source. Note that the sharp peaks in d(EQE)/dλ at higher wavelength are due to equipment artifact, which all fall at 1100 nm. Therefore, E_g of the absorbers were extracted from the peak indicated by the arrow in **Figure 6-4 (a)**. The E_g of all the CZTSSe were found to be similar, with E_g = 1.15 eV for undoped and 1.0 mol% doped CZTSSe, and E_g = 1.16 eV for the 0.5 mol% and 2.0 mol% doped CZTSSe. This further verified that the sample processing, especially selenization conditions, were similar for all the doped and undoped samples.

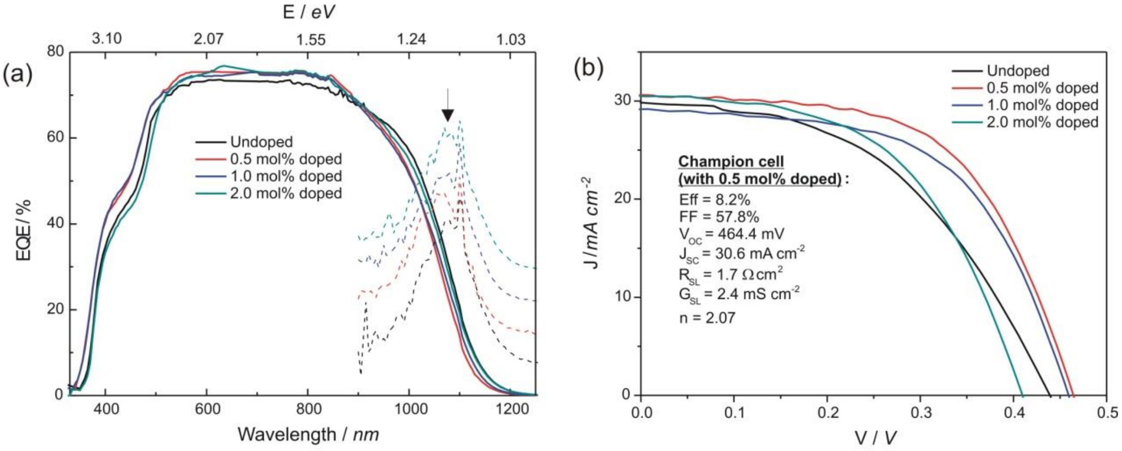

Figure 6-4. (a) External quantum efficiency (EQE) with band gap extracted from the peak of d(EQE)/dλ (see arrow), (b) Current density-voltage (J-V) curve of the best-performance device from each doping condition, with the device parameters of the best efficiency (0.5 mol% doped) listed. Note that the sharp peak of d(EQE)/dλ which all fall at 1100 nm is due to equipment artifacts.

CZTSSe solar cells from each doping condition were tested under simulated AM1.5 sunlight. The current density-voltage (J-V) curves of the best devices in each doping condition are shown in **Figure 6-4 (b)**, with the device parameters listed for the champion 0.5 mol% Sb-doped CZTSSe solar cell. The champion device in this study (with 0.5 mol% Sb doping) has an efficiency of 8.2% (active area 0.12 cm^2), comparable to high efficiency devices fabricated by non-hydrazine solution methods reported recently.[133-136] The average values and standard deviations of the device parameters from 5 devices in each doping condition are tabulated in **Table 6-1**.

Table 6-1. Summary of the current density-voltage (J-V) characteristics of CZTSSe solar cells with different concentration of Sb dopants. The average values and standard deviation of the device parameters are extracted from five devices in each group.

Sb conc. [mol%]	**Voc** [mV]	**Jsc** [mA/cm^2]	**FF** [%]	**Eff** [%]	**$E_g/q - V_{oc}$** [mV]	**R_{SL}** [Ω cm^2]	**n**
0.0	439.1 ± 4.3	28.1 ± 1.2	47.2 ± 1.0	5.8 ± 0.2	710.9 ± 4.3	2.8 ± 0.3	2.7 ± 0.4
0.5	463.9 ± 3.2	29.3 ± 1.2	58.2 ± 1.1	7.9 ± 0.2	696.1 ± 3.2	1.7 ± 0.2	2.1 ± 0.1
1.0	458.1 ± 1.8	29.0 ± 0.8	56.6 ± 0.8	7.5 ± 0.2	691.9 ± 1.8	1.5 ± 0.2	2.4 ± 0.1
2.0	406.9 ± 5.9	30.5 ± 1.5	53.4 ± 1.5	6.6 ± 0.1	753.1 ± 5.9	1.1 ± 0.2	2.8 ± 0.2

Taking the standard deviations into account, the short-circuit current densities (J_{SC}) stay almost constant regardless of the doping concentration, in consistent with similar band gaps extracted. However, when doped with 0.5 mol% Sb, the open-circuit voltage (V_{OC}) increases from 439.1 ± 4.3 to 463.9 ± 3.2 mV and the ideality factor (n) improves from 2.7 ± 0.4 to 2.1 ± 0.1. The V_{OC} increment of ~25 mV far exceeded the variation of bandgap (E_g/q of ~10 mV). Consistent with the enhanced grain growth, the series resistance R_{SL} also improves with Sb concentration, as shown in **Table 6-1**. With increased V_{OC}, improved n and R_{SL}, fill factor (FF) is also expected to increase due to the well-known empirical relationship (Equation 3.7 (a)-(c)). In fact, the calculated average FF for undoped, 0.5 mol%, 1.0 mol%, 2.0 mol% doped devices (calculated FF: 48.4%, 59.2%, 57.2%, 52.1% respectively) are in close agreement with the experimental average FF shown in **Table 6-1**. Although further Sb doping beyond 0.5 mol% increases the grain size and reduces the R_{SL} substantially, the V_{OC} decreases unexpectedly. Therefore, photoluminescence was done to investigate the V_{OC} dependence on the Sb concentration to understand the doping effect.

6.5 Optical Characteristics of Sb-Doped $Cu_2ZnSn(S,Se)_4$

Excitation-power dependent PL at 7 K and temperature-dependent PL with maximum laser excitation intensity (22.53 W.cm^{-2}) were performed on the CZTSSe bare absorbers (sisters' samples) and discussed in the following. **Figure 6-5** shows the excitation-power dependent PL spectra of the undoped CZTSSe and three other CZTSSe with different Sb doping concentration, measured at 7 K. As discussed in **Section 4.2.1**, the PL peak at the lower energy of ~1.05 eV (**Figure 6-5**) was attributed to quasi-donor-acceptor pair (QDAP) recombination with longer recombination lifetime due to carrier localization, whereas the high energy (> 1.10 eV) 'shoulder' emission was attributed to band-related recombination with shorter lifetime (< 5 ns) as carrier become more delocalized.[86] The QDAP recombination results from the clustering of donor-acceptor pairs (DAP) when the defect density is high. The interaction of DAP deviates from the original DAP model (which has no interaction between defect pairs), and thus is termed "quasi". More details about QDAP recombination can be found in **Section 4.2.1** and the literature.[86]

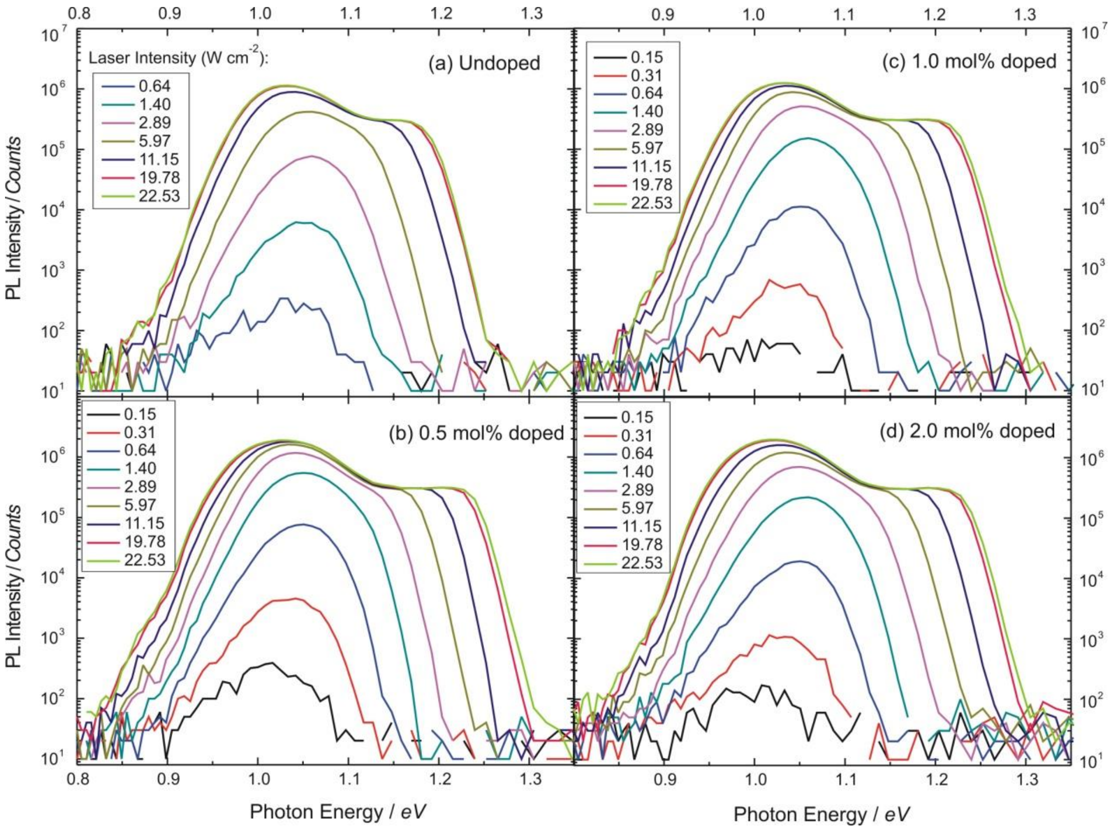

Figure 6-5. Power-dependent photoluminescence for (a) undoped, (b) 0.5 mol%, (c) 1.0 mol%, (d) 2.0 mol% Sb doped $Cu_2ZnSn(S,Se)_4$ thin films, measured at 7 K. (b)-(d)

shows significant extension of band-related emission (E > 1.25 eV) due to passivation of non-radiative states by Sb dopants.

The PL of the undoped CZTSSe thin film (**Figure 6-5 (a)**) is dominated by QDAP recombination when the excitation intensities are low. As the excitation intensity increases up to a *threshold* intensity of 5.97 W.cm^{-2}, the trap states (*which includes the radiative QDAP and non-radiative states*) within the band gap become fully occupied and additional photo-excited carriers *start* to occupy the band-related states at higher energy levels, as shown by the appearance of the shoulder emission. The *threshold laser intensity* of 5.97 W.cm^{-2} corresponds to a photon density per pulse of 1.07×10^{15} cm^{-2} for 532 nm laser wavelength and 15 kHz repetition rate. Assuming all the photons were absorbed within a depth of 100 nm (with absorption coefficient of 1×10^{5} cm^{-1})[87] and all the electron-hole pairs generated are captured by the trap states within the band gap, the *upper bound* trap density (N_t) within the band gap is estimated to be *1.07×10^{20} cm^{-3} for the undoped CZTSSe*. Note that the estimated N_t here is similar to the N_t estimated for the hydrazine-solution processed CZTSSe, as shown in **Table 4-3**. This indicates that the CZTSSe synthesized by non-toxic solution processing has equivalent intrinsic crystal quality which is promising. More importantly, the shoulder emission in 0.5 mol% Sb-doped CZTSSe (**Figure 6-5 (b)**) starts to appear at a lower threshold intensity of 2.89 W cm^{-2}, which corresponds to N_t of *5.16×10^{19} cm^{-3}* with similar assumptions made. This indicates that the *trap density within the band gap is significantly reduced* by approximately half as compared to the undoped sample.

The reduction in trap density by Sb doping is further verified by the PL spectra using maximum laser intensity (22.53 W cm^{-2}), as the shoulder emission extends toward higher photon energy beyond 1.25 eV for 0.5 mol% Sb-doped CZTSSe (**Figure

6-5 (b)). The longer extension of the shoulder emission is due to lower trap density within the band gap such that less amount of photo-excited carriers can occupy all the trap states and the remaining photo-excited carriers can then occupy the higher energy band-tail or band states. However, further doping beyond 0.5 mol% does not reduce the trap density as the threshold laser intensities for shoulder emissions in 1.0 mol% and 2.0 mol% Sb-doped CZTSSe are similar (2.89 W cm^{-2}), and the shoulder emissions do not extend further at maximum laser intensity (**Figure 6-5 (c)-(d)**), compared to the 0.5 mol% doped CZTSSe. A summary of the total trap density of the samples are given in **Table 6-2** below.

Table 6-2. Calculated density of quasi donor-acceptor pairs (QDAP) from the magnitude of blueshift in power-dependent photoluminescence measurement, assuming a dielectric constant of 7.94 [11, 87] for CZTSSe with band gap of 1.16 eV.

Sb conc. [mol%]	**Peak position** [eV]		**DAP Separation Distance** [nm]	**QDAP Density** [cm^{-3}]	**Upper Bound N_t** [cm^{-3}]	**Upper Bound γ** [meV]
	at lowest possible laser intensity	at saturated blueshifted peak				
0.0	1.033	1.059	6.95	**7.1×10^{17}**	**1.1×10^{20}**	**110-119**
0.5	1.018	1.051	5.47	**1.5×10^{18}**	**5.2×10^{19}**	**82-89**
1.0	1.009	1.059	3.62	5.0×10^{18}	5.2×10^{19}	82-89
2.0	0.998	1.055	3.26	6.9×10^{18}	5.2×10^{19}	82-89

With estimated *upper bound* of N_t, the *upper bound* for the depth of fluctuating potential (γ) induced by non-uniform distributed charged defects in highly doped CZTSSe can be calculated from **Equation (4.7)**. Assuming a dielectric constant of 7.94,[11, 87] electron effective mass of 0.07 and hole effective mass of 0.09-0.33 for our CZTSSe,[31] *the upper bound γ for the undoped CZTSSe* is found to be *110- 119 meV*, whereas the *upper bound γ for the 0.5 mol% Sb-doped CZTSSe* is found to be *82- 89 meV*. The *reduction of γ in CZTSSe with Sb-doping* is an important proof-of-concept that this intrinsic property of highly doped semiconductor can be tuned by extrinsic doping. Furthermore, the reduction in γ (28- 30 meV) is also consistent with the increment of V_{OC} of ~ 25 meV from undoped to 0.5 mol% Sb-doped CZTSSe (**Table 6-1**). The slight difference could be due to the different effective masses in our CZTSSe with mixed S-Se (expecting a lower hole effective masses and thus a slightly lower γ).[31] This highlights the direct impact of potential fluctuation on the V_{OC}, and serves as an important hint that the intrinsic property of the absorber layer should be highly focused for further improvement of CZTSSe solar cell.

The trap states discussed so far include both radiative (QDAP) and non-radiative recombination. As described in **Section 4.2.1** and based on **Equation (4.2)**, the *radiative* QDAP density can be estimated from the magnitude of the saturated blue-shift of the QDAP PL peaks in the power-dependent PL measurement. At the lowest excitation intensity, the charged donors and acceptors are far apart and the Coulombic interaction between them is negligible. At high excitation intensity (just before shoulder emission start to appear), all the donor and acceptor states are occupied. Here, the radiative recombination gives rise to the maximum blue-shifted PL peak as the separation distance between the charged donors and acceptors is minimum. Therefore, the saturation of the blue-shift magnitude in the QDAP PL peak is equal to the last Coulombic term in Equation (4.2), and thus the average spacing (r) of the radiative defects and the QDAP density (N_D) can be estimated by assuming $r = (4\pi N_D/3)^{-1/3}$.[86]

Table 6-2 lists the estimated QDAP densities of all four samples. The QDAP density increases from *7.1 × 10^{17} cm^{-3} for the undoped CZTSSe* to *1.5 × 10^{18} cm^{-3} for the 0.5 mol% Sb-doped CZTSSe*. Note that the estimated N_t of 0.5 mol% doped CZTSSe is much higher than the radiative QDAP density (**Table 6-2**). This is due to the conservative estimation on the *upper bound* trap density based on the assumption that all excitation photons are absorbed by the film, and non-radiative recombination is likely to occurs which are not reflected in the QDAP emission.

Even though the radiative QDAP density in 0.5 mol% Sb-doped CZTSSe ***increases***, the total trap density (*which includes the radiative QDAP and non-radiative states*) within the band gap ***decreases*** in the 0.5 mol% doped CZTSSe, compared to the undoped CZTSSe (**Table 6-2**). This suggests that the non-radiative centers is significantly reduced or passivated by Sb-doping. The suppression of non-radiative centers by Sb doping is further verified in temperature-dependent PL, as shown in **Figure 6-6** below.

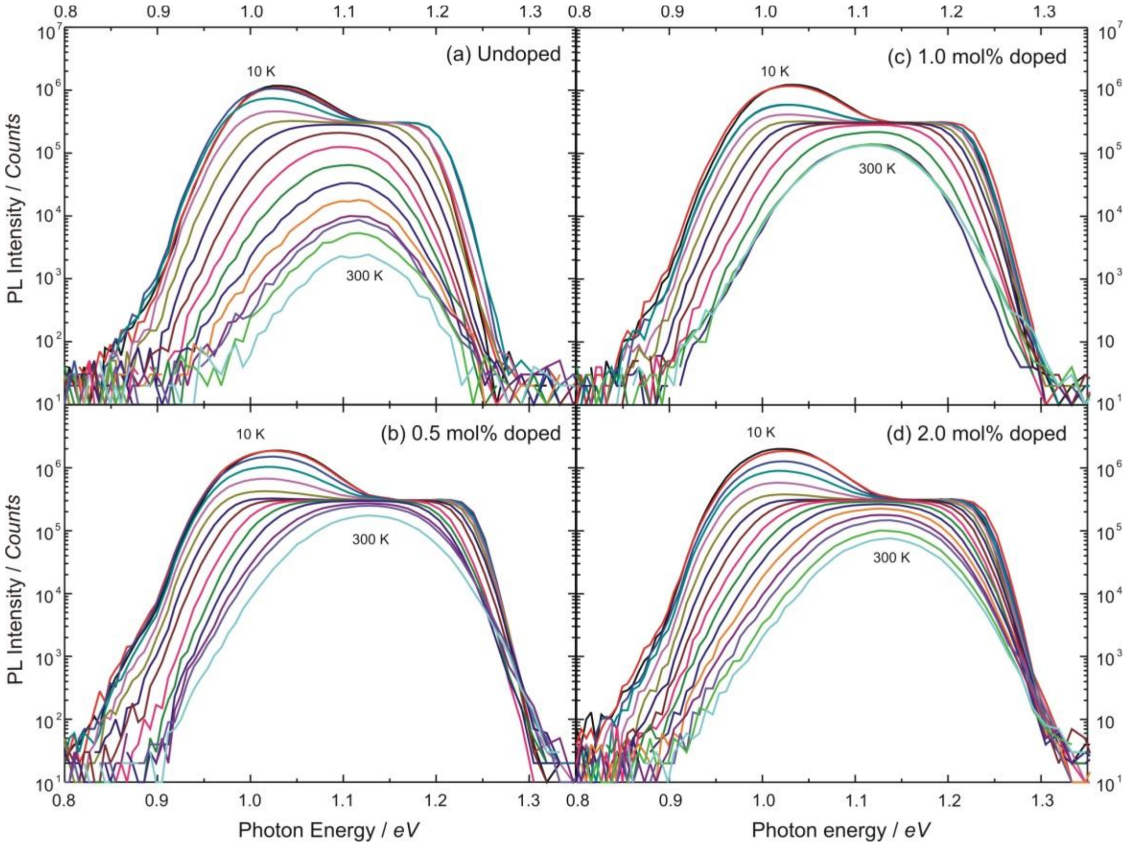

Figure 6-6. Temperature-dependent photoluminescence (PL) for (a) undoped, (b) 0.5 mol%, (c) 1.0 mol%, (d) 2.0 mol% Sb-doped $Cu_2ZnSn(S,Se)_4$ solar cells. Progressive decay of PL in (a) indicates the increasing non-radiative relaxation with temperature. Passivation of non-radiative states with 0.5 mol% Sb dopants slows the decay and

achieve higher PL intensity at room temperature. Further doping may results in non-radiative Auger recombination which reduces the PL intensity at high temperature.[142]

The decay of PL intensity with temperature in the undoped CZTSSe (**Figure 6-6 (a)**) is faster than the decay in the 0.5 mol% Sb-doped CZTSSe (**Figure 6-6 (b)**). In addition, the PL intensity at 300 K of the 0.5 mol% Sb-doped CZTSSe is two-orders of magnitude stronger compared to the undoped CZTSSe. As the photo-excited carriers are quenched by two competing channels- radiative or non-radiative recombination, the slow-decaying radiative PL intensity and high PL intensity at 300 K clearly indicate that the non-radiative centers are less efficient in quenching the photo-excited carriers in the 0.5 mol% Sb-doped CZTSSe. The slight quenching of PL with increasing temperature could be due to lattice vibration (phonon). Similar effect of suppressing the non-radiative recombination was also observed previously with Na doping in CZTSSe.[84, 143]

The mechanism for Sb suppressing the non-radiative recombination channel is not exactly clear at the moment. One possible mechanism is the change of crystal orientation which leads to less detrimental grain boundaries (with less non-radiative traps). Such mechanism have been reported in CIGS, where the high-efficiency CIGS solar cell with less non-radiative recombination centers has a dominant (220) crystal orientation compared to the usual (112) crystal orientation.[144] Furthermore, Sb-doping has been shown to effectively increase the ratio of (220)/(112) crystal orientation while improving the solar cell efficiency of CIGS.[145] As the kesterite CZTSSe has similar tetragonal crystal structure as CIGS, similar passivation mechanism of non-radiative channels could be hold true. Indeed, a further analysis on the XRD peaks indicates an increasing ratio of (220)/(112) crystal orientation as Sb-amount increases.

Table 6-3. Normalized ratio of XRD peak intensity. Each peak is normalized to its respective Mo peak intensity.

	Undoped	0.5 mol%	1 mol%	2 mol%
(220)/(112)	0.304	0.331	0.337	0.338
(312)/(112)	0.115	0.133	0.127	0.120

Although the non-radiative centers are efficiently suppressed, it was noted that the V_{OC} deficit was still high and the ideality factor (*n*) was still larger than *2*. There could be several reasons to account for this: (1) Sb does not completely remove all non-radiative centers, it may only passivate the non-radiative centers at specific location, e.g. grain boundaries; (2) non-radiative centers are not the sole culprit for large V_{OC} deficit, other factors such as severe potential fluctuation induced by high charged defect density have also been reported to account for the V_{OC} deficit;[26] (3) interfacial recombination could be severe and need more investigation.

Table 6-1 shows that further doping with Sb beyond 0.5 mol% reduces V_{OC} and FF. The cause of deteriorating V_{OC} can be explained experimentally as the PL intensities decay more quickly with temperature when the doping concentration increases beyond 0.5 mol% [faster decay rate in the 2.0 mol% doped CZTSSe (**Figure 6-6 (d)**) is observed compared to the 1.0 mol% doped CZTSSe (**Figure 6-6 (c)**)]. This suggests that further doping beyond 0.5 mol% will result in the creation of new defects which is reflected in the higher QDAP density in 1.0 mol% and 2.0 mol% Sb doped CZTSSe (**Table 6-2**). This is further supported by the fact that the increment in QDAP density from 0.5 mol% to 1.0 mol% doped CZTSSe ($3.5 \times 10^{18}\ cm^{-3}$) is higher than the increment from the undoped to 0.5 mol% doped CZTSSe ($7.9 \times 10^{17}\ cm^{-3}$). A high concentration of defects may also cause non-radiative Auger recombination which decreases the PL intensity at high temperature.[142] Finally, this observation may also suggest that a lower Sb concentration which can efficiently passivate the non-radiative states without creating new defect may yield better device performance through enhanced V_{OC}.

6.6 Conclusion

In conclusion, to aim towards large scale industrialization of CZTSSe technology, a greener synthesis method for CZTSSe layer was demonstrated using non-toxic and non-hazardous solution processing technique. Based on previous understanding on the intrinsic limitation on CZTSSe solar cell (as described in CHAPTER 4), extrinsic doping with Sb was attempted to alter the intrinsic property of the semiconductor, in particular to reduce the depth of potential fluctuation (γ). A baseline efficiency of 6.0 % was achieved in the undoped CZTSSe solar cell, whereas the champion efficiency of 8.2 % was achieved with 0.5 mol% Sb-doping.

The XRD diffraction and Raman phonon scattering do not vary between the undoped and doped CZTSSe, but the grain growth is significantly enhanced with higher Sb-concentration. This results in reduced series resistance (R_{SL}) and thus increases the short-circuit current density (J_{SC}) as Sb-concentration increases. However, maximum open-circuit voltage (V_{OC}) was achieved with 0.5 mol% Sb doping, and further doping reduces the V_{OC}. To understand the doping mechanism in depth, the dependence of V_{OC} on the Sb-concentration was investigated with power- and temperature-dependent photoluminescence (PL).

From power-dependent PL, a direct indication of reduced trap density (N_t) by approximately half in 0.5 mol% Sb-doped CZTSSe was observed from the threshold laser intensity where the band-tail related recombination appears, as compared to the undoped CZTSSe. The reduced N_t resulted in a lower γ induced in the 0.5 mol% Sb-doped CZTSSe. More importantly, the reduction of γ (28- 30 meV) is consistent with the increment of V_{OC} (~25 mV), which serves as an important evidence that the potential fluctuation has direct impact on V_{OC}.

Specifically, N_t was reduced through passivation of non-radiative recombination centers or defects, as indicated by (1) the increased radiative quasi-donor-acceptor-pair (QDAP) density although the total defect density (N_t) decreases, and (2) the slower decay of PL intensity with increasing temperature in the 0.5 mol% Sb-doped CZTSSe. However, further Sb doping beyond 0.5 mol% will create additional defects which promote non-radiative Auger recombination, resulted in the greater increase of QDAP density and faster decay of PL intensity with increasing temperature.

As non-radiative recombination still dominates, with N_t much higher than the QDAP density, further improvement on the absorbers' quality should focus on reducing the non-radiative recombination losses, which will enhance the open-circuit voltage. The non-radiative recombination centers have to be investigated in more details, e.g. the type (certain kind of defects, Auger quenching, phonons etc.), location (grain boundary, grain bulk etc.) and mechanisms of these non-radiative recombination centers, such that the passivation could be achieved in more effective ways.

CHAPTER 7 Conclusions and Future Work

7.1 Conclusions

In summary, a series of high-performance full-range bandgap (E_g = 1.0 - 1.5 eV) $Cu_2ZnSn(S,Se)_4$ (CZTSSe) solar cells were studied by electrical, optical and physical characterizations to understand the fundamental limitations of CZTSSe thin film technology. Compared to Si and other well-established thin film solar cells, open-circuit voltage deficit ($V_{OC,def}$, defined as E_g/q - V_{OC}) is generally observed in CZTSSe solar cells. In addition, the $V_{OC,def}$ widens as the bandgap [or S/(S+Se) ratio] of CZTSSe increases. Currently, $V_{OC,def}$ poses the biggest hurdle for CZTSSe technology.

In the case of high bandgap CZTSSe solar cells with high S/(S+Se) ratio, low short-circuit current density (J_{SC}) are also observed when compared to the Shockley-Queisser limit J_{SC} (SQ-J_{SC}). The low J_{SC} in high bandgap CZTSSe solar cells are usually accompanied by high series resistance (R_S), which also results in low fill factor (FF). The concerted effect of high $V_{OC,def}$, low J_{SC}, high R_S and low FF resulted in lower power conversion efficiency (PCE) for high E_g CZTSSe solar cells. The two losses, $V_{OC,def}$ and $R_S \rightarrow J_{SC}$ & FF loss, are generally observed in the reported high bandgap CZTSSe solar cells.

V_{OC} Deficit

Having known the macroscopic losses in CZTSSe solar cells, the microscopic causes for these losses were investigated. The electrical properties of CZTSSe layers were investigated by AC Hall measurement and the defect properties were probed by photoluminescence study. Regardless of S/(S+Se) ratio, the carrier mobilities in CZTSSe thin films (0.4 - 1.3 cm^2/Vs) are found to be much lower than the well established CIGSSe thin film (~ 4 cm^2/Vs). The low carrier mobility is well correlated to the defect physics in explaining the high $V_{OC,def}$ observed in CZTSSe solar cells. High defect densities (QDAP density or total defect density, N_t), especially the deep defects and non-radiative defects could act as efficient traps in quenching photogenerated carriers. In addition, the average depth of the electrostatic potential fluctuation (γ) induced by the charged defects are more severe in CZTSSe due to the high N_t. The resulted fluctuating bands act as a potential barrier for carriers transport across the material. Therefore, high carrier recombination will occur which results in perturbed carrier transport. This will lower the carrier mobility and carrier diffusion length (L_d), which reduces the open-circuit voltage (V_{OC}) ultimately.

For a good solar cell, the V_{OC} is generally lower than its bandgap at room temperature. However, the extrapolation of V_{OC} at temperature of 0K from the temperature-dependent *I-V* measurement will be equivalent to its bandgap ($V_{OC,def} = 0$ at 0K).[34] This means that the thermodynamic losses on the V_{OC} at operating room temperature are inevitable. Considering a general V_{OC} losses resulted purely from thermodynamic loss is ~ *350 mV* at 300K for a good solar cell (for the best-performing Si or CIGS solar cell),[75] the fluctuating valence band and fluctuating conduction band will contribute to an additional $V_{OC,def}$ by 2γ. For comparison, the exact $V_{OC,def}$ of hydrazine solution processed *CIGSSe, CZTSSe-Z2 [low S/(S+Se)] and CZTSSe-Z6 [high S/(S+Se)]* studied here are *547, 588 and 933 mV*, respectively (**Table 3-1**). Assuming γ is independent of temperature, the overall $V_{OC,def}$ resulted from the summation of thermodynamic loss and potential fluctuation (= $350\ mV + 2\gamma/q$) were approximately *420, 570, and 630 mV* for CIGSSe, Z2 and Z6 respectively (**Table 4-3**). This suggests that there is still an unaccountable $V_{OC,def}$ of approximately *127, 17, 303 mV* for CIGSSe, Z2 and Z6 respectively.

Although the contributions from thermodynamic losses and potential fluctuation may not an accurate number, the large unaccountable $V_{OC,def}$ (> 300 mV) suggests that there are additional loss factors contributing to $V_{OC,def}$ in high bandgap CZTSSe. The additional loss factors could be related to the intrinsic quality of the CZTSSe layer (non-radiative carrier recombination and deep defect states), and/or extrinsic factors such as interfacial recombination (front CZTSSe/CdS interface and/or back CZTSSe/Mo interface) that causes device shunting. By physical characterizations, it was found that the *high S/(S+Se) ratio CZTSSe are prone to the formation of secondary phases* when grown under off-stoichiometric chemical composition. This could also be explained by the theoretical calculated phase diagram.[25]

Specifically, low band gap secondary phases are formed at the CZTSSe/CdS interface, possibly Cu_2SnS_3 with bandgap much smaller (E_g = 0.96 - 1.35 eV, depending on crystal structure)[146] than the host CZTSSe with high E_g of 1.49 eV. Cu_2SnS_3 may provide a shunting path for the photogenerated carriers, and thus explains the high shunt conductance (G_{SL}) observed in Z6 (**Table 3-1**). Besides, the low band gap secondary phases could also act as a sink for photogenerated electron-hole pairs due to the higher valence band maximum and lower conduction band minimum (compared to the host CZTSSe). This carriers' sink will potentially promote electron-hole pair recombination which results in a high reverse saturation current (J_0) and ideality factor (n_L), as shown in **Table 3-1**.

J_{SC} and FF Loss in High Bandgap CZTSSe

The main reason for J_{SC} losses in high bandgap CZTSSe solar cells is the high series resistances (R_S) dominated by the interfacial resistances. J_{SC}-V_{OC} measurement provides a clear evidence that non-ohmic back contact are developed in high S-content

CZTSSe solar cell. The non-ohmic back contact arise from two factors: (1) Formation of Schottky barrier at CZTSSe/Mo interface, as suggested by the decreasing carrier concentration for high S-content CZTSSe (**Figure** 3-6); (2) Formation of high bandgap secondary phases ($Sn(S,Se)_2$, ZnS) at the CZTSS/Mo interfaces which act as hole blocking layer for hole transport to the Mo back contact.

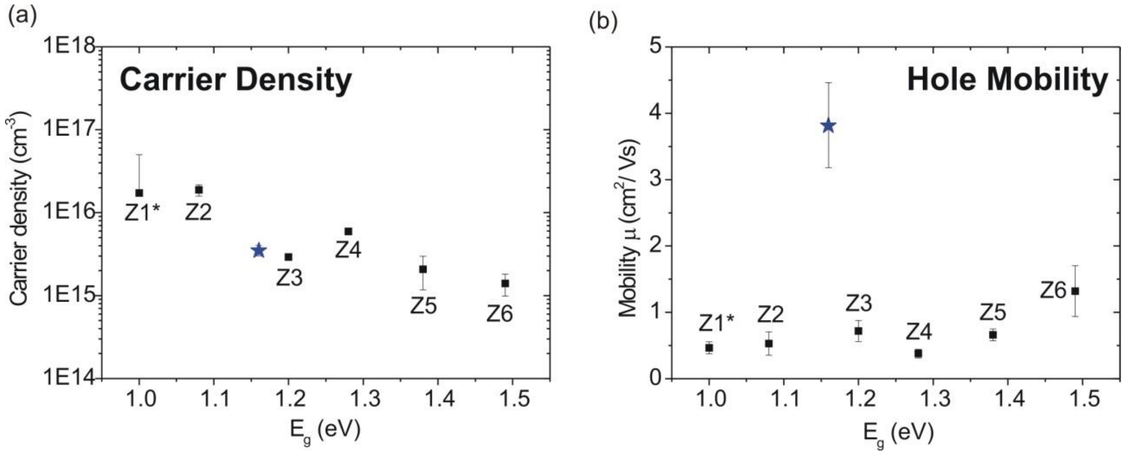

Engineering Defect Properties

It was demonstrated that the intrinsic defect properties of CZTSSe crystal could be engineered by extrinsic doping. Specifically, the total trap density was reduced by approximately half in the Sb-doped CZTSSe synthesized using non-toxic solution processing technique. The reduction in total trap density is mainly due to the passivation of non-radiative defects. As a result of the lower trap density, the induced fluctuating potential is shallower and the reduction in γ (25- 28 meV) is in close agreement with the increment in V_{OC} (~25 meV). Besides, Sb doping enhances grain growth in CZTSSe, which results in larger grain size and lower series resistance for the solar cell.

7.2 Future Work

Through the investigations on the intrinsic and extrinsic loss factors using a variety of characterization techniques, a comprehensive understanding on the limitation of CZTSSe solar cells was obtained. Based on these understanding, several directions could be pursued to further optimize the power conversion efficiency beyond 12.6 % for a warrant to commercialize this technology.

(a) *To understand the mechanism of non-radiative recombination or non-radiative defect type.* This thesis has identified non-radiative recombination losses in CZTSSe through photoluminescence study, and found that the non-radiative recombination could be reduced with Sb or Na-doping. In addition, the non-radiative recombination centers contribute significantly to the total defect density (N_t), which could affect the average depth of the fluctuating potential if these non-radiative recombination centers were charged defects. Thus, non-radiative recombination centers have direct and indirect impact on the V_{OC}. However, the origins and mechanisms of the non-radiative recombination channels remain largely unknown. It could be detrimental lattice defects located at the grain boundaries,[84] or simply Auger recombination due to large density of defect states.[142] High quality single-crystal CZTSSe could be grown to examine the possibility of non-radiative defects at grain boundaries. If certain defects act as the non-radiative recombination centers, the mechanism of recombination should be examined more carefully, such as applying group theory to examine the possibility of radiative transition. By understanding the non-radiative recombination mechanisms, a more appropriate and effective solutions could be designed to reduce the non-radiative recombination losses and increasing the $V_{OC.}$

(b) *Engineering defect properties of CZTSSe through extrinsic doping, partial or full replacement of component element.* It was demonstrated that Sb-doping can help to passivate the non-radiative defects and lower the induced fluctuating potential in CZTSSe, improving the V_{OC} eventually. However, the reduction of γ (and thus the increment in V_{OC}) is not significant. The origin of the fluctuating potential is caused by high defect density in CZTSSe. Due to the similar atomic radius and atomic number between Cu and Zn, the cross-substitution between these two elements is frequent such that [Cu_{Zn}+Zn_{Cu}] defect cluster may form. These defect clusters are self-compensated without contributing to any net carriers, and large defect density could adversely induce a deeper fluctuating potential. Therefore, Zn can be replaced with other element to reduce the dominant (and deeper) Cu_{Zn} antisite defects. As Zn-orbitals do not contribute to the density-of-states near the conduction or valence band edge, Zn is considered as inactive to the electrical properties of CZTSSe.[43] Therefore, replacement of Zn by other element may improve the defect properties and enhance the V_{OC}.

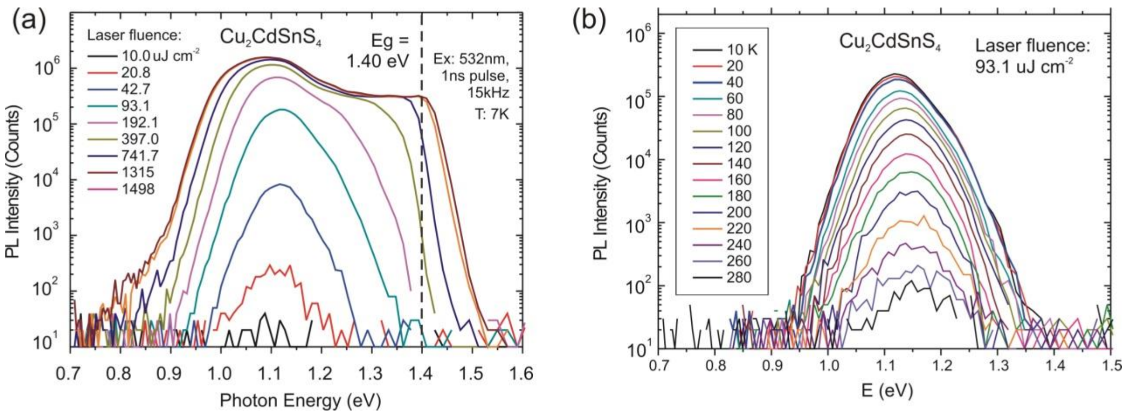

Figure 7-1. (a) Power-dependent and **(b)** temperature-dependent PL of Cu_2CdSnS_4.

An element quickly come into mind is cadmium (Cd), which is located just below Zn in the periodic table. Although Cd is toxic, Cu_2CdSnS_4 has been synthesized for a proof-of-concept that the intrinsic defect properties of the kesterite crystal could be engineered. **Figure 7-1** shows the power- and temperature-dependent photoluminescence of Cu_2CdSnS_4. Note that it is a *pure sulphide crystal*, but the shoulder emission extended to higher energy exceeding its bandgap (1.40 eV) at the maximum laser fluence. Similar shoulder emission was observed in $Cu_2ZnSnSe_4$, but not in the high S-content Cu_2ZnSnS_4 [**Figure 4-1 (c)**]. This indicates that the total defect density and the depth of fluctuating potential (γ) are reduced by replacing Zn with Cd. As a further evidence, the PL peak of the main QDAP emission is found to be more symmetric compared to the asymmetric PL peak in Cu_2ZnSnS_4 [**Figure 4-1 (c)**]. The asymmetric PL peak with slow decaying PL at the low energy side is often related to the depth fluctuating potential.[80]

Figure 7-1 (b) shows the temperature-dependent PL of Cu_2CdSnS_4 with the same laser fluence as in Cu_2ZnSnS_4. The temperature-dependent PL shows a slower decay and the PL intensity is sustained up to a higher temperature of 280K, higher compared to the case of Cu_2ZnSnS_4 [**Figure 4-5 (c)**]. This indicates that the non-radiative recombination centers are significantly reduced. However, the transition from QDAP to BB recombination was not observed, indicating that the defect level in Cu_2CdSnS_4 is still relatively deeper compared to CIGSSe [**Figure 4-5 (a)**], as supported by the activation energy extracted from the Arrhenius plot below (**Figure 7-2**). As non-radiative recombination is reduced through replacing Zn, this also suggests that the Zn-related defects could contribute to non-radiative recombination in CZTSSe.

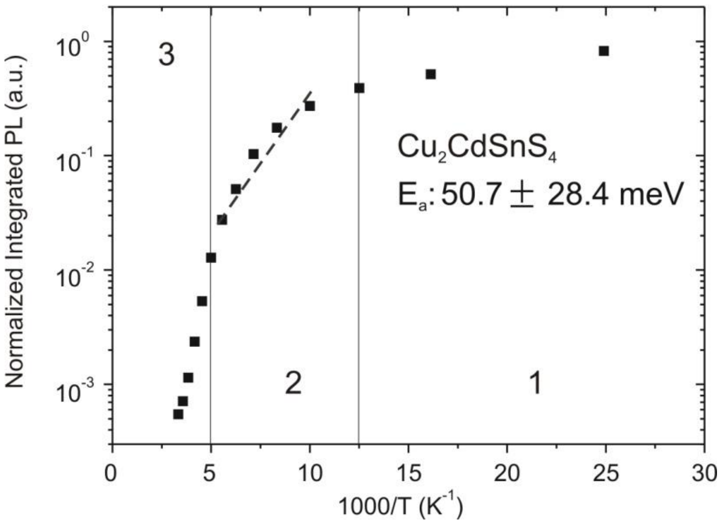

Figure 7-2. Arrhenius plot from temperature-dependent PL of Cu_2CdSnS_4. Defect activation energy E_a are extracted from region 2 (100 - 180K) and the dash line shows the Arrhenius fit.

Lastly, AC Hall measurement was done on the Cu_2CdSnS_4 thin film. **Figure 7-3** shows the post-processing of Hall signal. The results indicate that Cu_2CdSnS_4 is a *p*-type material, with resistivity (ρ) of 107.3 ± 3.3 kΩ.cm, majority carrier density of $1.6 \times 10^{14} \pm 3.9 \times 10^{13}$ cm^{-3}, and majority carrier mobility of 0.4 ± 0.1 cm^2/V s. Further element replacement, other than Cd, should be studied extensively from the perspective of theoretical DFT calculation as well as experimental works.

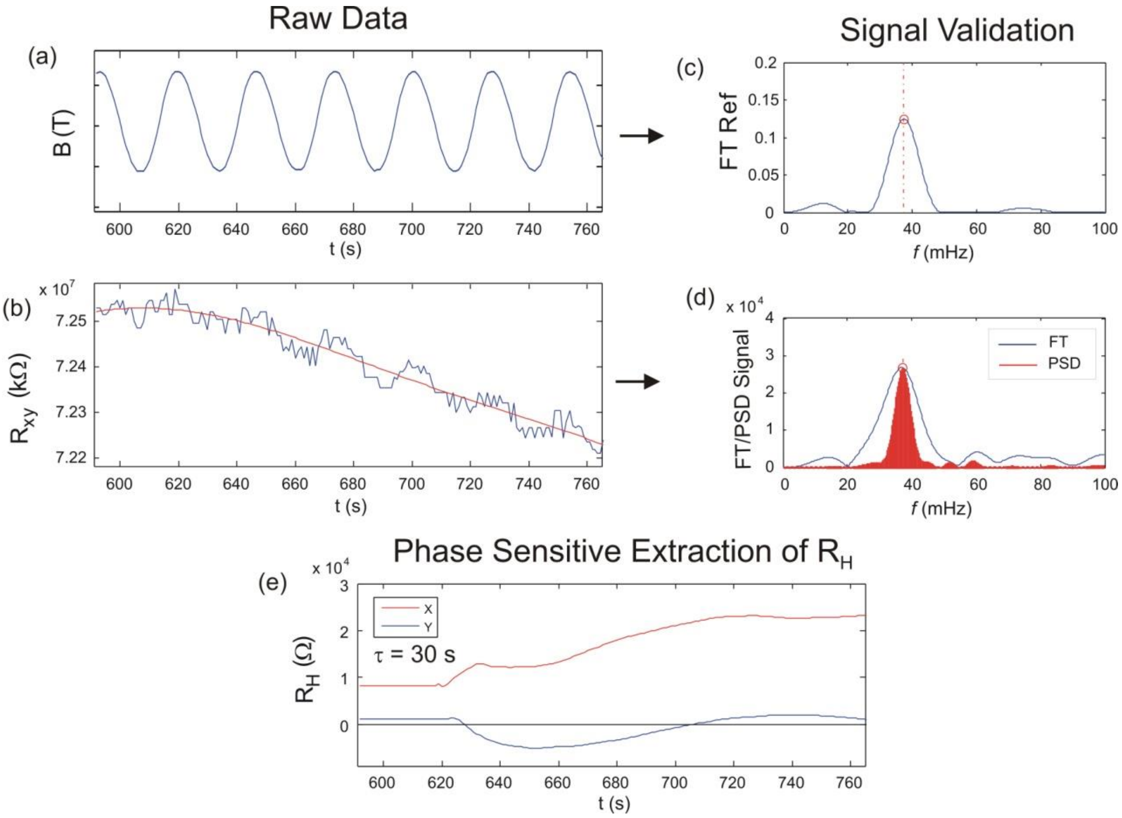

Figure 7-3. Hall signal post-processing using fast Fourier transform and phase-sensitive detection for Cu_2CdSnS_4.

(c) *To understand the thermodynamics for the formation of secondary phases and perform back contact engineering.* In CHAPTER 5, it has been shown that the unwanted secondary phases tend to form at the surface (CZTSSe/CdS interface) or the back interface (CZTSSe/Mo interface). Thermodynamic simulation should be performed to prove whether this is thermodynamically favourable. If this is the case, surface etching and back contact engineering could be performed to eliminate the unwanted secondary phases, as a way to reduce the shunt conductance (which also improve the V_{OC}) and the series resistance (which also improve the J_{SC}). Improvement in both of these parameters will result in high fill factor (FF) and improve the power conversion efficiency of CZTSSe solar cells.

Appendix A- Examples of AC Hall Effect Measurement

Below are two examples among many other successful examples for AC Hall measurement on cuprous oxide thin film and lead perovskite thin film. Both examples show the Hall signal oscillating at the same frequency as the *B*-field, validating the Hall signal. The Hall parameters are extracted as indicated below.

Cuprous Oxide (Cu_2O) Thin Film:

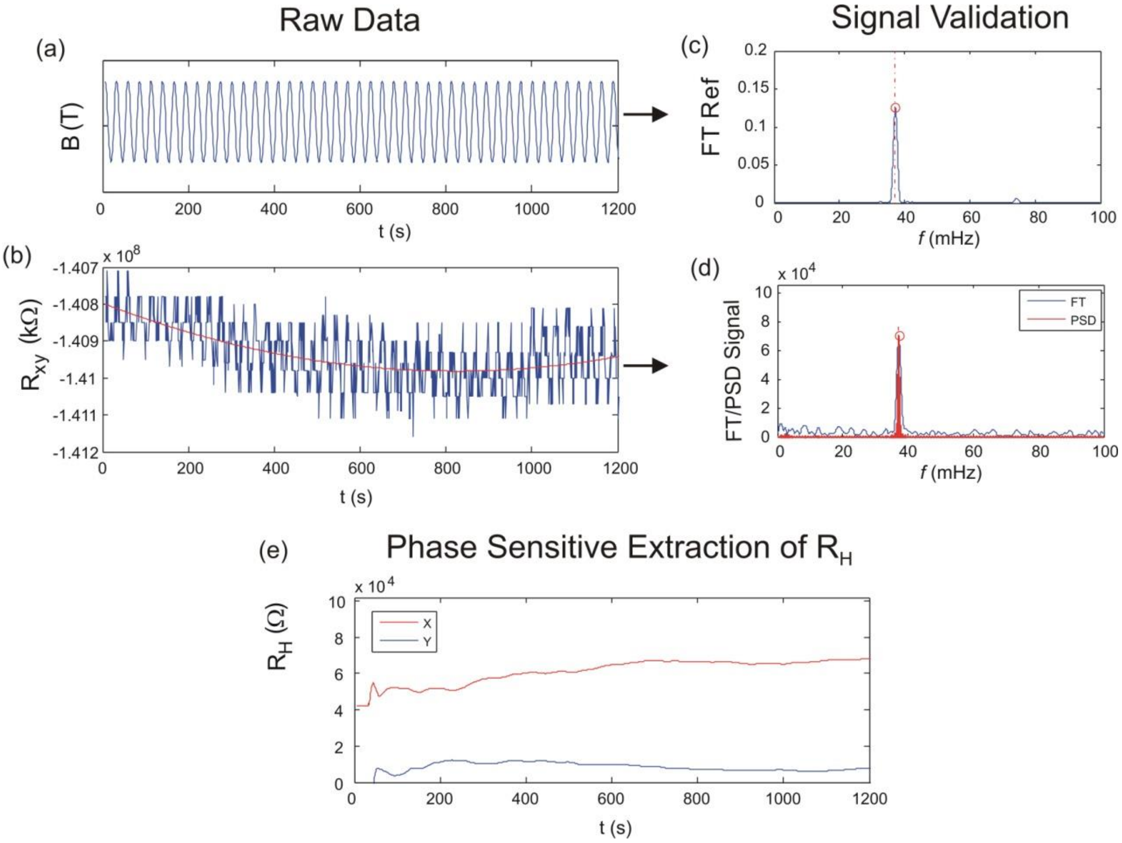

Figure A1. Hall oscillation raw data and post-analysis Hall signal.

<u>Resistivity Measurement:</u>

Sheet resistance $R_S = 8.8\times10^8 \pm 7.9\times10^4$ Ω/□,

Resistivity $\rho = 8.8\times10^4 \pm 2.6\times10^3$ Ω.cm,

<u>AC Hall Measurement:</u>

Hall resistance $R_H = 6.1\times10^4 \pm 3.1\times10^2$ Ω,

Majority carrier density $p = 8.2\times10^{13} \pm 1.06\times10^{13}$ cm^{-3},

Majority carrier mobility $\mu = 0.9 \pm 0.1$ cm^2/V s.

<u>Brief Diagnosis:</u>

Carrier mobility is similar to CZTSSe but the carrier density is much lower, which results in low bulk conductivity. Extrinsic doping can be studied to increase *p*.

Lead Perovskite ($CH_3NH_3PbI_3$) Thin Film:

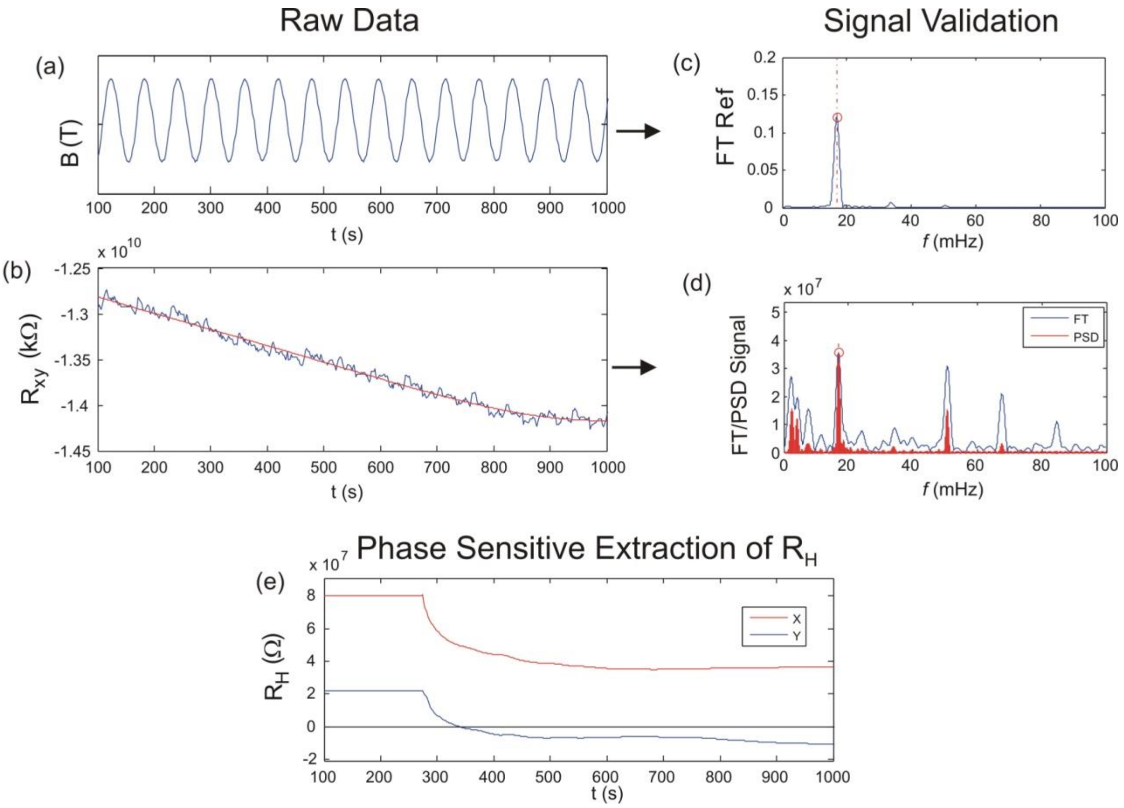

Resistivity Measurement:

Sheet resistance $R_S = 1.6\times10^{11} \pm 5.8\times10^{8}\ \Omega/\square$,

Resistivity $\rho = 3.5\times10^{6} \pm = 7.8\times10^{5}\ \Omega$.cm,

AC Hall Measurement:

Hall resistance $R_H = 3.7\times10^{7} \pm 2.5\times10^{5}\ \Omega$,

Majority carrier density $p = 6.2\times10^{11} \pm 1.6\times10^{11}$ cm^{-3},

Majority carrier mobility $\mu = 2.9 \pm 1.0$ cm^2/V s.

Brief Diagnosis:

Lead-perovskite thin film has very low carrier density leading to the high sheet resistance and resistivity for the perovskite thin films. This helps to explain the high series resistance typically observed in perovskite solar cells, which results in a low short-current density (J_{SC}). However, the carrier mobility is much higher than CZTSSe, indicating that there are less detrimental deep defects in perovskite, which helps to explain the long carrier diffusion length of > 1 µm (similar to CIGS which also has a mobility of ~4 cm^2/V.s).

References

[1] IEA International Energy Agency, 2014 Snapshot of Global PV Markets, IEA PVPS T1-26:2015.

[2] Fraunhofer Institute for Solar Energy Systems ISE, Photovoltaics Report, Slide #19, 17 Nov 2015. www.ise.fraunhofer.de

[3] Solar Frontier CIS Module: More electricity in real world conditions, http://www.solar-frontier.com/eng/technology/Performance/index.html

[4] Fraunhofer Institute for Solar Energy Systems ISE, Photovoltaics Report, 17 Nov 2015. www.ise.fraunhofer.de

[5] J. J. Scragg, P. J. Dale, L. M. Peter, G. Zoppi, and I. Forbes, Phys. Stat Sol. B **245**, 1772 (2008).

[6] R. Birkmire, in *Solar Cells and their Applications* (John Wiley & Sons, Inc., 2010), p. 137.

[7] H.-W. Schock, in *Encyclopedia of Sustainability Science and Technology*, edited by R. Meyers (Springer New York, 2012), p. 9394.

[8] W. Shockley and H. J. Queisser, J. Appl. Phys. **32**, 510 (1961).

[9] U. Rau and J. H. Werner, Applied Physics Letters **84**, 3735 (2004).

[10] J. Lee, J. D. Cohen, and W. N. Shafarman, Thin Solid Films **480–481**, 336 (2005).

[11] O. Gunawan, et al., Appl. Phys. Lett. **100**, 253905 (2012).

[12] A. O. Pudov, A. Kanevce, H. A. Al-Thani, J. R. Sites, and F. S. Hasoon, J. Appl. Phys. **97**, 064901 (2005).

[13] R. Scheer, J. Appl. Phys. **105**, 104505 (2009).

[14] H. Katagiri, N. Sasaguchi, S. Hando, S. Hoshino, J. Ohashi, and T. Yokota, Sol. Energy Mater. Sol. Cells **49**, 407 (1997).

[15] K. Jimbo, R. Kimura, T. Kamimura, S. Yamada, W. S. Maw, H. Araki, K. Oishi, and H. Katagiri, Thin Solid Films **515**, 5997 (2007).

[16] K. Hironori, J. Kazuo, Y. Satoru, K. Tsuyoshi, M. Win Shwe, F. Tatsuo, I. Tadashi, and M. Tomoyoshi, Appl. Phys. Expr. **1**, 041201 (2008).

[17] B. Shin, O. Gunawan, Y. Zhu, N. A. Bojarczuk, S. J. Chey, and S. Guha, Prog. Photovolt: Res. Appl. **21**, 72 (2013).

[18] H. Hiroi, N. Sakai, T. Kato, and H. Sugimoto, in *Photovoltaic Specialists Conference (PVSC), 2013 IEEE 39th*, 2013), p. 0863.

[19] Y. S. Lee, T. Gershon, O. Gunawan, T. K. Todorov, T. Gokmen, Y. Virgus, and S. Guha, Adv. Energy Mater. **5**, 1401372 (2015).

[20] W. Wang, M. T. Winkler, O. Gunawan, T. Gokmen, T. K. Todorov, Y. Zhu, and D. B. Mitzi, Adv. Energy Mater. **4**, 1301465 (2014).

[21] A. Polizzotti, I. L. Repins, R. Noufi, S.-H. Wei, and D. B. Mitzi, Energy & Environmental Science **6**, 3171 (2013).

[22] K. Ito, *Copper Zinc Tin Sulfide-Based Thin Film Solar Cells* (Wiley, 2014).

[23] T. K. Todorov, O. Gunawan, T. Gokmen, and D. B. Mitzi, Prog. Photovolt: Res. Appl. **21**, 82 (2013).

[24] T. K. Todorov, K. B. Reuter, and D. B. Mitzi, Adv. Mater. **22**, E156 (2010).

[25] S. Chen, A. Walsh, X.-G. Gong, and S.-H. Wei, Adv. Mater. **25**, 1522 (2013).

[26] S. Chen, J.-H. Yang, X. G. Gong, A. Walsh, and S.-H. Wei, Phys. Rev. B. **81**, 245204 (2010).

[27] M. Dimitrievska, A. Fairbrother, E. Saucedo, A. Pérez-Rodríguez, and V. Izquierdo-Roca, Appl. Phys. Lett. **106**, 073903 (2015).

[28] Y. Yan, C. S. Jiang, R. Noufi, S.-H. Wei, H. R. Moutinho, and M. M. Al-Jassim, Phys. Rev. Lett. **99**, 235504 (2007).

[29] C. Persson and A. Zunger, Phys. Rev. Lett. **91**, 266401 (2003).

[30] S. Siebentritt, S. Sadewasser, M. Wimmer, C. Leendertz, T. Eisenbarth, and M. C. Lux-Steiner, Phys. Rev. Lett. **97**, 146601 (2006).

[31] T. Gokmen, O. Gunawan, T. K. Todorov, and D. B. Mitzi, Appl. Phys. Lett. **103**, 103506 (2013).

[32] A. D. Collord, H. Xin, and H. W. Hillhouse, IEEE J. Photovolt. **5**, 288 (2015).

[33] S. S. Hegedus and W. N. Shafarman, Prog. Photovolt: Res. Appl. **12**, 155 (2004).

[34] O. Gunawan, T. K. Todorov, and D. B. Mitzi, Appl. Phys. Lett. **97**, 233506 (2010).

[35] A. Redinger, M. Mousel, M. H. Wolter, N. Valle, and S. Siebentritt, Thin Solid Films **535**, 291.

[36] A. Fairbrother, E. García-Hemme, V. Izquierdo-Roca, X. Fontané, F. A. Pulgarín-Agudelo, O. Vigil-Galán, A. Pérez-Rodríguez, and E. Saucedo, J. Am. Chem. Soc. **134**, 8018 (2012).

[37] A. Fairbrother, X. Fontané, V. Izquierdo-Roca, M. Espíndola-Rodríguez, S. López-Marino, M. Placidi, L. Calvo-Barrio, A. Pérez-Rodríguez, and E. Saucedo, Sol. Energy Mater. Sol. Cells **112**, 97 (2013).

[38] M. A. Green, *Solar cells: operating principles, technology and system applications.* (Kensington, N.S.W., University of New South Wales, 1992).

[39] Q. Guo, G. M. Ford, W.-C. Yang, B. C. Walker, E. A. Stach, H. W. Hillhouse, and R. Agrawal, J. Am. Chem. Soc. **132**, 17384 (2010).

[40] T. K. Todorov, J. Tang, S. Bag, O. Gunawan, T. Gokmen, Y. Zhu, and D. B. Mitzi, Adv. Energy Mater. **3**, 34 (2013).

[41] S. Bag, O. Gunawan, T. Gokmen, Y. Zhu, T. K. Todorov, and D. B. Mitzi, Energy & Environmental Science **5**, 7060 (2012).

[42] G. Brammertz, M. Buffière, S. Oueslati, H. ElAnzeery, K. Ben Messaoud, S. Sahayaraj, C. Köble, M. Meuris, and J. Poortmans, Appl. Phys. Lett. **103** (2013).

[43] S. Chen, X. G. Gong, A. Walsh, and S.-H. Wei, Appl. Phys. Lett. **94**, 041903 (2009).

[44] Peter Wurfel, Physics of solar cells: from principles to new concepts, Wiley-VCH Verlag GmbH, 2005, p. 115.

[45] Peter Wurfel, Physics of solar cells: from principles to new concepts, Wiley-VCH Verlag GmbH, 2005, p. 122.

[46] O. Madelung, *Semiconductors: other than Group IV elements and III-V compounds* (Springer-Verlag Berlin Heidelberg GmbH, 1992).

[47] S. B. Zhang, S.-H. Wei, A. Zunger, and H. Katayama-Yoshida, Phys. Rev. B **57**, 9642 (1998).

[48] S.-H. Wei and S. B. Zhang, Physical Review B **66**, 155211 (2002).

[49] National Institute of Standards and Technology, Hall Effect Measurements, http://http://www.nist.gov/pml/div683/hall.cfm

[50] J. P. Leitão, N. M. Santos, P. A. Fernandes, P. M. P. Salomé, A. F. da Cunha, J. C. González, G. M. Ribeiro, and F. M. Matinaga, Physical Review B **84**, 024120 (2011).

[51] T. Tanaka, T. Nagatomo, D. Kawasaki, M. Nishio, Q. Guo, A. Wakahara, A. Yoshida, and H. Ogawa, Journal of Physics and Chemistry of Solids **66**, 1978 (2005).

[52] R. Adhi Wibowo, E. Soo Lee, B. Munir, and K. Ho Kim, physica status solidi (a) **204**, 3373 (2007).

[53] R. A. Wibowo, W. S. Kim, E. S. Lee, B. Munir, and K. H. Kim, Journal of Physics and Chemistry of Solids **68**, 1908 (2007).

[54] C. P. Chan, H. Lam, and C. Surya, Sol. Energy Mater. Sol. Cells **94**, 207 (2010).

[55] T. Prabhakar and N. Jampana, Sol. Energy Mater. Sol. Cells **95**, 1001 (2011).

[56] Z. Zhou, Y. Wang, D. Xu, and Y. Zhang, Sol. Energy Mater. Sol. Cells **94**, 2042 (2010).

[57] S. W. Shin, S. M. Pawar, C. Y. Park, J. H. Yun, J.-H. Moon, J. H. Kim, and J. Y. Lee, Sol. Energy Mater. Sol. Cells **95**, 3202 (2011).

58 N. Z. Lupu, N. M. Tallan, and D. S. Tannhauser, Review of Scientific Instruments **38**, 1658 (1967).

59 J. Lindemuth, in *Magnetics Technology International*, 2012), p. 37.

60 O. Gunawan, Y. Virgus, and K. F. Tai, Appl. Phys. Lett. **106**, 062407 (2015).

61 L. J. van der Pauw, Philips Research Reports **13** (1958).

62 P. M. Hemenger, Review of Scientific Instruments **44**, 698 (1973).

63 Gunawan, O. and B. Lei, Solar cell characterization system with an automated continuous neutral density filter, USPTO, Editor. 2014: USA.

64 C. Zhang, J. Zhang, Y. Hao, Z. Lin, and C. Zhu, J. Appl. Phys. **110**, 064504 (2011).

65 R. A. Sinton and A. Cuevas, in *Proc. 16th Eur. Photovolt. Sol. Energy Conf.* (Taylor & Francis, Glasgow, UK, 2000), p. 1152.

66 O. Gunawan, T. Gokmen, and D. B. Mitzi, J. Appl. Phys. **116**, 084504 (2014).

67 D. B. Mitzi, M. Yuan, W. Liu, A. J. Kellock, S. J. Chey, V. Deline, and A. G. Schrott, Adv. Mater. **20**, 3657 (2008).

68 D. A. R. Barkhouse, O. Gunawan, T. Gokmen, T. K. Todorov, and D. B. Mitzi, Prog. Photovolt: Res. Appl. **20**, 6 (2012).

69 T. Todorov, H. Sugimoto, O. Gunawan, T. Gokmen, and D. B. Mitzi, IEEE J. Photovolt. **4**, 483 (2014).

70 H. H. Park, et al., Appl. Phys. Lett. **105**, 202101 (2014).

71 W. van Roosbroeck, Phys. Rev. B **101**, 1713 (1956).

72 A. R. Moore, Appl. Phys. Lett. **37**, 327 (1980).

73 P. Jackson, D. Hariskos, R. Wuerz, O. Kiowski, A. Bauer, T. M. Friedlmeier, and M. Powalla, Phys. Stat Sol. RRL **9**, 28 (2014).

74 S. Siebentritt, Thin Solid Films **535**, 1 (2013).

75 M. A. Green, K. Emery, Y. Hishikawa, W. Warta, and E. D. Dunlop, Prog. Photovolt: Res. Appl. **23**, 1 (2015).

76 Impact of both series and shunt resistance, http://pveducation.org/pvcdrom/solar-cell-operation/impact-of-both-resistances, accessed: June, 2015.

77 L. J. v. d. Pauw, in *Philips Research Reports*, 1958), Vol. 13, p. 1.

78 O. D. Miller, E. Yablonovitch, and S. R. Kurtz, IEEE J. Photovolt. **2**, 303 (2012).

79 M. C. Peter Y.Yu, *Fundamentals of Semiconductors* (Springer 2005).

80 A. L. Efros and B. I. Shklovskii, *Electronic Properties of Doped Semiconductors* (Springer-Verlag Berlin Heidelberg, 1984).

81 A. Bauknecht, S. Siebentritt, J. Albert, and M. C. Lux-Steiner, J. Appl. Phys. **89**, 4391 (2001).

82 A. P. Levanyuk and V. V. Osipov, Sov. Phys. Uspekhi **24**, 187 (1981).

83 I. Dirnstorfer, M. Wagner, D. M. Hofmann, M. D. Lampert, F. Karg, and B. K. Meyer, Phys. Stat Sol. A **168**, 163 (1998).

84 T. Gershon, B. Shin, N. Bojarczuk, M. Hopstaken, D. B. Mitzi, and S. Guha, Adv. Energy Mater. **5**, 1400849 (2014).

85 T. Schmidt, K. Lischka, and W. Zulehner, Phys. Rev. B **45**, 8989 (1992).

86 T. Gershon, B. Shin, N. Bojarczuk, T. Gokmen, S. Lu, and S. Guha, J. Appl. Phys. **114**, 154905 (2013).

87 C. Persson, J. Appl. Phys. **107**, 053710 (2010).

88 S. Minoura, K. Kodera, T. Maekawa, K. Miyazaki, S. Niki, and H. Fujiwara, J. Appl. Phys. **113**, 063505 (2013).

89 C. Persson, Appl. Phys. Lett. **93**, 072106 (2008).

90 B. Ohnesorge, R. Weigand, G. Bacher, A. Forchel, W. Riedl, and F. H. Karg, Appl. Phys. Lett. **73**, 1224 (1998).

91 J. H. Davies, *The Physics of Low-Dimensional Semiconductors* (Cambridge University Press, United Kingdom, 1998).

[92] J. I. Pankove ed., *Optical Processes in Semiconductors* (Dover Publications, New York, 1975).
[93] R. J. Nelson and R. G. Sobers, J. Appl. Phys. **49**, 6103 (1978).
[94] D. W. Miller, C. W. Warren, O. Gunawan, T. Gokmen, D. B. Mitzi, and J. D. Cohen, Appl. Phys. Lett. **101**, 142106 (2012).
[95] S. Ahmed, K. B. Reuter, O. Gunawan, L. Guo, L. T. Romankiw, and H. Deligianni, Adv. Energy Mater. **2**, 253 (2012).
[96] J. J. Scragg, J. T. Wätjen, M. Edoff, T. Ericson, T. Kubart, and C. Platzer-Björkman, J. Am. Chem. Soc. **134**, 19330 (2012).
[97] J. Li, Y. Zhang, W. Zhao, D. Nam, H. Cheong, L. Wu, Z. Zhou, and Y. Sun, Adv. Energy Mater. **5**, 1402178 (2015).
[98] S. P. Harvey, I. Repins, and G. Teeter, J. Appl. Phys. **117**, 074902 (2015).
[99] B. Shin, Y. Zhu, N. A. Bojarczuk, S. J. Chey, and S. Guha, Appl. Phys. Lett. **101**, 053903 (2012).
[100] Shiro Nishiwaki, Naoki Kohara, Takayuki Negami, and Takahiro Wada, Jap. J. Appl. Phys. **37**, L71 (1998).
[101] T. Minemoto, T. Matsui, H. Takakura, Y. Hamakawa, T. Negami, Y. Hashimoto, T. Uenoyama, and M. Kitagawa, Sol. Energy Mater. Sol. Cells **67**, 83 (2001).
[102] R. Haight, A. Barkhouse, O. Gunawan, B. Shin, M. Copel, M. Hopstaken, and D. B. Mitzi, Appl. Phys. Lett. **98**, 253502 (2011).
[103] M. Bar, et al., Appl. Phys. Lett. **99**, 222105 (2011).
[104] The RS is also extracted using Lambert-W fitting method.
[105] L. A. Burton, D. Colombara, R. D. Abellon, F. C. Grozema, L. M. Peter, T. J. Savenije, G. Dennler, and A. Walsh, Chem. Mater. **25**, 4908 (2013).
[106] A. Khare, B. Himmetoglu, M. Cococcioni, and E. S. Aydil, J. Appl. Phys. **111**, 123704 (2012).
[107] J. M. R. Tan, Y. H. Lee, S. Pedireddy, T. Baikie, X. Y. Ling, and L. H. Wong, J. Am. Chem. Soc. **136**, 6684 (2014).
[108] T. Nomura, T. Maeda, K. Takei, M. Morihama, and T. Wada, Phys. Stat Sol. C **10**, 1093 (2013).
[109] A. J. Smith, P. E. Meek, and W. Y. Liang, J. Phys. C: Solid State Phys. **10**, 1321 (1977).
[110] S.-H. Su, et al., Front. Energy Res. **2**, 27 (2014).
[111] C. Ruei-San, T. Chih-Che, S. Wei-Chu, and H. Ying-Sheng, Nanotechnology **25**, 415706 (2014).
[112] A. Fairbrother, et al., Prog. Photovolt: Res. Appl. **22**, 479 (2014).
[113] M. Danilson, M. Altosaar, M. Kauk, A. Katerski, J. Krustok, and J. Raudoja, Thin Solid Films **519**, 7407 (2011).
[114] W. E. Morgan and J. R. Van Wazer, J. Phys. Chem. **77**, 964 (1973).
[115] R. B. Shalvoy, G. B. Fisher, and P. J. Stiles, Phys. Rev. B **15**, 1680 (1977).
[116] M. Oshikiri and F. Aryasetiawan, Phys. Rev. B **60**, 10754 (1999).
[117] K. K. Kam and B. A. Parkinson, J. Phys. Chem. **86**, 463 (1982).
[118] M. T. Winkler, W. Wang, O. Gunawan, H. J. Hovel, T. K. Todorov, and D. B. Mitzi, Energy Environ. Sci. **7**, 1029 (2014).
[119] A. Carrete, A. Shavel, X. Fontané, J. Montserrat, J. Fan, M. Ibáñez, E. Saucedo, A. Pérez-Rodríguez, and A. Cabot, J. Am. Chem. Soc. **135**, 15982 (2013).
[120] H. Guo, Y. Cui, Q. Tian, S. Gao, G. Wang, and D. Pan, Crystal Growth & Design **15**, 771 (2015).
[121] I. Repins, et al., Sol. Energy Mater. Sol. Cells **101**, 154 (2012).
[122] T. Tanaka, D. Kawasaki, M. Nishio, Q. X. Gu, and H. Ogawal, in *Phys. Stat Sol. - Current Topics in Solid State Physics*, edited by M. Stutzmann (Wiley-V C H Verlag Gmbh, Weinheim, 2006), Vol. 3, p. 2844.

123 H. Katagiri, K. Jimbo, W. S. Maw, K. Oishi, M. Yamazaki, H. Araki, and A. Takeuchi, Thin Solid Films **517**, 2455 (2009).

124 J. J. Scragg, P. J. Dale, and L. M. Peter, Thin Solid Films **517**, 2481 (2009).

125 J. J. Scragg, D. M. Berg, and P. J. Dale, Journal of Electroanalytical Chemistry **646**, 52 (2010).

126 R. Schurr, et al., Thin Solid Films **517**, 2465 (2009).

127 J.-O. Jeon, et al., ChemSusChem **7**, 1073 (2014).

128 H. Zhou, W.-C. Hsu, H.-S. Duan, B. Bob, W. Yang, T.-B. Song, C.-J. Hsu, and Y. Yang, Energy Environ. Sci. **6**, 2822 (2013).

129 Q. J. Guo, H. W. Hillhouse, and R. Agrawal, J. Am. Chem. Soc. **131**, 11672 (2009).

130 C. Steinhagen, M. G. Panthani, V. Akhavan, B. Goodfellow, B. Koo, and B. A. Korgel, J. Am. Chem. Soc. **131**, 12554 (2009).

131 G. M. Ford, Q. J. Guo, R. Agrawal, and H. W. Hillhouse, Chemistry of Materials **23**, 2626 (2011).

132 X. Zeng, K. F. Tai, T. Zhang, C. W. J. Ho, X. Chen, A. Huan, T. C. Sum, and L. H. Wong, Sol. Energy Mater. Sol. Cells **124**, 55 (2014).

133 H. Xin, J. K. Katahara, I. L. Braly, and H. W. Hillhouse, Adv. Energy Mater. **4**, 1301823 (2014).

134 Z. Su, et al., Journal of Materials Chemistry A **2**, 500 (2014).

135 S.-N. Park, S.-J. Sung, D.-H. Son, D.-H. Kim, M. Gansukh, H. Cheong, and J.-K. Kang, RSC Advances **4**, 9118 (2014).

136 Y. Sun, et al., Journal of Materials Chemistry A **1**, 6880 (2013).

137 W. Ki and H. W. Hillhouse, Adv. Energy Mater. **1**, 732 (2011).

138 T. Schnabel, M. Löw, and E. Ahlswede, Sol. Energy Mater. Sol. Cells **117**, 324 (2013).

139 H. Xin, S. M. Vorpahl, A. D. Collord, I. L. Braly, A. R. Uhl, B. W. Krueger, D. S. Ginger, and H. W. Hillhouse, Phys. Chem. Chem. Phys. **17**, 23859 (2015).

140 H. Park, Y. Hwang, and B.-S. Bae, J Sol-Gel Sci Technol **65**, 23 (2013).

141 A. Khare, B. Himmetoglu, M. Johnson, D. J. Norris, M. Cococcioni, and E. S. Aydil, J. Appl. Phys. **111**, 083707 (2012).

142 Y. Cho, X. Lue, M. Wienold, M. Ramsteiner, H. T. Grahn, and O. Brandt, Phys. Rev. B. **87**, 155203 (2013).

143 B. T. Gershon, Y. S. Lee, R. Mankad, O. Gunawan, T. Gokmen, D. Bishop, B. McCandless, and S. Guha, Appl. Phys. Lett. **106**, 123905 (2015).

144 M. A. Contreras, M. J. Romero, and R. Noufi, Thin Solid Films **511–512**, 51 (2006).

145 M. Yuan, D. B. Mitzi, W. Liu, A. J. Kellock, S. J. Chey, and V. R. Deline, Chemistry of Materials **22**, 285 (2010).

146 P. A. Fernandes, P. M. P. Salomé, and A. F. d. Cunha, Journal of Physics D: Applied Physics **43**, 215403 (2010).